SIMULATION OF INTIMAL THICKENING INDUCED BY HEMODYNAMICAL SHEAR STRESSES

by

Avishek Mukherjee

A dissertation submitted to the Faculty of the University of Delaware in partial fulfillment of the requirements for the degree of Doctor of Philosophy in Mathematics

Fall, 2023

SIMULATION OF INTIMAL THICKENING INDUCED BY HEMODYNAMICAL SHEAR STRESSES

by

Avishek Mukherjee

Approved: ____
Mark S. Gockenbach, Ph.D.
Chair of the Department of Mathematical Sciences

Approved: ____
Debra Hess Norris
Interim Dean of the College of Arts and Sciences

Approved: ____
Louis F. Rossi, Ph.D.
Vice Provost for Graduate and Professional Education and
Dean of the Graduate College

I certify that I have read this dissertation and that in my opinion it meets the academic and professional standard required by the University as a dissertation for the degree of Doctor of Philosophy.

Signed: ____
Pak-Wing Fok, Ph.D.
Professor in charge of dissertation

I certify that I have read this dissertation and that in my opinion it meets the academic and professional standard required by the University as a dissertation for the degree of Doctor of Philosophy.

Signed: ____
Ryan Zurakowski, Ph.D.
Member of dissertation committee

I certify that I have read this dissertation and that in my opinion it meets the academic and professional standard required by the University as a dissertation for the degree of Doctor of Philosophy.

Signed: ____
Tobin Driscoll, Ph.D.
Member of dissertation committee

I certify that I have read this dissertation and that in my opinion it meets the academic and professional standard required by the University as a dissertation for the degree of Doctor of Philosophy.

Signed: ____
Richard Braun, Ph.D.
Member of dissertation committee

ACKNOWLEDGEMENTS

I would like to express my gratitude to my advisor Dr. Pak-Wing Fok for his guidance, help, and patience throughout the process.

I would also like to thank Dr. Lloyd N. Trefethen (University of Oxford) and Dr. Tobin Driscoll (University of Delaware) for their help and guidance on the topic of numerical conformal maps, which led me to look at a particular aspect of the research in a new light.

I would like to thank the committee members Dr. Ryan Zurakowski, Dr. Tobin Driscoll, and Dr. Richard Braun for dedicating their valuable time to go over my thesis and offering valuable suggestions and insights that helped to enrich this thesis.

In addition, I would also like to thank Dr. Navid Mohammad Mirzaei and Dr. Jerome Troy for their help with some aspects of coding in FEniCS.

I am grateful to my friends Dr. Kamal Joshi and Shreeha Upadhyaya for their support throughout my PhD program.

I would like to dedicate this thesis to my parents for their unconditional support in the best and the worst of times.

TABLE OF CONTENTS

Appendix

LIST OF TABLES

LIST OF FIGURES

ABSTRACT

Atherosclerosis is an inflammatory disease in medium-sized and large arteries caused by accumulation of lipids within the arterial wall. It is a complex process that involves lipid infiltration through the sites of endothelial damage, formation of foam cells, and the creation of plaques. These plaques can rupture, releasing clotting agents into the bloodstream, causing a complete blockage of blood vessels, resulting in heart attacks and strokes. The complex process of atherosclerosis starts with a benign thickening of the intima. Thus, intimal thickening is a precursor to atherosclerosis.

The goal of this work is to investigate intimal growth in arteries, induced by hemodynamical shear stress, through finite element simulation using the FEniCS computational environment. In this thesis, we develop a mathematical model that establishes a relationship between growth and hemodynamics, which should be viewed as providing a framework for coupling hemodynamic simulations to mathematical descriptions of atherosclerosis, both of which have been modeled separately in great detail. In our model, the growth of the intima depends on cross section geometry and features of hemodynamics (shear stress). In this work, the arterial wall is modeled as three distinct layers, the intima, the media, and the adventitia, each with different material properties. Since the average mechanical properties of an arterial wall are more or less uniform along the axial direction, we introduce a 2D model of an arterial cross section in which all variables of interest are invariant with respect to the axial direction. Blood flow through vessels is approximately non-turbulent and unidirectional in regions of the vessel away from vessel arches and bifurcations. In addition, in our model, the timescale for vessel growth and deformation is very large compared to the timescale of the blood velocity. Thus, taking time average of the velocity of blood flow

with respect to the timescale of our simulations, the blood flow can be approximated to be steady. Further, the the dissipative forces near the boundary (the endothelium) becomes large so the tangential component of the velocity vanishes. Hence, we assume that the blood flow is steady, non-turbulent, and unidirectional. The blood flow is modeled with a Poisson equation (derived from time-independent and unidirectional Navier-Stokes equation in absence of external forces) with a zero-flow Dirichlet boundary condition at the endothelium. We calculate the shear stress from the solution to the Poisson equation. Damages to endothelial cells induce platelets from blood to attach to the sites of injury that release platelet-derived growth factor (PDGF). In addition, endothelial cells themselves release PDGF in response to shear stress. In this work, since we are interested in the release of PDGF by uninjured endothelial cells, we assume that the endothelial cells release PDGF in a shear-dependent manner. Although PDGF causes cell proliferation both in the intima and the media, but since we are only interested in the growth of intima, growth is assumed to occur only in the intima and is modeled using morphoelasticity theory. The PDGF transport is modeled as a steady-state diffusion-degradation equation since the time scale of diffusion and degradation of PDGF happens at a time scale much much smaller compared to timescale of the intimal growth. We solve the diffusion-degradation equation in all three layers subject to a Neumann boundary condition on the endothelium that registers the flux of PDGF through the endothelium into the intima and a Dirichlet boundary condition on the outer boundary of the adventitia. Since the endothelium is far away from the outer boundary of the adventitia and considering the diffusion and degradation of PDGF across the arterial wall, the PDGF concentration at the outermost boundary of the arterial wall can be considered to be negligible. Therefore, we impose a zero PDGF Dirichlet boundary condition on the outermost boundary of the arterial wall. Finally, the optimal displacement fields for the arterial wall and the lumen are obtained by minimizing strain energy functionals for the arterial wall and the lumen.

We simulate intimal growth for three distinct arterial cross section geometries. We

show that the rate of intimal thickening varies depending on different cross section geometries. For cross section geometries that are annular, the growth of the intima is uniform in the angular direction, the endothelium stays a disk as the intima grows. For non-annular cross section geometries, thicker intimas grow more compared to thinner ones, rate of intimal thickening depends on the distance to the center of flow (greater distance, less growth), shear stress is negatively correlated with distance from the flow center (where the flow velocity is maximal), the maxima and minima of curvature increase and decrease, respectively, with time, the PDGF concentration increase with time, the shape of the lumen becomes polygonal over time for non-annular cross sections. We also observe multiple remodelling phases of the lumen (the lumen dilates, followed by a contraction, followed by a dilation). This multiple remodelling feature is completely new and hasn't been addressed in any literature yet. Each layer of the artery has transversely helical collagen fiber fields which when stretched offer resistance to outward dilation, thus contributing to the total energy of the system. While there are several interpolation and probabilistic techniques available to model the fiber distributions, we implemented the technique of numerical conformal maps to model the fiber field distribution in each of the layers.

The mathematical model established in this thesis should be viewed as providing a framework for coupling hemodynamics simulations to mathematical descriptions of atherosclerosis, both of which have been modeled separately in great detail. This work can be extended to include the process of atherosclerosis and its progression that will shed light on the association among hemodynamics, intimal thickening and atherosclerosis, which is associated with life-threatening diseases. With the advancement of medical technologies, our model, coupled with a model for atherosclerosis, can help predict cardiovascular diseases in advance.

Chapter 1

INTRODUCTION

Cardiovascular diseases have become a major health concern in our modern industrialized society. Often factors like lack of exercise, unhealthy diet, stress and anxiety, among many, contribute to cardiovascular diseases. Among different types of cardiovascular diseases, atherosclerosis is the primary cause for cardiovascular events like myocardial infarctions and stroke. In the United States alone, heart disease has been regarded as the leading cause of death since 1950 [23]. Thus, mathematical models that describe the buildup of atherosclerotic plaque are very important. Atherosclerosis has been the subject of many investigations over the past few decades [66, 40, 41, 9, 21, 64, 19].

Endothelial dysfunction is considered as one of the early markers of atherosclerosis [7]. One of the consequences of endothelial dysfunction is that it can cause low-density lipoprotein (LDL) trafficking from the bloodstream into the intima. This starts a cascade of inflammation processes, resulting in atherosclerosis. Atherosclerosis is a gradual phenomenon and has several stages of progression.

Shear stress, along with the geometry of blood vessels, are important predictors of atherosclerosis [8]. In the article, Dolan *et. al.* observed that vessel bifurcations and arches are prone to atherosclerosis due to complex flow patterns at these locations. An unidirectional and constant flow is observed in parts of the arterial tree that have uniform cross section geometry and oscillatory flows are observed at vessel bifurcations and arches [4]. Regions experiencing low shear stress are prone to the development of atherosclerotic lesions; an observation similar to that made by Zaromytidou *et. al.* in [81]. The shear stress depends on the geometry of the vessel. At vessel bifurcations, the lateral wall experiences low oscillatory shear stress while the point of bifurcation experiences high shear stress (see Fig. 2 in [4]).

1.1 General properties of blood flow

Blood is generally considered to have non-Newtonian properties. The non-Newtonian features of blood arise primarily due to the presence of cells and platelets suspended in the plasma [60]. One of the main features of a non-Newtonian blood flow is that the viscosity varies with the shear rate. Although blood is non-Newtonian in nature, Newtonian blood flow models are used extensively. The main important feature of Newtonian blood is that the dynamic viscosity does not depend on the shear rate. For a Newtonian fluid, the dynamic viscosity (η) and kinematic viscosity (ν_k) are related as $\dfrac{\eta}{\rho} = \nu_k$, with ρ being the density of blood. In [32], Johnston *et. al.* state that for mid-range to high shear rate, a Newtonian model of blood flow can be used, whereas, for low shear rate, a generalised power law model (that establishes a relation between viscosity and shear rate) can be used to model a non-Newtonian blood flow. The viscosity of Newtonian blood is 0.0345 Poise ($\approx 4 \times 10^{-6}$ kPa.s) [32]. In [17], Gijsen *et. al.* studied the effects of non-Newtonian and Newtonian blood flow on the velocity profile at the carotid bifurcation. The authors found that the experimental results were in good agreement with the numerical results both for a Newtonian and a non-Newtonian blood flow. Blood flow through arteries can be laminar or turbulent. The Reynolds' number is used to characterize whether a Newtonian flow can become turbulent or not. The Reynolds' number for a non-Newtonian fluid is given by the formula $Re = \frac{\rho a U}{\nu_k(0)}$ [76], where ρ is the density of blood, a is the diameter of the vessel, U is the average incoming velocity, and $\nu_k(0)$ is the kinematic viscosity of blood when the shear rate is 0. In [76], Tian *et. al.* study the effect of Reynolds' number on the wall shear stress of a 2D channel with plaque being modelled with the function $y = -a + A \exp[-(x - x_0)^2/b^2]$, where A and b represent the height and the width of the stenosis, respectively, x_0 is the center of stenosis, and $2a$ is the width of the 2D flow channel. They experimented for different values of the ratios A/a (height of the plaque) and b/a (width of the plaque) to observe that (i) the wall shear stress increases on the wall on which the plaque is located, (ii) greater values of A/a compared to b/a change the characteristics the flow significantly, and (iii) increasing the Reynolds' number decreases the wall shear stress. In [76], Tian *et. al.* are using a highly idealized representation of a stenosed artery. Since there is a close relationship between the Reynolds' number and the wall shear stress, Reynolds' number plays a critical role in atherosclerosis. In [38], Ku reports that the typical Reynolds' number for blood varies from 1 in small arterioles to 4000 in large arteries .

1.2 Poiseuille blood flow models

Although blood flow, considering it to be Newtonian, is very complex and is determined by the full solution to Navier-Stokes equation, sometimes the blood flow is modeled as being laminar. In [55], Olufsen and Nadim observe that in case of small arteries with radius less than 0.2 cm, the relationship between flow and pressure can be well described by a Poiseuille law, whereas, for large arteries, one may have to incorporate more spatial dependence, especially when turbulence arises. In [54], Olufsen studies blood flow conditions in large systemic arteries using a blood flow model that is axisymmetric, Newtonian, laminar, and incompressible. In a similar study [56], Olufsen *et. al.* study the blood flow in large systemic arteries by reducing the Navier-Stokes equations to a set of 1D linearized PDEs under the assumption of an axisymmetric Navier-Stokes equations. In [5], Chiu and Chien state that in the straight parts of the arterial tree, the flow is laminar, resulting in high shear stress, while in branches and arches, the flow is highly disturbed, resulting in irregular wall shear stress. In short, there are simple laminar flow solutions (such as Poiseuille flow) to the Navier-Stokes equations under special circumstances.

1.3 Flows in complex geometries

As mentioned above, blood flow is qualitatively different in different parts of the arterial tree. There are several instances when there is a transition of a laminar flow to a turbulent one. In the study [62], Quarteroni points out some of the factors that are responsible for the transition from a laminar flow to a turbulent one. Some of the factors are physical exercise which increases the flow velocity, a stenotic artery that increases the Reynolds' number, and decreased blood viscosity caused by diseases like anemia. Turbulent blood flows also depend on the percentage of stenosis. In the study [31], Jahangiri *et. al.* mention that flow is approximately laminar for stenosis up to 70% while the flow is usually turbulent when stenosis exceeds 80%. Spiral laminar flows are also observed in arteries [74]. In this study, Stonebridge *et. al.* examined blood flow patterns in the common carotid artery, internal carotid artery, external carotid artery, common femoral artery, superficial femoral artery, and the infra renal aorta in a cohort of 42 volunteers. They observed that 97% of the volunteers have more sites with spiral laminar flow compared to other flows. Alongside sudden changes in vessel geometry, any remodelling of the heart itself induces turbulence in the flow [53]. This study observed that an aortic dilation causes turbulence in the aortic arch. Such turbulent flows are common at vessel arches and bifurcations, leading to low wall shear stress and high oscillatory index [43], making these regions prone to atherosclerosis and plaque progression.

These kinds of changes in the flow pattern induce a change in the mechanoresponse of the endothelial cells. As a result, there is lipid trafficking into the intima, which eventually progresses to atherosclerosis. The disease develops as a benign thickening of the intima which we discuss in Section 1.5.

1.4 Hemodynamics and shear stress

Blood flow and features of hemodynamics like blood pressure, shear stress, and flow velocity also play a significant role in determining the rate of progression of intimal thickening and formation of plaques. The blood flow through the lumen of a blood vessel induces shear stress on the endothelium. Researchers have speculated that plaques can be sensitive to the shear stress magnitude, or the time rate of change of shear stress. The nature of the shear stress also impacts the localization, formation, and progression of atherosclerotic plaques.

In the study [13], Friedman *et. al.* observed a correspondence between shear stress and intimal thickening in young and old vessels. They observed that intimas corresponding to low shear stress in young vessels are thinner compared to high shear stress. But for older vessels, high shear stress corresponds to thinner intimas compared to low shear stress.

The progression of advanced atherosclerosis may also depend on the time rate of change of shear stress. The study [38] observes that plaques form and localize at sites of low oscillatory shear stress. In [33], Moore Jr *et. al.* demonstrate that low oscillatory shear stress is highly correlated with plaque development compared to regions experiencing a high oscillatory shear stress.

In addition, vessel wall thickness has a correlation with blood pressure as observed in the study [42]. In this study, Liu and Fung observed a positive correlation between vessel wall thickness and increasing blood pressure in rats. In another study [80], six cynomolgus monkeys were fed a diet consisting of 2% cholesterol and 25% peanut oil. Then the blood flow was increased by constructing an arteriovenous fistula between the right iliac artery and vein, with the left iliac artery serving as the control. Zarins *et. al.* observed that the media cross section area increased twofold, with no difference in total media thickness, and no difference in the mean intimal thickness between the right and the left iliac arteries.

1.5 Diffuse intimal thickening and atherosclerosis

Early atherosclerosis begins with the thickening of the intima, known as diffuse intimal thickening (DIT). DIT can occur even in fetuses. In the study [48], Nakashima *et. al.* found evidence of DIT in coronary arteries and the aorta after 36 weeks of gestation. DIT has been known as a precursor to atherosclerosis [50]. The progression from DIT to atherosclerosis involves several factors, among which endothelial dysfunction, lipid accumulation in the intima, proliferation of SMCs induced by growth factors, migration of SMCs from the media to the intima are some. As a result of all these factors, the intima gradually thickens over time becoming a potential site on which atherosclerosis develops [11, 70]. Many studies have tried to classify atherosclerotic plaques with respect to their histology and morphology. In [49], Nakashima *et. al.* classified early-stage atherosclerosis into four stages, Grades 0, 1, 2, and 3, according to the lipid deposition level. They showed that Grade 0 atherosclerosis (DIT) showed no lipid deposits and the absence of macrophages, Grades 1 and 2 showed deposition of fatty streaks and extracellular lipids in the outer layer of the intima, while Grade 3 (pathological intimal thickening) showed presence of extracellular lipids underneath a layer of foam cell macrophages. Low-density lipoprotein (LDL) present in the blood infiltrates the arterial wall because of endothelial dysfunction and undergoes oxidation to form oxidized-LDL (oxLDL). Macrophages chemotax towards oxLDL [63]. The macrophages absorb oxLDL to form foam cells and contribute to the formation of fatty plaques. Another study [57] uses optical coherence tomography to visualize the morphology of the 8 different stages of plaque progression shown in the table below:

Types of lesions	Characteristics
Intimal thickenings or intimal xanthomas	Abundance of smooth muscle cells, proteoglycan-rich extracellular matrix, and absence of inflammation
Pathological intimal thickenings	Presence of proteoglycans and lipid
Fibroatheromas	Lipid-rich necrotic core surrounded by fibrous tissue
Thin cap fibroatheromas	Large necrotic core sheathed by thin fibrous cap
Plaque ruptures	Luminal thrombus overlying a thin, disrupted fibrous cap
Eroded plaques	Absence of fibrous cap rupture, abundance of proteoglycans and smooth muscle cells in luminal thrombus
Calcified nodules	Absence of necrotic core and presence of calcium
Healed lesions	Reparation of disrupted fibrous cap

Table 1.1: Types of lesions and their characteristics

Understanding the progression of atherosclerotic lesions warrants a detailed mathematical model. Over the last few decades, many investigations have been carried out to establish a mathematical model of atherosclerosis. An important constituent for developing a mathematical model is a determination of layer-specific material properties of an arterial wall. In [27], Holzapfel *et. al.* determine the layer-specific mechanical properties of each of the three layers of 13 human nonstenotic left anterior descending coronary arteries through autopsy. These mechanical properties are often incorporated into mathematical models for plaque buildup. In [16], Gasser *et. al.* present a model that accounts for the mechanical properties and collagen fiber distribution in each of the three layers. While [27] and [16] study only the mechanical properties, papers like [11] and [45] use the properties to make predictions about plaque development and growth. Fok and Gou [11] simulated intimal thickening under a time-dependent growth tensor using a hyperelastic framework coupled with morphoelasticity. Mirzaei *et. al.* [45] formulated a mathematical model involving macrophages, lipids, necrotic cells, oxidized lipids, oxygen concentration and platelet-derived growth factor to describe plaque evolution and vessel growth.

One commonly used measure of cardiovascular risk is intima-media thickness (IMT), representing the combined thickness of the intima and the media [6]. In [10], Fernández-Alvarez *et. al.* provide a summary of different studies that report the association between carotid IMT and cardiovascular risk prediction. The authors conclude that carotid IMT is a well-established early marker for carotid atherosclerosis. Thus, assessment of carotid IMT is crucial in predicting future cardiovascular diseases. The study [2] provides an extensive review of different studies conducted on the IMT of the carotid artery across a diverse population of different age groups and sexes. In this study, Aminbaksh and Mancini also referred to studies that measured IMT progression rate over 2 years and then measured the rate again after a 4 year follow-up. The authors compared different studies to find that IMT plays a significant role in determining the risk of a myocardial infarction or stroke. The authors referred to the Rotterdam Study which concluded that a baseline mean IMT of 0.822 mm or greater has a strong correlation with myocardial infarction while a mean IMT of 0.75 mm or greater is strongly associated with the risk of stroke. In addition, if IMT progresses at a rate of 0.034 mm per year, then there is a increased risk of future cardiovascular events. In the study [67], Sakakura *et. al.* studied human autopsy specimens from 17 weeks of gestation to 23 months and observed an increase in intima/media ratio from birth (0.1) to two years of age (0.3). The authors discussed the progression of plaque from a thickened intima to formation of an acellular necrotic core, and classified the progression into four stages: intimal thickening (AHA type I lesion), intimal xanthoma (AHA type II lesion), pathological intimal thickening (PIT) (AHA type III lesion), and fibroatheroma (AHA type IV lesion). The characteristics of each of these lesions is given in Table 1.1.

In summary, intimal thickening can be considered as the "soil" on which atherosclerosis develops, as noted by Schwartz *et. al.* in [70]. Thus, a mathematical model for simulating intimal thickening is a crucial pre-requisite for modeling and simulating atherosclerosis. One of the important and interesting aspects of intimal thickening is that its development is dependent on the shear stress induced on the endothelium due to the blood flow through the vessel.

1.6 General aims

Researchers have separately studied intima-media thickness and the effect of shear stress on vessel wall thickness and atherosclerosis. But to our knowledge, there are fewer studies that tie blood flow, wall shear stress, and the evolution of vessel wall thickness under the effects of hemodynamics. Since intimal thickening is a precursor to atherosclerosis, it is essential to formulate a mathematical model to describe the evolution of vessel wall thickness considering the effects of the hemodynamical features like shear stress. In this thesis, we provide a mathematical framework to calculate and simulate intimal growth under a shear stress induced by a Poiseuille flow.

In this thesis, we simulate intimal growth under hemodynamical shear stresses for three different arterial cross section geometries, an annular cross section and two non-annular cross sections. We show that the rate of intimal growth differs for different cross section geometries, thicker intimas grow more compared to thinner ones, the lumen becomes polygonal with time for non-annular cross sections, how the rate of growth depends on the distance of the region from the center of flow (point on the lumen where the magnitude of the Poiseuille flow is maximum). We also show multiple remodelling phases of the lumen where the lumen first dilates followed by an contraction followed by an outward dilation. We also implement a new technique of numerical conformal maps to simulate collagen fiber fields for each of the three layers of the cross sections. In addition, we demonstrate that the magnitude of shear stress at a particular point on the endothelium has a negative correlation with the distance of the point from the center of flow for non-annular cross sections along with correlations among the distance of the endothelium from the center of flow, PDGF concentration, and the curvature of the endothelium. To the best of our knowledge, there does not exist any literature that investigates how Poiseuille blood flow through different cross section geometries affect intimal thickening.

The mathematical model and simulations in this thesis shed light on the effects of hemodynamical shear stress and vessel cross section geometry on intimal thickening which will help understand why certain areas of the vessels, like arches and bifurcations, are prone to intimal thickening and the development of atherosclerosis and plaques. This model should be viewed as a stepping stone towards a more complete mathematical framework that gels general hemodynamics and plaque development.

All codes used to generate the results of this thesis can be accessed at https://github.com/avishmj/intimal-thickening

Chapter 2

A MODEL FOR SHEAR-INDUCED INTIMAL THICKENING

Platelet derived growth factor (PDGF) is a protein produced by platelets, endothelial cells, smooth muscle cells, and other kinds of cells. The main functions of PDGF are to promote cell growth and division, enhance migration of smooth muscle cells within the arterial wall, and repair arterial tissue by stimulating division of smooth muscle cells along with synthesis of extracellular matrix proteins. PDGF can be produced and released by platelets that attach to endothelial cells at sites of endothelial injury. The endothelial cells themselves can also release PDGF in the absence/presence of shear stress. In this work, we are ignoring endothelial damage and assume that endothelial cells release PDGF in response to shear stress only.

To model intimal growth induced by shear stress and PDGF, we need mathematical models for the blood flow (Section 2.1), the shear stress (Section 2.1.1) due to the blood flow, the growth and elastic response of the vessel wall (Section 2.2), and the PDGF concentration (Section 2.3). This section introduces the mathematical models we considered for our work.

Fig. 2.1 below summarizes our mathematical and computational setup. In Fig. 2.1, the intima-media interface in the reference configuration will be referred to as $\partial\Omega_1^{(2)}$, the media-adventitia interface will be referred to as $\partial\Omega_2^{(2)}$ and their corresponding notations in the grown deformed configuration will be referred to as $\partial\omega_1^{(2)}$ and $\partial\omega_2^{(2)}$, respectively. The lumen–intima interface (endothelium) in both the reference, $\partial\Omega_1^{(1)}$, and the grown, deformed configuration, $\partial\omega_1^{(1)}$, is actually single layer of endothelial cells rather than a mathematical closed curve. However, it is common practice to represent the interface as a mathematical closed curve. A constant pressure P is applied to the endothelium of the grown deformed configuration. The map $\mathbf{\Phi}$ takes a point (X, Y) in the reference stress free configuration to a point (x, y) in the grown deformed configuration.

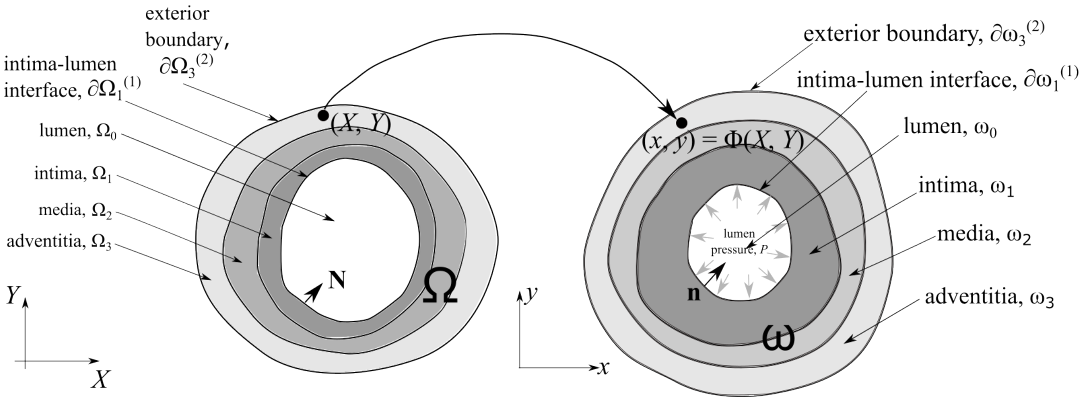

Figure 2.1: Cross section of an artery showing the lumen, intima, media and adventitia. The reference configuration $\Omega = \bigcup_{k=0}^{3} \Omega_k$, is mapped to the grown and deformed configuration $\omega = \bigcup_{k=0}^{3} \omega_k$ and the reference point (X, Y) is mapped to the point (x, y). Ω and ω are the reference and deformed domains, respectively. The unit normal vector $\mathbf{N}$ points into the reference-configuration lumen while $\mathbf{n}$ points into the deformed lumen. The inner and outer boundaries of Ω_k are $\partial\Omega_k^{(1)}$ and $\partial\Omega_k^{(2)}$ respectively for $k = 1, 2, 3$ in the reference frame. These boundaries map to $\partial\omega_k^{(1)}$ and $\partial\omega_k^{(2)}$ in the grown, deformed frame, respectively.

2.1 Hemodynamics

Blood flow is highly pulsatile. Our simulations represent a mean, time-independent flow. We have also considered a unidirectional blood flow. This assumption is reasonable when the flow is laminar. We neglect swirling/turbulent blood flow and the presence of eddies, both of which could be important in atherogenesis. In reality, both pressure gradient across a vessel and the dynamic viscosity of blood change with time and also with axial distance. We made these assumptions to simplify an already complex model. To take into account the effect of the flow on the growth and deformation of the vessel wall, we introduce a mathematical model for the blood flow. At the macroscale, the blood flow is well described by the time-dependent incompressible Navier-Stokes equation, defined in the grown deformed configuration,

$$\frac{\partial \mathbf{V}}{\partial t} + \mathbf{V} \cdot \nabla \mathbf{V} = \frac{\mu_l}{\rho} \nabla^2 \mathbf{V} - \frac{1}{\rho} \nabla p + \mathbf{f}, \tag{2.1}$$

where $\mathbf{V}$, p, μ_l, ρ, and $\mathbf{f} = (f_x, f_y, f_z)$ are the flow velocity, the pressure, the dynamic viscosity of blood, the density of blood, and the external body force, respectively. Since the flow is unidirectional and independent of the Z-axis, $\mathbf{V} = [0, 0, w(x, y)]^T$ and $\mathbf{V} \cdot \nabla \mathbf{V} = \mathbf{0}$. Since blood flow occurs at a time scale much much smaller than the time scale of the process of intimal thickening, we can consider a steady state non-pulsatile blood flow model. Considering a steady-state in the absence of external body forces ($\mathbf{f} = \mathbf{0}$), Eq. (2.1) reduces to

$$-\nabla p + \mu_l \Delta \mathbf{V} = \mathbf{0}. \tag{2.2}$$

Eq. (2.2) is a system of three equations. Since the flow is in the Z-direction, p_x and p_y must be zero. The third equation, along with the assumption that a constant pressure gradient G is applied along the vessel, can be rewritten as

$$\Delta w(x, y) = w_x^2 + w_y^2 = -\frac{G}{\mu_l}, \quad (x, y) \in \omega_0. \tag{2.3}$$

We impose a no-slip boundary condition at the endothelium $\partial \omega_1^{(1)}$ as follows:

$$w(x, y) = 0, \qquad (x, y) \in \partial \omega_1^{(1)}. \tag{2.4}$$

Thus in compact form, Eqs. (2.3, 2.4) can be written as

$$\Delta w = -\frac{G}{\mu_l}, \qquad (x, y) \in \omega_0 \tag{2.5}$$

$$w = 0, \qquad (x, y) \in \partial \omega_1^{(1)} \tag{2.6}$$

In the above equations, ω_0 represents the lumen and $\partial \omega_1^{(1)}$ represents the endothelium.

2.1.1 Shear stress on the endothelium

Due to the Poiseuille blood flow through the lumen, the inner boundary of the intima experiences shear stress in the Z direction. In response to the shear stress, the endothelial cells release PDGF which promotes cell division of the smooth muscle cells in the intima, causing a gradual intimal thickening.

The mathematical form of the stress for a Newtonian fluid given a pressure p, dynamic viscosity μ_l under a given flow $\mathbf{V}$ is given by

$$\mathbf{T} = -p\mathbf{I} + \mu_l(\nabla\mathbf{V} + \nabla\mathbf{V}^T). \tag{2.7}$$

With $\mathbf{V} = (0, 0, w(x, y))$, the stress tensor takes the matrix form,

$$\mathbf{T} = \begin{pmatrix} -p & 0 & \mu_l w_x \\ 0 & -p & \mu_l w_y \\ \mu_l w_x & \mu_l w_y & -p \end{pmatrix}. \tag{2.8}$$

The shear stress on endothelium is

$$\tau = \mathbf{n} \cdot \mathbf{T} \cdot \mathbf{e}_z = \mu_l \left(n_1 w_x + n_2 w_y\right) \tag{2.9}$$

where $\mathbf{n}$ is the unit normal on $\partial\omega_1^{(1)}$ pointing into the lumen and $\mathbf{e}_z$ is the unit vector in the Z direction.

2.2 Hyperelasticity and Morphoelasticity

To model the growth and deformation of the vessel layers when subjected to a constant pressure on the endothelium, we incorporated a hyperelastic model coupled with morphoelasticity. Hyperelasticity is one of the most common ways to describe nonlinear elasticity. It is commonly used for biological tissue modeling [27] and relies on the existence of a strain energy density function W. In our problem, we use a strain energy density function that incorporates a neo-Hookean response, a penalty term to penalize elastic deformations for near-incompressible materials, and a term that registers the energy contribution from collagen fibers. The form for W is motivated by the Holzapfel-Gasser-Ogden (HGO) model for a nearly-incompressible material [27, 16].

2.2.1 Energy functional

An energy functional represents the stored energy of a vessel undergoing deformation governed by the deformation gradient tensor $\mathbf{F} = \nabla\mathbf{\Phi} = \mathbf{I} + \nabla\mathbf{u}$. Here, $\mathbf{\Phi} = \mathbf{X} + \mathbf{u}$ is a mapping from the reference stress free configuration to the grown deformed configuration as shown in Fig. 2.1 and $\mathbf{u}$ is the displacement field. We minimize the energy functional with respect to the displacement field $\mathbf{u}$ to get the optimal displacement that minimizes a total energy. In this paper, the energy functional is always defined with respect to the reference stress free configuration. We also incorporate growth into our model [20]. A pure growth of a domain results in overlapping elements, which results in a non-physical or non-realistic configuration. As a result, the grown body undergoes strain to accommodate elements so that they do not overlap: in many situations, a growth simultaneously induces an elastic response. Thus, we assume that the deformation tensor $\mathbf{F}$ can be decomposed into a growth deformation tensor $\mathbf{F}_g$ followed by an elastic response tensor $\mathbf{F}_e$:

$$\mathbf{F} \;=\; \mathbf{F}_e\mathbf{F}_g. \tag{2.10}$$

We will assume that the growth deformation tensor takes the form

$$\mathbf{F}_g \;=\; \begin{pmatrix} g(x,y,t) & 0 & 0 \\ 0 & g(x,y,t) & 0 \\ 0 & 0 & 1 \end{pmatrix}. \tag{2.11}$$

We assume isotropic growth in the $x-y$ plane and no growth in the z direction.

The energy functional takes the form [11]

$$\Pi[\mathbf{\Phi}] = \sum_{k=1}^{3} \int_{\Omega_k} J_g^{(k)} \cdot W_k(\mathbf{F}_e)\, dA + \frac{P}{2} \int_{\partial\Omega_1^{(1)}} \mathrm{Cof}(\mathbf{F})\, \mathbf{N} \cdot \mathbf{\Phi}\, ds. \tag{2.12}$$

where $\mathbf{F}_e$ is the elastic component of the deformation gradient, $J = \det(\mathbf{F})$, $J_g^{(k)} = \det(\mathbf{F}_g^{(k)})$; for $k = 1$ (intima), $\mathbf{F}_g^{(k)} = \mathbf{F}_g$ (Eq. 2.11) and for $k = 2,3$ (media and adventitia, respectively), $\mathbf{F}_g^{(k)} = \mathbf{I}$; P is the pressure applied on the endothelium, $\mathbf{n}$ is the unit normal on the endothelium in the direction of the lumen, $\mathrm{Cof}(\mathbf{F}) = J\mathbf{F}^{-T}$, and W_k is the strain energy density function as defined in Eq. (2.14) below.

Since $\mathbf{\Phi} = \mathbf{X} + \mathbf{u}$, we can write the above equation in terms of $\mathbf{u}$ as

$$\Pi[\mathbf{u}] = \sum_{k=1}^{3} \int_{\Omega_k} J_g^{(k)} \cdot W_k(\mathbf{F}_e)\, dA + \frac{P}{2} \int_{\partial\Omega_1^{(1)}} \mathrm{Cof}(\mathbf{F})\, \mathbf{N} \cdot (\mathbf{X} + \mathbf{u})\, ds. \tag{2.13}$$

Therefore, solving for $\nabla\Pi[\mathbf{u}]\mathbf{u}' = 0$ for all test functions $\mathbf{u}'$ gives the optimal displacement $\mathbf{u}$. Fok and Gou [11] show that minimizing $\Pi[\mathbf{u}]$ is equivalent to minimizing the stress formulation of $\Pi[\mathbf{\Phi}]$.

The strain energy functions for the intima, media and adventitia are represented by W_1, W_2 and W_3 respectively [11]:

$$\begin{aligned} W_k = {} & \underbrace{\mu_k(I_1 - 3)}_{\text{Neo-Hookean term}} + \underbrace{\frac{\nu\mu_k}{1-2\nu}(J_e - 1)^2}_{\text{Penalty term}} - \underbrace{\mu_k \ln J_e}_{\text{Auxiliary term}} \\ & + \underbrace{\frac{\eta_k}{\beta_k}\left(\exp\left[\beta_k(1-\rho_k)(I_1-3)^2 + \beta_k\rho_k(I_4-1)_+^2\right] - 1\right)}_{\text{Energy contribution of stretched collagen fibers}} \end{aligned} \tag{2.14}$$

for k=1, 2, 3 representing the intima, media, and the adventitia, respectively [27].

In the above equation, μ_k, β_k, ρ_k, and η_k are layer-specific material constants (see Table 2.1 for their values), and ν measures the incompressibility of the material; $\nu \to 0.5$ corresponds to an incompressible material, whereas a substantially lower value of ν implies a compressible material. Since biological tissues are mostly composed of water, they are often modeled as being nearly incompressible. Furthermore, I_1, I_4 and J_e are defined as follows (physical significance discussed below):

$$I_1 = \mathrm{Tr}(\mathbf{F}_e^T \mathbf{F}_e) \tag{2.15}$$

$$I_4 = \mathbf{b}(X,Y)^T \mathbf{F}_e^T \mathbf{F}_e \mathbf{b}(X,Y) \tag{2.16}$$

$$J_e = \det(\mathbf{F}_e) \tag{2.17}$$

where $(X,Y) \in \Omega_k$ and $\mathbf{b}(X,Y)$ are the unit fiber vectors at (X,Y) in the reference stress free domain [47]. The fibers are inclined at an angle with respect to the cross section. For each of the layers, the inclination angles, ϕ_k, take on different values (see Table 2.1 for values of ϕ_k).

The auxiliary term ensures that the stress in the reference stress free configuration is zero [58]. The penalty term penalizes large deformations (corresponding to J_e being far away from 1) when $\nu \approx 0.5$. For ensuring incompressibility, we assume $\det(\mathbf{F}) = J = \det(\mathbf{F}_e)\det(\mathbf{F}_g) = J_e J_g$. If $J_e \approx 1$, then the amount by which elements grow or shrink is controlled by J_g, the determinant of the growth tensor $\mathbf{F}_g$.

In Eqs. (2.15, 2.17), I_1 and I_4 are invariants under rotations and translations. The invariant I_1 registers the resultant stretch of an infinitesimal element, from the reference stress free configuration to the grown deformed configuration, in the direction of the principal axes. The invariant I_4 is the normalized length of the collagen fibers projected onto the plane of the cross section. In the stress free configuration, either the fibers are not stretched or are coiled up, representing $I_4 = 1$. We want to register only the tensile contribution. The contribution of the collagen fibers in the last term of the strain energy function takes effect only if the normalized fiber length $I_4 > 1$, i.e., when the fibers are stretched. Therefore, we introduce $(I_4 - 1)_+^2$ as

$$(I_4 - 1)_+^2 \quad = \quad \begin{cases} 0\,, & \text{if } I_4 \leq 1, \\ (I_4 - 1)^2\,, & \text{if } I_4 > 1. \end{cases} \tag{2.18}$$

If $\mathbf{\Phi}$ is a map from the reference to the grown deformed configuration, the strain energy density function is a function of $\nabla\mathbf{\Phi}$. Then the strain energy functional, $\Pi[\mathbf{\Phi}]$, is an integral consisting of $W(\nabla\mathbf{\Phi})$ as defined in Eq. (2.14), that registers the total energy stored in the grown deformed configuration due to a displacement $\mathbf{u}$ of the arterial layers. The strain energy density functional is minimized with respect to $\mathbf{u}$ (since $\nabla\mathbf{\Phi} = \mathbf{I} + \nabla\mathbf{u}$, minimizing $\Pi[\mathbf{\Phi}]$ with respect to $\mathbf{u}$ is the same as minimizing it with respect to $\mathbf{\Phi}$). The minimizer gives the minimum energy deformation of the vessel walls. However, the minimizer need not be unique in general. The polyconvexity of the strain energy density functions W_k guarantees the existence of at least one minimizer (see [11] for more details).

A proper selection of the appropriate values of the material parameters for the strain energy function is essential for an accurate analysis of the behavior of vessels under loading. In this thesis, the values of the parameters are taken from [27], where Holzapfel *et. al.* provided a range of values for the parameters and their standard deviations based on extensive experimental results. We took the mean values of the parameters. The parameter values are given in the below table.

Parameters	Meaning	Values
μ_1	Intima shear modulus	27.9 kPa
η_1	Intima material parameter	263.66 kPa
β_1	Intima material parameter	170.88
ϕ_1	Fiber angle in intima	60.3°
ρ_1	Intima material parameter	0.51
μ_2	Media shear modulus	1.27 kPa
η_2	Media material parameter	21.6 kPa
β_2	Media material parameter	8.21
ϕ_2	Fiber angle in media	20.61°
ρ_2	Media material parameter	0.25
μ_3	Adventitia shear modulus	7.56 kPa
η_3	Adventitia material parameter	38.57 kPa
β_3	Adventitia material parameter	85.03
ϕ_3	Fiber angle in adventitia	67°
ρ_3	Adventitia material parameter	0.55
ν	Measure of incompressibility	0.49

Table 2.1: Material parameters and their values. The parameters μ_k, ρ_k, β_k, and η_k roughly capture the stiffness of the different layers.

The material parameters in the above table govern the mechanical response of the arterial wall due to pressure and growth. One of the important and interesting avenues to explore is the sensitivity of the parameters to the mechanical response of the arterial wall to growth and deformation. However, such an analysis is not the focal point of this thesis and thus is beyond the scope.

2.3 PDGF Transport

As mentioned previously, Platelet-Derived Growth Factor (PDGF) is released by endothelial cells when they experience shear stress. PDGF promotes migration and cell division of smooth muscle cells (SMCs) within the arterial wall. A healthy intima starts with a single layer of endothelial cells. With time, there is migration of SMCs from the media to the intima. These SMCs come in contact with PDGF and proliferate to make the intima thicker over time. A good review of the biology of PDGF can be found in [65] where Reidy *et. al.* found little effect of PDGF on SMCs proliferation but instead induces a migration of SMCs from the media to the intima.

In practice, it is difficult to measure the distribution of PDGF in tissues, making it difficult to create a mathematical model for PDGF dynamics. PDGF is a dimer with A and B subunits. Therefore, proxies for PDGF such as PDGF A mRNA and PDGF B mRNA levels are measured for different shear stress levels [29]. In this thesis, we have considered the response of PDGF A mRNA level to shear stress as a model for the PDGF dynamics.

2.3.1 Diffusion-Degradation Model for PDGF

Let $C(x, y, t)$ be the concentration of PDGF. Since the diffusion and degradation of PDGF happen at a time scale that is much much smaller compared to the time scale of plaque growth, we can consider a steady state diffusion-degradation equation for the PDGF in the arterial wall:

$$\begin{aligned} D\nabla^2 C - kC &= 0, \qquad (x,y) \in \omega_1 \cup \omega_2 \cup \omega_3, && (2.19)\\ -D\frac{\partial C}{\partial \mathbf{n}} &= \zeta_1 m, \qquad (x,y) \in \partial\omega_1^{(1)}, && (2.20)\\ C &= 0, \qquad (x,y) \in \partial\omega_3^{(2)}. && (2.21) \end{aligned}$$

where D is the diffusivity of PDGF, k is its degradation rate, $\mathbf{n}$ is the unit normal on the endothelium pointing into the lumen, and m is the relative PDGF A mRNA level.

For finding the diffusion-degradation equation of the PDGF concentration C, there are two parameters that need to be determined; the degradation constant k and the relative PDGF A mRNA level m. In Eq. (2.20), we assume that the flux of PDGF across the endothelium is proportional to PDGF A mRNA level (which depends on the shear stress as discussed below) with ζ_1 being the constant of proportionality. This equation is inspired by [29], in which Hsieh *et. al.* study the effect of shear stress on the relative PDGF A mRNA and PDGF B mRNA levels. The authors report that when subjected to an increase of shear stress, the increase in PDGF A mRNA level was dominant compared to PDGF B mRNA level. So, we considered the flux of PDGF to be proportional to the relative PDGF A mRNA level and discarded the relative PDGF B mRNA level.

In this work, we model the PDGF A mRNA level (m) as a saturating function of the shear stress: $m = \zeta_2 \dfrac{\tau}{\tau + \tau_0}$, where τ is the shear stress due to a Poiseuille blood flow and τ_0 is the baseline shear stress. Therefore, the Neumann boundary condition in Eq. (2.20) becomes

$$-D\frac{\partial C}{\partial \mathbf{n}} = \zeta_1\zeta_2\frac{\tau}{\tau+\tau_0} = J_{\max}\frac{\tau}{\tau+\tau_0}. \tag{2.22}$$

The value of diffusivity $D = 0.01\ \mathrm{mm}^2/\mathrm{h}$ is taken from [22]. We leave the degradation constant k to be a free variable. We assume that the values of D and k are the same across all the vessel layers.

To our knowledge, there are no studies that investigate how PDGF flux varies with respect to laminar wall shear stress on the endothelium. However, in [29], Hsieh *et. al.* study the relative PDGF A mRNA and PDGF B mRNA levels due to shear stress in cultured human umbilical vein endothelial cells. The authors observed that the PDGF A mRNA level increased in a shear-dependent manner when the veins were subjected to an increasing shear stress ranging from 0 to 6 dyne/cm^2 and then plateaued between 6 and 51 dyne/cm^2. For finding the PDGF flux, two parameters need to be determined: τ_0 and $J_{\max}$. We determine τ_0 by fitting data on relative PDGF A mRNA level from the experiments in [29]. This article studies the effect of shear stress on the relative PDGF A mRNA and PDGF B mRNA levels but does not report the effect of shear stress on PDGF levels. The maximum flux $J_{\max}$ can be determined from [71]. In this paper, Shankar *et. al.* compare the production of PDGF by human umbilical vein endothelial cells by synthetic peptide ligands and thrombin. The cultured cells were put in 12-well plates, with each well containing approximately 2×10^5 cells, and incubated with thrombin and thrombin receptor peptides for 24 hours. The PDGF level (ng/well/24 h) was then reported.

In [29], let R_i be the relative PDGF A mRNA level for the shear stress $\tau^{(i)}$ (the index i refers to each of the 8 observations made by Hsieh *et. al.*). We then performed a least squares fit to the residual

$$res(\chi, \tau_0) = \sum_{i=1}^{8} \left| R_i - \chi \frac{\tau^{(i)}}{\tau^{(i)} + \tau_0} \right|^2$$

By performing two-parameter least squares for χ and τ_0, we obtained the optimal values $\tau_0 = 0.32$ Pa and $\chi = 44.62$ that minimized the above residual: see Fig. 2.2 below

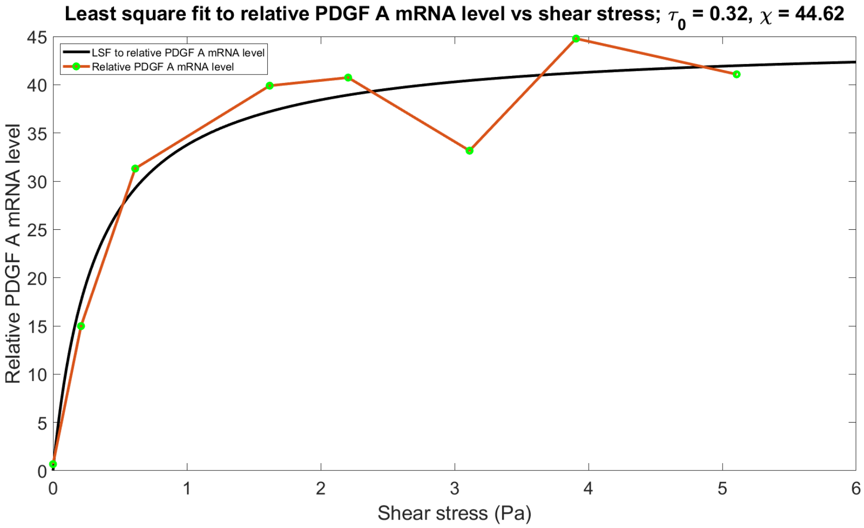

Figure 2.2: PDGF flux as a response to the shear stress at the endothelium. The flux saturates as the shear stress increases. The flux is approximated by the equation $-D\frac{\partial C}{\partial \mathbf{n}} = J_{\max}\frac{\tau}{\tau + \tau_0}$ with $D = 0.01$ mm^2/h. We performed a two-parameter (χ and τ_0) least squares fit. The optimal values for the two-parameter least squares fit were $\chi = 44.62$ and $\tau_0 = 0.32$ Pa.

We are now interested in finding the maximum PDGF flux $J_{\max}$ from [71]. We took the mean value of the control (1.33 ng/well/24 h) to be the value for $J_{\max}$ and scaled it to ng/mm^2/h using the fact that a well consists of 2×10^5 cells approximately [71]. The human vasculature is fractal in nature [14], giving rise to an enormous surface area. In the article [37], Krüger-Genge *et. al.* mention that about 6×10^{13} endothelial cells cover a total surface area of 6000 m^2. Assuming that 6000 m^2 of surface area is covered by 6×10^{13} endothelial cells, 1 cell occupies approximately $\dfrac{6000\ \text{m}^2}{6 \times 10^{13}} = 0.0001\ \text{mm}^2$. Then as a result, 1.33 ng/well/24 h is equivalent to $\dfrac{1.33}{(2 \times 10^5) \times 10^{-4}(24)} = 0.003\ \text{ng/mm}^2/\text{h}$. With this reduced value of $J_{\max}$, we get the relation between shear stress and PDGF flux as illustrated in Fig. 2.3

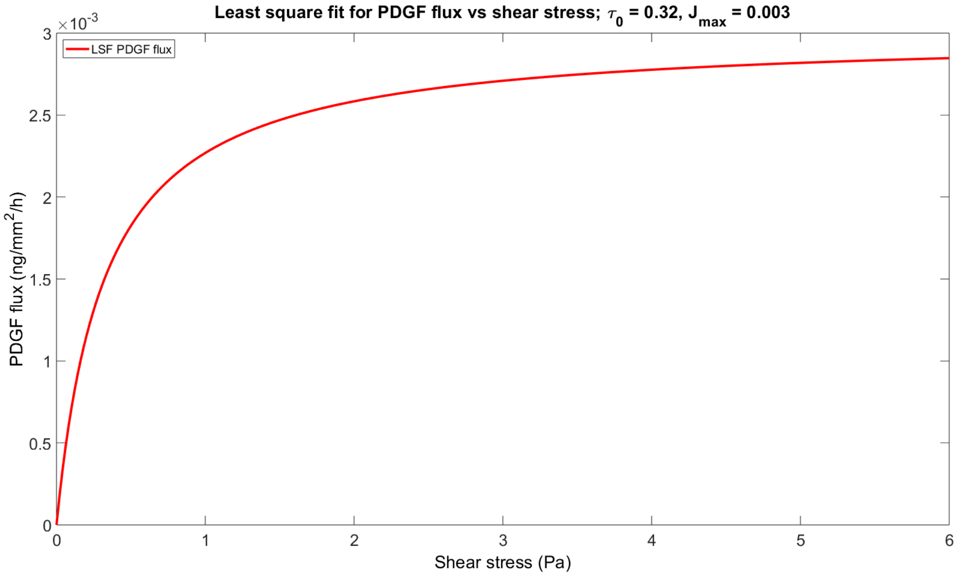

Figure 2.3: PDGF flux as a response to the shear stress at the endothelium. The flux saturates as the shear stress increases. The flux is approximated by the equation $-D\dfrac{\partial C}{\partial \mathbf{n}} = J_{\max}\dfrac{\tau}{\tau + \tau_0}$ with $D = 0.01\ \text{mm}^2/\text{h}$, $J_{\max} = 0.003\ \text{ng/mm}^2/\text{h}$, and $\tau_0 = 0.32$ Pa.

The material parameters considered in our model are given in Table. 2.1. The Table. 2.2 below refers to the physical parameters along with their meanings.

Physical parameters	Meaning	Values
G	Pressure gradient across the vessel	0.013 kPa/mm
ν_l	Dynamic viscosity of blood	4×10^{-6} kPa.s
k	PDGF degradation rate constant	$0.0002\ \mathrm{h}^{-1}$
D	PDGF diffusivity	$0.01\ \mathrm{mm}^2/\mathrm{h}$
$J_{\max}$	Maximum PDGF flux	$0.003\ \mathrm{ng/mm}^2/\mathrm{h}$
τ_0	Baseline shear stress	0.3×10^{-3} kPa
α	Growth rate	0.5/year
C_0	Baseline PDGF concentration	$0.01\ \mathrm{ng/mm}^2$

Table 2.2: Physical parameters and their values.

2.4 Growth of the intima

Since PDGF promotes cell division, we define the growth rate $\gamma(x, y)$ to be

$$\gamma(x,y) = \alpha \frac{C^m}{C_0^m + C^m}, \quad (x,y) \in \omega. \tag{2.23}$$

for some constant C_0, a Hill coefficient m, and a reference growth rate α. We have chosen a Hill function assuming that the rate of growth saturates for large PDGF concentration.

For the intima, media, and the adventitia, the growth tensor takes the form

$$\mathbf{F}_g = \begin{pmatrix} 1+\gamma t & 0 & 0 \\ 0 & 1+\gamma t & 0 \\ 0 & 0 & 1 \end{pmatrix} \tag{2.24}$$

We assume that there is no growth in the axial direction which implies that the entry in the (3,3) position of $\mathbf{F}_g$ is 1.

In this thesis, we have chosen $m = 4$, $C_0 = 0.01$ ng/mm^2, and $\alpha = 0.5$/year. Since the $(1,1)$ and $(2,2)$ components of $\mathbf{F}_g$ are the same, the growth is isotropic in the x and y directions.

Chapter 3

COMPUTING FIBER FIELDS USING NUMERICAL CONFORMAL MAPS

An arterial vessel has three layers, namely, the intima, the media and the adventitia. Each of these layers is modeled to have two families of strain-stiffening collagen fibers that are transversely helical. In an unloaded configuration, these fibers are coiled up. In the case of a pressurized lumen, these fibers stretch and start to resist further outward expansion. As the fibers elongate, they stiffen, affecting the mechanical response. Having a mathematical model of vessel expansion is crucial in cardiovascular applications such as predicting stenosis and simulating hemodynamics. Thus, to study the mechanics of the vessel wall under loading, it is important to calculate the fiber configurations in the unloaded configuration. The aim of this section is to introduce a new technique of using conformal maps to numerically calculate the fiber field in a general arterial cross-section. The technique relies on finding a rational approximation of the conformal map. First, points on the physical cross section are mapped to points on a reference annulus using a rational approximation of the forward conformal map. Next, we find the angular unit vectors at the mapped points, and finally a rational approximation of the inverse conformal map is used to map the angular unit vectors back to vectors on the physical cross section. We have used MATLAB software packages to achieve these goals.

Cardiovascular diseases, leading to heart attacks (myocardial infarction) and stroke, are among the prime causes of mortality in modern society. Often increased stress levels, lack of exercise and many other factors are associated with cardiovascular disorders. Myocardial infarction is one of the most common causes of fatality and occurs when blood flow to the heart muscles is blocked. It has been the subject of many investigations over the past few decades [72, 61, 78, 73, 46].

One of the most important factors behind myocardial infarction is the blockage of arteries (stenosis). As coronary arteries undergo blockage, the heart experiences more pressure to maintain the blood flow, resulting in increased stress on the heart muscles, usually leading to heart failure. Thus, it is of prime importance to provide a mathematical model that can capture the dynamics of stenosis, and a crucial component of these models is an accurate mechanical model of the artery [15]. For the mechanical model, we need a strain energy density function from which we can calculate the lowest energy deformation; from the strain energy function, the stress response of a hyperelastic material can be derived (see [24], Chapter 6). The mathematical form of the strain-energy density function for nearly incompressible arterial tissue consists of several terms: a neo-Hookean term and a contribution from collagen fibers [11]. In general, the strain energy density function takes the form

$$W = W_{NH}(I_1) + W_{aniso}(I_1, I_4, I_4^*) \tag{3.1}$$

where $W_{NH}(I_1) = \mu(I_1 - 3)$ is a neo-Hookean function of $I_1 = \text{Trace}(\mathbf{C})$ with μ being a layer-specific material parameter, $\mathbf{C} = \mathbf{F}^T\mathbf{F}$ is the right Cauchy-Green tensor that registers the deformation from the reference to the deformed domain, and $\mathbf{F}$ is the deformation gradient. A commonly used term for $W_{aniso}(I_1, I_4, I_4^*)$ is

$$\begin{aligned} W_{aniso}(I_1, I_4, I_4^*) = \frac{\eta}{2\beta} \exp[\beta(1-\rho)(I_1-3)^2 + \beta\rho(I_4-1)_+^2] \\ + \frac{\eta}{2\beta} \exp[\beta(1-\rho)(I_1-3)^2 + \beta\rho(I_4^*-1)_+^2]. \end{aligned} \tag{3.2}$$

The term $W_{aniso}(I_1, I_4, I_4^*)$ registers the anisotropy of the model [28, 68] due to the presence of two families of collagen fibers with normalized lengths I_4 and I_4^* (see Section 3.1 below for more details). The constants ρ, η and β refer to the material constants of each of the layers. The other prime factor to consider while taking into account the dynamics of stenosis is the stiffness of the collagen fibers. In Eq. (3.2), $\beta\rho$ determines the stiffness of a layer. A higher value of $\beta\rho$ implies a higher degree of stiffness compared

to a lower value of $\beta\rho$. The degree of stiffness could dictate the rate of lumen occlusion due to intimal growth [44].
In a healthy coronary artery, the intima consists of a single layer of smooth muscle cells (SMCs) and no collagen fibers. Over time there is an influx of SMCs from the media into the intima. A gradual thickening of the intima occurs when the SMCs undergo cell division. The proliferation of the SMCs in the intima and accumulation of lipids result in the formation of lesions. Katsuda *et. al.* [34] observed localization of collagen fibers around the lesions.

Although there is no histological evidence of transverse helical collagen fibers in the intima, studies like [11, 28] have assumed a two-family fiber model for the strain energy functional for the intima.

It is of significant importance to model the orientation of the fiber fields and predict how they change in order to describe accurately the response of the arterial walls due to loading. Computational techniques to explicitly compute fiber fields in general arterial cross sections using non-probabilistic approaches are rarely documented. In this study, we introduce conformal maps as an alternative to interpolation techniques when it comes to modeling fiber fields in 2D vessel cross sections.

Over the past few decades, some intensive investigations have been carried out to simulate and provide models for the distribution of fibers in the layers of an arterial vessel. When it comes to the myocardium, fibers also play an important role, and there have been many studies that attempt to numerically construct fiber fields within the myocardial wall. In [59], Plank *et. al.* introduce a Laplace-Dirichlet Rule-Based (LDRB) algorithm to assign fiber orientations to heart models. In this study, the authors use linear interpolation for calculating fiber orientations within the myocardium. Deterministic techniques like interpolation are very common when modeling fibers in the heart. In [79], Wong and Kuhl solve a Poisson equation subjected to the Dirichlet conditions that the fiber orientations in the heart vary gradually from $-70°$ to $80°$ from the outer to the inner wall. Theofilogiannakos *et. al.* [75] study a post-mortem human heart. They reconstruct a continuous fiber field from experimental measurements of the actual fiber direction at a set of discrete points within each slice. In [1], Akyildiz *et. al.* perform a diffusion tensor imaging (DTI) of seven carotid plaques. They observe that in advanced stage carotid plaques, the predominant fiber orientation is in the circumferential direction, with the elevation angle being zero or close to zero.

Fibers also play an important role in governing the dynamics and mechanics of an arterial wall. Microscopically, fibers are oriented helically around the lumen and are mostly aligned with wall boundaries with a small amount of dispersion [52]. Therefore, in studies of vessels that have annular cross sections, fiber fields are assigned to the circumferential direction by simply computing the unit tangential vector. However, in reality, arterial cross sections are not perfectly annular. In such cases, the fiber orientations are sometimes modeled using interpolation techniques similar to the ones discussed above for myocardial tissue. For example, Fok and Gou [11] calculated the fiber orientations as weighted averages of the tangent vectors on the Jordan boundaries (simple closed curves homeomorphic to a unit circle) of an arterial layer.

In addition to several interpolation models for computing and simulating fiber orientations, there are several studies on probabilistic approaches for computing fiber field orientations. In [15], structural continuum frameworks are developed, taking into account the dispersion of the collagen fiber orientations. A probability density function of the fiber orientation in the reference frame is used in [26] for the construction of the strain energy function. Another study [69] used maximum-likelihood estimation to determine the angle of the fibers along with a model to quantify collagen fiber dispersion. Similarly, in [36], a density function describing the distribution of the collagen fibers is incorporated into the strain energy function, and it evolves as the fibers orient themselves in the direction of the maximum Cauchy stress. Cacho *et. al.* [3] establish a relationship between the fiber end points and their arc lengths, which is estimated from image data. The mechanical response of collagen fibers, subjected to stress, is determined by a random variable approximated by a beta distribution. There is also open source software, FEBio (https://febio.org/), that simulates fiber orientations using probability distributions. In FEBio, a random distribution of fiber orientation is assigned to the points on the domain, and the average strain energy density function is calculated (https://help.febio.org/FebioUser/FEBio_um_3-4-Section-4.3.html). The type of distribution function can be chosen from a range of distribution functions, which provides one with options of selecting spherical, ellipsoidal, circular, elliptical, von Mises and π-periodic von Mises distributions according to the geometry under consideration (https://help.febio.org/FebioUser/FEBio_um_3-4-Subsection-4.3.3.html).

3.1 The collagen fibers

We consider an infinitely long cylindrical artery that has its cross section aligned with the X-Y plane, and every cross section is mechanically and geometrically identical for every Z. Each of the three layers of an artery (intima, media and adventitia) has transverse helical collagen fibers associated to it as shown in the Fig. 3.1

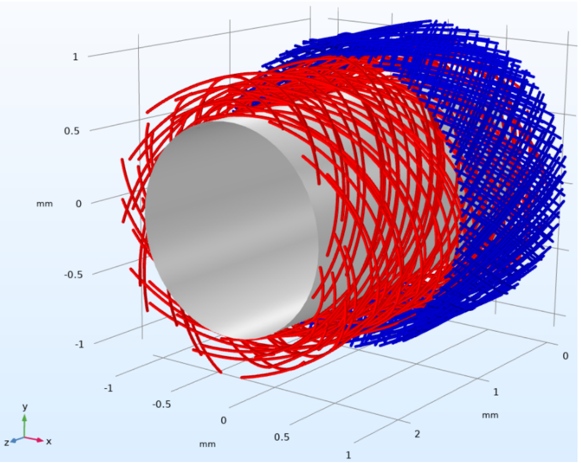

Figure 3.1: Schematic diagram of transversely helical collagen fibers. **Image credit:** https://www.comsol.com/blogs/using-curvilinear-coordinates/

These collagen fibers offer resistance to the expansion of the arteries. In the reference configuration, they remain in their lowest energy state. As soon as the arteries start to dilate under pressure, the collagen fibers start to uncoil, offering resistance to further dilation of the artery. As the collagen fibers stiffen gradually, it takes more and more energy to dilate the vessel. The collagen fibers have an inclination angle that is independent of the Z axis. Inclination angle is the angle made by the transversely helical collagen fibers with respect to the X-Y plane. To incorporate the effect of the collagen fibers on deformation, we introduce a variable I_4 for each of the layers, intima, media and adventitia. I_4 is the normalized length of the collagen fibers. As the vessel is loaded, I_4 increases. However, in reality, there are two families of fibers. One family is oriented at an angle ϕ, with respect to the axial direction, while the other is oriented at an angle $\pi - \phi$. We introduce I_4 and I_4^* to represent fiber lengths for each family:

$$I_4 = \mathbf{b}(X,Y)^T \mathbf{C} \mathbf{b}(X,Y), \quad I_4^* = \mathbf{b}^*(X,Y)^T \mathbf{C} \mathbf{b}^*(X,Y). \tag{3.3}$$

where $\mathbf{b} = \begin{bmatrix} b_1 & b_2 & b_3 \end{bmatrix}^T$ and $\mathbf{b}^* = \begin{bmatrix} b_1 & b_2 & -b_3 \end{bmatrix}^T$ are the unit fiber vectors at the point (X,Y) in the reference stress-free/unloaded domain corresponding to each of the families of the fibers. In our work, since we ignore the residual stresses, the stress-free configuration is the same as the unloaded configuration. From the definitions of $\mathbf{b}$ and $\mathbf{b}^*$, we see that $I_4 = I_4^*$. Hence, W_{aniso} in Eq. (3.2) only depends on I_1 and I_4 and takes the form

$$W_{aniso}(I_1, I_4, I_4^*) = \frac{\eta}{\beta} \exp[\beta(1-\rho)(I_1-3)^2 + \beta\rho(I_4-1)_+^2]. \tag{3.4}$$

The inclination angle, ϕ, is different for each layer, so the length of the fiber, projected onto the X-Y plane, is also different for each layer. In the reference stress-free/unloaded configuration, $I_4 = 1$ since $\mathbf{C} = \mathbb{1}$, and $\mathbf{b}$ is a unit vector. $\mathbf{Fb}$ gives us the deformation of the unit fiber vector in the deformed configuration.

3.2 Numerical conformal mapping

The function $\mathbf{b}(X,Y)$ for any physical cross section is not easy to calculate for a general point (X,Y). In the previous section, we explored different strategies for computing $\mathbf{b}(X,Y)$. Since the calculation is done numerically, many algorithms prove to be computationally intensive. The main idea here is to come up with a new approach using numerical conformal maps to calculate $\mathbf{b}(X, Y)$.

We introduce a reference annulus with inner radius ρ and outer radius 1, with $0 < \rho < 1$. Given a physical cross section, the idea is to construct a conformal map that maps the physical cross section to the reference annulus.

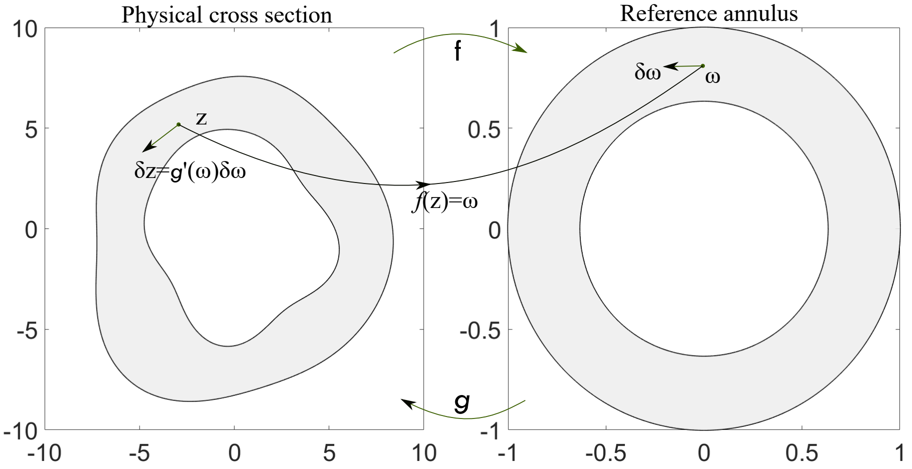

Figure 3.2: Conformal mapping of fiber fields between the reference annulus and the physical cross section. f is the forward conformal map from the physical cross section to the reference annulus, and g is the inverse conformal map from the reference annulus to the physical cross section. We map z to ω using f, find the unit fiber vector $\delta\omega$ in the reference annulus and map it back to the fiber vector δz in the physical cross section using the derivative of the inverse conformal map g.

There are a few reasons behind choosing conformal maps. First, the fiber field in the reference annulus is very easy to compute. For any point (U, V) on the annulus, the unit fiber direction vector can be derived easily by calculating the vector $\begin{bmatrix} -\sin(\theta) & \cos(\theta) \end{bmatrix}^T$, where $\theta = [arctan(V, U)]$; $arctan$ is the four-quadrant arctangent. The other advantage of a conformal map is that it preserves angles locally. The fiber fields in a general cross section should satisfy some basic properties. First, fiber vectors at the boundaries between the intima, media and adventitia should be tangential: We assume that the fibers from one layer do not penetrate the adjacent layers. Second, the field should vary smoothly across the layers of the vessel. A smooth fiber field is essential for the strain-energy function to be well defined. General maps that are not conformal will not preserve angles: They can map tangential vectors in the annulus to non-tangential vectors in the physical cross section. However, for conformal maps, vectors tangent to boundaries remain tangential. Thus, the aim is to create a conformal map from the reference annulus to the physical cross section as shown in Fig. 3.2.

Since the fiber field in the reference annulus can be computed easily, we can find the fiber field in the physical cross section simply by multiplying the unit fiber vector $\delta\omega$ with the derivative of the inverse conformal map:

$$\delta z = g'(\omega)\delta\omega \tag{3.5}$$

where $\delta\omega = -\sin\theta + i\cos\theta$ is the unit fiber vector on the reference annulus at the point ω, δz is the fiber vector in the physical cross section, and g is the inverse conformal map from the reference annulus to the physical cross section. The projected vector is proportional to $[\mathfrak{Re}(\delta z)\ \ \mathfrak{Im}(\delta z)]^T$. This vector is inclined at an angle ϕ. Therefore, $\mathbf{b} \propto \left[\mathfrak{Re}(\delta z)\ \ \mathfrak{Im}(\delta z)\ \ \sqrt{\mathfrak{Re}^2(\delta z) + \mathfrak{Im}^2(\delta z)}\tan\phi\right]^T$. Therefore, in order for $\mathbf{b}$ to have unit length, we can write

$$\mathbf{b} = \begin{bmatrix} b_1(X,Y) \\ b_2(X,Y) \\ b_3(X,Y) \end{bmatrix} = \begin{bmatrix} \mathfrak{Re}(\delta z) \\ \mathfrak{Im}(\delta z) \\ \sqrt{\mathfrak{Re}^2(\delta z) + \mathfrak{Im}^2(\delta z)}\tan\phi \end{bmatrix} \Bigg/ L \tag{3.6}$$

where $L = \sqrt{(1+\tan^2\phi)(\mathfrak{Re}^2(\delta z) + \mathfrak{Im}^2(\delta z))}$, and ϕ is the inclination angle of the fibers in each of the layers. In the study [28], Holzapfel *et. al.* inferred the inclination angles (along with other material constants) by fitting to stress-strain data. They showed that in human coronary arteries, $\phi \approx 60.3°$, $20.61°$ and $67°$ for the intima, media and adventitia, respectively.

3.3 Analytic functions and AAA approximation

Let's consider simply connected domains as a first step to understanding the method. The idea [77] is to construct the unique conformal map $f : \Omega \mapsto D$, with Ω being a smooth simply connected domain bounded by a Jordan curve P and D being the open unit disk, such that $f(0) = 0$ and $f'(0) > 0$. Then, $h(z) = \log(f(z)/z)$ is a non-zero analytic function on Ω that is continuous on $\bar{\Omega}$ and can be written as $h(z) = u(z)+iv(z)$, where $u(z)$ and $v(z)$ are real harmonic functions in Ω and continuous on $\bar{\Omega}$. Any point $z_p = re^{i\theta}$ on the Jordan boundary P is mapped to $f(z_p) = e^{i\psi}$, where $\psi \in \mathbb{R}$, with $|f(z_p)| = 1$. Then, $u(z_p) + iv(z_p) = i(\psi - \theta) - \log r$, where r, $\theta \in \mathbb{R}$ for $z_p \in P$.
Writing $f(z)$ in terms of $h(z)$, we get

$$f(z) = ze^{u(z)+iv(z)} \tag{3.7}$$

where $u(z)$ satisfies the Laplace equation with a Dirichlet boundary condition:

$$\Delta u = 0; \quad u(z) = -\log|z|, \quad z \in P. \tag{3.8}$$

In Eq. (3.7), $v(z)$ is a harmonic conjugate of $u(z)$ satisfying $v(0) = 0$. Solving Eq. (3.8) and finding its harmonic conjugate $v(z)$ gives the algebraic form of the conformal map $f(z)$ according to Eq. (3.7). The solution to Eq. (3.8) is approximated by the real part of a complex analytic function:

$$u(z) \approx \mathfrak{Re} \sum_{k=0}^{n} c_k z^k \tag{3.9}$$

for some n, where $c_k = a_k + ib_k$, a_k, $b_k \in \mathbb{R}$, and $b_0 = 0$, Therefore,

$$u(z) \approx \sum_{k=0}^{n} \Big(a_k \mathfrak{Re}(z^k) - b_k \mathfrak{Im}(z^k)\Big); \;\; b_0 = 0. \tag{3.10}$$

Since $z \in P$ and $u(z) = -\log|z|$, we plug in distinct points sampled from P into $-\log|z|$, forming the left-hand side of Eq. (3.10). For the right-hand side of Eq. (3.10), we get a weighted linear combination of a_k and b_k for each of the points $z \in P$.

To set up a least squares problem, let's sample $8n$ points on the Jordan curve P, $z_0, z_1, \ldots, z_{8n-1}$. Then, from Eq. (3.10), we get

$$\begin{bmatrix} 1 & \mathfrak{Re}(z_0) & -\mathfrak{Im}(z_0) & \ldots & \mathfrak{Re}(z_0^n) & -\mathfrak{Im}(z_0^n) \\ 1 & \mathfrak{Re}(z_1) & -\mathfrak{Im}(z_1) & \ldots & \mathfrak{Re}(z_1^n) & -\mathfrak{Im}(z_1^n) \\ \vdots & \vdots & \vdots & \vdots & \vdots & \vdots \\ 1 & \mathfrak{Re}(z_{8n-1}) & -\mathfrak{Im}(z_{8n-1}) & \ldots & \mathfrak{Re}(z_{8n-1}^n) & -\mathfrak{Im}(z_{8n-1}^n) \end{bmatrix} \begin{bmatrix} a_0 \\ a_1 \\ b_1 \\ \vdots \\ a_n \\ b_n \end{bmatrix} \approx \begin{bmatrix} -\log|z_0| \\ -\log|z_1| \\ \vdots \\ -\log|z_{8n-1}| \end{bmatrix} \tag{3.11}$$

The above matrix equation can be written in a compact form as $\mathbf{Ax} \approx \mathbf{d}$. Solving the least squares problem in Eq. (3.11), we get the coefficients $a_0, a_1, \ldots, a_n$ and $b_1, b_2, \ldots, b_n$. Plugging the coefficients into Eq. (3.10), we get $u(z)$, and since $v(z)$ is the harmonic conjugate of $u(z)$, it takes the form

$$v(z) \approx \sum_{k=0}^{n} \Big(a_k \mathfrak{Im}(z^k) + b_k \mathfrak{Re}(z^k) \Big). \tag{3.12}$$

Once we get $u(z)$ and $v(z)$, they can be substituted in Eq. (3.7) to get the conformal mapping $f(z)$.

For a smooth doubly connected domain, there are two Jordan boundaries P_1 and P_2, and we employ a similar strategy to the one above. However, there are differences in the formulation of the problem [77]. The strategy for a smooth doubly connected domain is to find a conformal map $f(z)$ that maps the domain to a circular annulus with inner radius ρ such that $0 < \rho < 1$, where ρ is known as the conformal modulus, and the outer radius is 1. If P_1 and P_2 are the outer and the inner Jordan boundaries, respectively, of the smooth doubly connected domain, then f satisfies $f(P_1) = S$ and $f(P_2) = \rho S$, where S is the unit circle. Note that ρ is an unknown that must be found. The approximation of $u(z)$ for a smooth doubly connected domain takes the form

$$u(z) \approx \mathfrak{Re} \sum_{k=-n}^{n} c_k z^k \tag{3.13}$$

where $c_k = a_k + ib_k$, for some $a_k,\ b_k \in \mathbb{R}$ and $b_0 = 0$. Since $v(z)$ is the harmonic conjugate of $u(z)$, we get

$$u(z) \approx \sum_{k=-n}^{n} \Big(a_k \mathfrak{Re}(z^k) - b_k \mathfrak{Im}(z^k) \Big) \tag{3.14}$$

$$v(z) \approx \sum_{k=-n}^{n} \Big(a_k \mathfrak{Im}(z^k) + b_k \mathfrak{Re}(z^k) \Big). \tag{3.15}$$

Thus, the Dirichlet boundary conditions for $u(z)$ will be

$$u(z) = \begin{cases} -\log|z|\ , & z \in P_1, \\ -\log|z| + \log\ \rho\ , & z \in P_2. \end{cases} \tag{3.16}$$

Similar to finding $u(z)$ for a smooth simply connected domain, we solve the Laplace equation $\Delta u = 0$ subjected to Dirichlet boundary conditions in Eq. (3.16) to find $u(z)$ and its harmonic conjugate $v(z)$. Since there are two Dirichlet boundary conditions for $u(z)$, we get two matrix equations. To set up a least squares problem, we sample $8n$ points from each of the Jordan boundaries. From P_1, we sample the points $z_{0,1}, z_{1,1}, z_{2,1}, \ldots, z_{8n-1,1}$. Similarly, for the Jordan boundary P_2, we sample the points $z_{0,2}, z_{1,2}, z_{2,2}, \ldots, z_{8n-1,2}$. Now, since $\log\rho$ is unknown, the conformal map can be found by solving the least squares system

$$\mathbf{Ax} \approx \mathbf{C} \tag{3.17}$$

where

$$\mathbf{A} = \begin{bmatrix} \mathfrak{Re}(z_{0,1}^{-n}) & -\mathfrak{Im}(z_{0,1}^{-n}) & \dots & \mathfrak{Re}(z_{0,1}^{n}) & -\mathfrak{Im}(z_{0,1}^{n}) & 0 \\ \mathfrak{Re}(z_{1,1}^{-n}) & -\mathfrak{Im}(z_{1,1}^{-n}) & \dots & \mathfrak{Re}(z_{1,1}^{n}) & -\mathfrak{Im}(z_{1,1}^{n}) & 0 \\ \vdots & \vdots & \vdots & \vdots & \vdots & \vdots \\ \mathfrak{Re}(z_{8n-1,1}^{-n}) & -\mathfrak{Im}(z_{8n-1,1}^{-n}) & \dots & \mathfrak{Re}(z_{8n-1,1}^{n}) & -\mathfrak{Im}(z_{8n-1,1}^{n}) & 0 \\ \mathfrak{Re}(z_{0,2}^{-n}) & -\mathfrak{Im}(z_{0,2}^{-n}) & \dots & \mathfrak{Re}(z_{0,2}^{n}) & -\mathfrak{Im}(z_{0,2}^{n}) & -1 \\ \mathfrak{Re}(z_{1,2}^{-n}) & -\mathfrak{Im}(z_{1,2}^{-n}) & \dots & \mathfrak{Re}(z_{1,2}^{n}) & -\mathfrak{Im}(z_{1,2}^{n}) & -1 \\ \vdots & \vdots & \vdots & \vdots & \vdots & \vdots \\ \mathfrak{Re}(z_{8n-1,2}^{-n}) & -\mathfrak{Im}(z_{8n-1,2}^{-n}) & \dots & \mathfrak{Re}(z_{8n-1,2}^{n}) & -\mathfrak{Im}(z_{8n-1,2}^{n}) & -1 \end{bmatrix}, \mathbf{x} = \begin{bmatrix} a_{-n} \\ b_{-n} \\ a_{-n+1} \\ b_{-n+1} \\ \vdots \\ a_{n-1} \\ b_{n-1} \\ a_n \\ b_n \\ \log \rho \end{bmatrix},$$

$$\text{and } \mathbf{C} = \begin{bmatrix} -\log|z_{0,1}| \\ -\log|z_{1,1}| \\ \vdots \\ -\log|z_{8n-1,1}| \\ -\log|z_{0,2}| \\ -\log|z_{1,2}| \\ \vdots \\ -\log|z_{8n-1,2}| \end{bmatrix}.$$

Solving the least squares problem in Eq. (3.17), we get the coefficients as well as the conformal modulus. From the least squares solution, we can construct $u(z)$ and $v(z)$ to get the conformal map $f(z)$ according to Eq. (3.7). We implement the conformal map numerically using the open source package `chebfun` (`https://www.chebfun.org/`, `http://www.chebfun.org/examples/`) and `conformal2` (`http://www.chebfun.org/examples/complex/ConformalMapping2.html`). The Fourier series approximations of Jordan boundaries P_1 and P_2 take the parametric forms $r_1(\theta)$ and $r_2(\theta)$, respectively. Multiplying the parametric forms by $e^{i\theta}$ gives us the sampled points on the Jordan boundaries in the forms $r_1(\theta)\cos(\theta) + ir_1(\theta)\sin(\theta)$ for P_1 and $r_2(\theta)\cos(\theta) + ir_2(\theta)\sin(\theta)$ for P_2. The function `chebfun` samples $8n$ points from each of $r_1(\theta)e^{i\theta}$ and $r_2(\theta)e^{i\theta}$ to set up the least squares problem in Eq. (3.17). The function `conformal2` solves the least squares problem to find the series approximation of $f(z)$, and then the AAA algorithm takes the series expansion form of $f(z)$ and converts it to a barycentric rational approximation [51]. The reason for using the AAA algorithm is that the rational approximation uses a smaller number of coefficients than a polynomial representation of $f(z)$ [51].

The AAA algorithm samples m, with $m \leq 16n$, distinct points, also known as support points, from the Jordan boundaries of the physical cross section. Let's call these points $z_1, z_2, \ldots, z_m$. These points are then mapped to their corresponding images, $f_1 = f(z_1), f_2 = f(z_2), \ldots, f_m = f(z_m)$, on the boundaries of the reference annulus using the forward map $f(z)$ in Eq. (3.7), using a set of non-zero complex weights $w_1, w_2, \ldots, w_m$. The function `conformal2` returns a function handle `f`, with the values of z_j, f_j and w_j, for $j = 1, 2, 3, \ldots, m$. Then, the barycentric rational representation of $f(z)$ takes the form

$$f(z) = \sum_{j=1}^{m} \frac{w_j f_j}{z - z_j} \Bigg/ \sum_{j=1}^{m} \frac{w_j}{z - z_j} \tag{3.18}$$

(see Theorem 2.1 [51]). According to [51], for reasonable choice of z_j, the construction of the barycentric rational approximation becomes well conditioned. This improves the numerical stability of the conformal map. It should be noted that the AAA algorithm uses the Arnoldi factorization of $\mathbf{A}$ in Eq. (3.17), representing Eq. (3.13) through an orthogonal polynomial basis rather than monomials.

For the inverse conformal map g, the AAA algorithm samples k distinct points, $Z_1, Z_2, \ldots, Z_k$, from the boundaries of the reference annulus, with $k \leq 16n$. The corresponding points $F_j \equiv z_j$ on the Jordan boundaries of the physical cross section are known, satisfying $g(Z_j) = F_j$ for $j = 1, 2, \ldots, k$, using a set of non-zero complex weights $W_1, W_2, \ldots, W_k$. The code `conformal2` returns another function handle for the inverse conformal map $g(z)$, written as `finv` in the codes in the GitHub link (provided towards the end of this thesis), containing the values of Z_j, F_j and W_j for $j = 1, 2, 3, \ldots, k$, from which the barycentric rational approximation of the inverse conformal map can be constructed in the form $g(z) = N(z)/D(z)$. Then, the derivative of $g(z)$ can be written as

$$g'(z) = \frac{N'(z)D(z) - N(z)D'(z)}{D(z)^2};\ N'(z) = -\sum_{j=1}^{k} \frac{W_j F_j}{(z - Z_j)^2},\ D'(z) = -\sum_{j=1}^{k} \frac{W_j}{(z - Z_j)^2}. \tag{3.19}$$

Then, the unit fiber vector in the physical cross section can be found using Eq. (3.5). The code `conformal2` also returns the value of the conformal modulus ρ.

3.4 Results

Given a general arterial cross section, we find the forward and the inverse conformal map through barycentric rational approximation of f and g. Thus, for each of the layers, we find the fiber field on the corresponding reference annulus and map the fiber field back to the physical cross sections by applying Eqs (3.5) and (3.6). Following the mapping procedure as shown in Fig. 3.2, the resulting fiber fields are computed in Fig. 3.3.

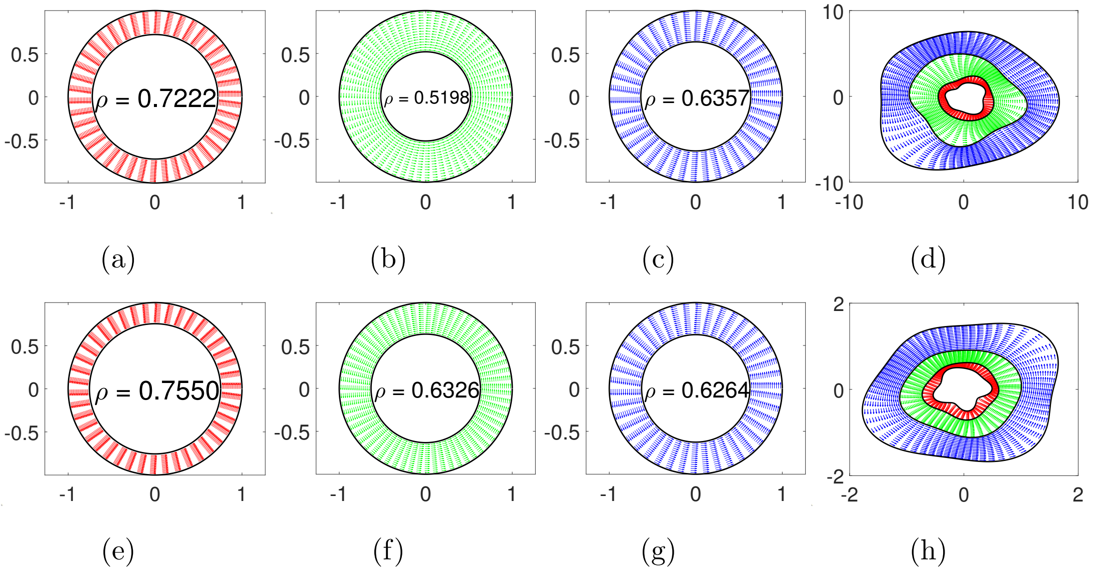

(a) (b) (c) (d)

(e) (f) (g) (h)

Figure 3.3: Conformal mapping of fiber fields between the reference annulus and the physical cross section for each of the three layers of an artery. Here we show mappings for two different cross sectional geometries. ρ is the conformal modulus. The values of m for the conformal map for the intima in (d) to (a), media in (d) to (b), and adventitia in (d) to (c) are 29, 30, and 26, respectively. The values of m for the conformal map for the intima in (h) to (e), media in (h) to (f), and adventitia in (h) to (g) are 34, 24, and 25, respectively.

Fig. 3.3 (a)–(c) represents the fiber field in the reference annulus for each of the three layers. (a) represents the reference annulus for the intima of the physical cross section in (d). Similarly, (b) and (c) represent the reference annuli for the media and the adventitia, respectively, corresponding to the physical cross sections in (d). (e)–(h) represent the reference annuli for the intima, media and adventitia and the physical cross section, respectively, for a different physical cross section geometry. The conformal modulus ρ is different for each of the reference annuli. A 3D visualization of the fibers is shown in Fig. 3.4.

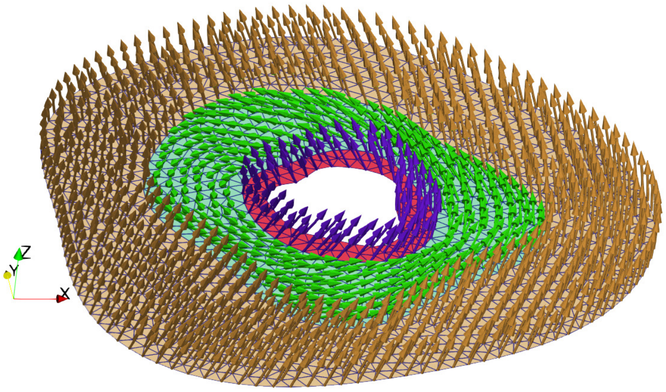

Figure 3.4: 3D view of the fiber fields for the three layers. Region colored red is the intima, region colored green is the media, and the region colored brown is the adventitia. The angles of inclination with respect to the plane for the intima, media and the adventitia are 60.3°, 20.61° and 67°, respectively. On the media-adventitia interface, we define the inclination angle to be 67°, and on the intima-media interface, we define the inclination angle to be 60.3°.

We also applied our technique to Fig. 2(a) of [48], which is a cross section of an adult right coronary artery, and generated the fiber fields in each of the three layers.

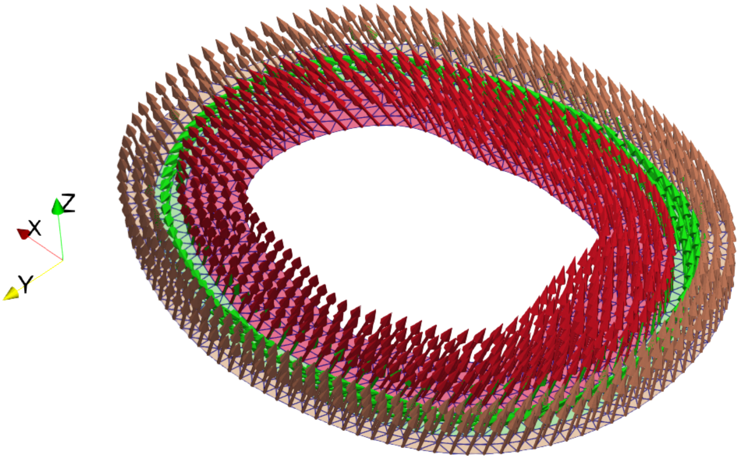

Figure 3.5: Fiber fields generated by the method of conformal maps for the cross section in Fig. 2(a) of [48].

The computation of fiber fields is of utmost importance in an accurate model for arterial mechanics. We have shown that, by using conformal maps, we can achieve that goal efficiently. To calculate the fiber fields using conformal maps, we only need a representation of the Jordan boundaries of the three layers. Provided with the Fourier series, the MATLAB function `conformal2` then calculates the conformal modulus ρ, the forward function handle `f` and the inverse function handle `finv`, which are necessary to create the barycentric rational approximations of the forward and the inverse maps. Using the barycentric rational approximations, we then create the fiber fields for each of the layers in the physical cross section.

However, there are limitations in using the method of conformal maps. Our model does not take into account fiber dispersion as probabilistic approaches do. However, that can be readily fixed by introducing appropriate distribution functions to the fiber orientation in the reference or the physical cross section. Another limitation is that the code `conformal2` diverges for Jordan boundaries that have points with large second derivatives (i.e., where the curvature is very high). This commonly results in the *crowding phenomenon* [77] (see the GitHub link at the end of the thesis for an example).

As discussed in the Introduction, collagen fibers in the myocardium or an artery are mainly oriented in a "circumferential direction"; however, the notion of a circumferential direction is not well defined in the case of a general cross section geometry. The term only makes sense in the case of an annular cross section. Conformal maps make the concept of a "circumferential direction" mathematically precise. We say that a fiber vector is oriented in a circumferential direction in a general cross section if and only if the fiber when mapped to the reference annulus using the forward conformal map is the angular unit vector.

Our method works for any general cross section geometry (except for the one limitation mentioned above). Given a cross section geometry, once the map is constructed, the fiber directions can be found out readily. The lengths of the fibers projected onto the physical cross section depend on the angles of inclination. This results in fibers of different projected lengths in different layers. Also, computational techniques for explicitly finding the fiber field for general cross section geometries using non-probabilistic approaches are rarely documented. Our paper [47] fills the gap and provides an example of an important biomechanical application of conformal mapping.

This chapter is taken from [47] (see Appendix A for rights).

Chapter 4

NUMERICAL METHODS

For numerical simulations, we have considered three geometries to work on which are presented in the next chapter. We should note that these geometries do not correspond to any specific medical images. For generating the geometries and the meshes, we have used an open source software called `Gmsh` and for solving the hyperelasticity problems using finite elements, we have used `FEniCS`, which is an open source software based on Python. For calculating the conformal maps for generating the fiber fields in the reference configuration, we have used `MATLAB`.

In order to create a 2D geometry and a mesh in `Gmsh`, we need to provide the software with a set of boundary points. So we created the desired geometry using `Inkscape` and sampled points from the boundaries using `WebPlotDigitizer` (`https://automeris.io/WebPlotDigitizer/`). Once the points on the boundaries are supplied to `Gmsh`, we can create surfaces in between the boundaries. Finally, we create a mesh on the domains.

We then create the conformal mapping in `MATLAB`. In order to create the conformal mapping, we need to provide a Fourier series for each of the boundaries. We then find the fiber fields for each of the three layers.

In `FEniCS`, we solve the hyperelasticity problem in two steps using first order elements on a very fine mesh. The minimization of the total energy is done using Newton iteration. We have divided the problem into two steps.

The first step includes pressurizing the domain without any growth, which we call the pressure loop. In this step, we slowly increase P from 0 kPa to 13 kPa using small pressure increment. The growth tensor is the identity for every layer. For each increment, we set the initial condition to be the solution from the previous step. Finally, we get the solutions $\mathbf{u}_{1,p}$ and $\mathbf{u}_{2,p}$ to be optimal displacement fields for the arterial layer and the lumen, respectively, at 13 kPa with no growth.

Next, is the growth loop. We discretize time T into small time increments. We set the final solutions from the pressure loop, $\mathbf{u}_{1,p}$ and $\mathbf{u}_{2,p}$ as initial conditions for the first iteration. For subsequent iterations, we set the initial condition to be the solution from the previous time step.

We implement other numerical techniques in our model such as meshing the lumen, regularization of curvature, and formulating all problems in their weak form. These methods are discussed below.

4.1 Meshing the lumen

In our model, the shape of the arterial lumen evolves over time as the arterial wall grows and deforms. Therefore, in order to solve for the Poiseuille flow through the lumen as time progresses, we need a mesh on the lumen. As the lumen shape changes, the mesh must also deform. To calculate the displacement of the nodes in the lumen mesh, we minimize the energy functional

$$\Pi(\mathbf{u}_l) = \int_{\Omega_0} W_0(\mathbf{F}_e^{(0)})\, dA \tag{4.1}$$

where $\mathbf{u}_l$ which represents the displacement field of the nodes of the mesh and the energy density function for the lumen is defined as follows [58]:

$$W_0 = \underbrace{\frac{\mu_0}{2}(I_1^{(0)} - 3)}_{\text{Neo-Hookean term}} + \underbrace{\left(\frac{\kappa}{2} - \frac{\mu_0}{3}\right)(J_e^{(0)} - 1)^2}_{\text{Penalty term}} - \underbrace{\mu_0 \ln J_e^{(0)}}_{\text{Auxiliary term}} . \tag{4.2}$$

In the above equation, the superscripts and the subscripts 0 signify that we are dealing with the lumen.

Since there is no growth tensor associated with the lumen, we consider $\mathbf{F}_g^{(0)} = \mathbf{I}$.

$$\mathbf{F}^{(0)} = \mathbf{F}_e^{(0)} \tag{4.3}$$

$$I_1^{(0)} = \mathrm{Tr}(\mathbf{F}_e^{(0)T}\mathbf{F}_e^{(0)}) \tag{4.4}$$

$$J_e^{(0)} = \det(\mathbf{F}_e^{(0)}) \tag{4.5}$$

and

$$\mathbf{F}^{(0)} = \mathbf{F}_e^{(0)} = \mathbf{I} + \nabla \mathbf{u}_l. \tag{4.6}$$

Since the endothelium is a boundary to the lumen, the optimal solution $\mathbf{u}_l$ is defined at the endothelium too. The endothelium is a common boundary to the lumen and the arterial wall which has the displacement field $\mathbf{u}$. Thus, the displacement field must be continuous across $\partial\omega_1^{(1)}$:

$$\mathbf{u}_l(x, y) = \mathbf{u}(x, y), \quad (x, y) \in \partial\omega_1^{(1)}. \tag{4.7}$$

There are several ways to mesh the lumen. One of them is to re-mesh the lumen at every time step using `gmsh`. However, that may create an issue in node mismatch along the endothelium. After re-meshing using `gmsh`, the nodes of the re-meshed lumen don't always match with the nodes of mesh on the arterial wall at the endothelium. Since the displacement field of the adjacent mesh must match the displacement field of the re-meshed lumen, mismatch in node alignments forbids us from enforcing the Dirichlet boundary condition (4.7) on the endothelium. Therefore, we opted for another way of evolving the mesh of the lumen as the three layers of the artery deform using a strain energy density function on the initial lumen mesh mimicking an imaginary highly compressible material. We introduced the strain energy density function (4.2) on the lumen mesh to deform the mesh in a way such that the mesh elements stay regular (don't become too skewed). Triangular elements that are close to equilateral stabilize the numerical solution of the Poiseuille flow. The edges of the elements of the mesh can be imagined as elastic springs connecting the nodes of the mesh. As the lumen deforms, the springs configure themselves in a way to minimize the total energy stored in them, resulting in more regular elements. So, we have taken $\mu_0 = 1$ and $\kappa = \frac{2}{3}$ in Eq. (4.2) to make the penalty term vanish, resulting in filling the lumen with an artificial, compressible material.

4.2 Regularization of curvature

If the endothelium is parameterized in terms of $r(\theta)$, then we calculate the curvature as $\frac{r^2 - rr'' + 2r'^2}{(r'^2 + r^2)^{\frac{3}{2}}}$. In this section, we calculate $r(\theta)$ from the center $(0, 0)$. Although most interesting relations between $r(\theta)$, $\tau(\theta)$, $C(\theta)$, and $\kappa(\theta)$ are observed when we calculate these quantities with respect to the center of flow, we chose the center of flow to be at $(0, 0)$ only for this section to demonstrate the effectiveness of regularization before differentiation. It is a well known fact that given a noisy function $r(\theta)$, taking a numerical gradient amplifies the noise. Any numerical method will introduce errors in the node positions, resulting in a noisy $r(\theta)$. This can be seen from Fig. (4.1) below. Although the endothelium in mesh 1 is a perfect circle, the plot of $r(\theta)$ is not a constant. Instead, there is some noise in the data. If we calculate the curvature using the $r(\theta)$ as shown in the plots, the noise in the data amplifies and as a result, the curvature becomes very noisy. Therefore, one needs to regularize the curvature or in other words, make it smooth.

There are several different ways to smoothly differentiate noisy data [35]. One way is to first fit a smoothing spline (`https://csaps.readthedocs.io/en/latest/formulation.html#implementation`) through the noisy data set of $r(\theta)$. Then we sample data points from the spline itself and then differentiate to find the curvature. A smoothing spline $f(x)$ is a real-valued function that minimizes

$$\alpha \sum_{j=1}^{n} |y_j - f(x_j)|^2 + (1 - \alpha) \int_a^b [f''(t)]^2 \, dt \tag{4.8}$$

where y_j are the given data points, $a = \min(x_1, x_2, \ldots, x_N)$, $b = \max(x_1, x_2, \ldots, x_N)$ and $\alpha \in [0, 1]$ is the smoothing parameter. If $\alpha \to 0$, then the smoothing spline $f(x)$ is the least squares straight line fit to the data. On the other hand, if $\alpha \to 1$, then $f(x)$ is the natural cubic spline interpolant.

The value of the smoothing parameter should depend on the magnitude of noise present in the data. We experimented with different values of α for different geometries. For cross section 1, we considered $\alpha = 0.1$, while for cross sections 2 and 3, we chose $\alpha = 0.992$.

In the below figure, we demonstrate how noisy the curvature can be when we don't fit $r(\theta)$ with a smoothing spline. The graph for $r(\theta)$ is the distance to the endothelium at time $t = 0$.

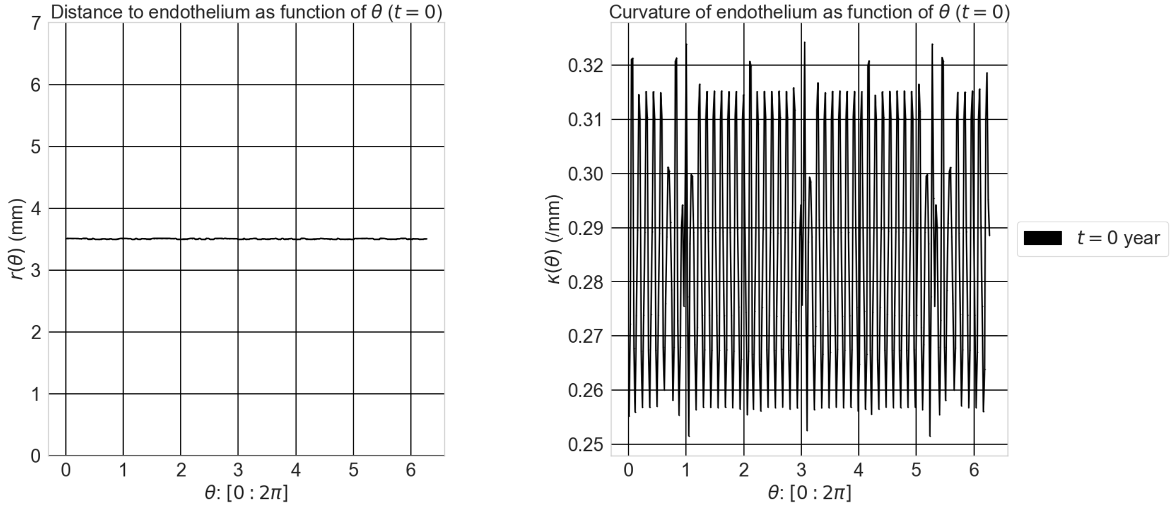

Figure 4.1: Noisy curvature obtained before fitting a smoothing spline through $r(\theta)$.

Next, we fit a smoothing spline through $r(\theta)$ and differentiate the spline itself instead of the actual $r(\theta)$. The smoothing spline has the smoothing coefficient $\alpha = 0.1$.

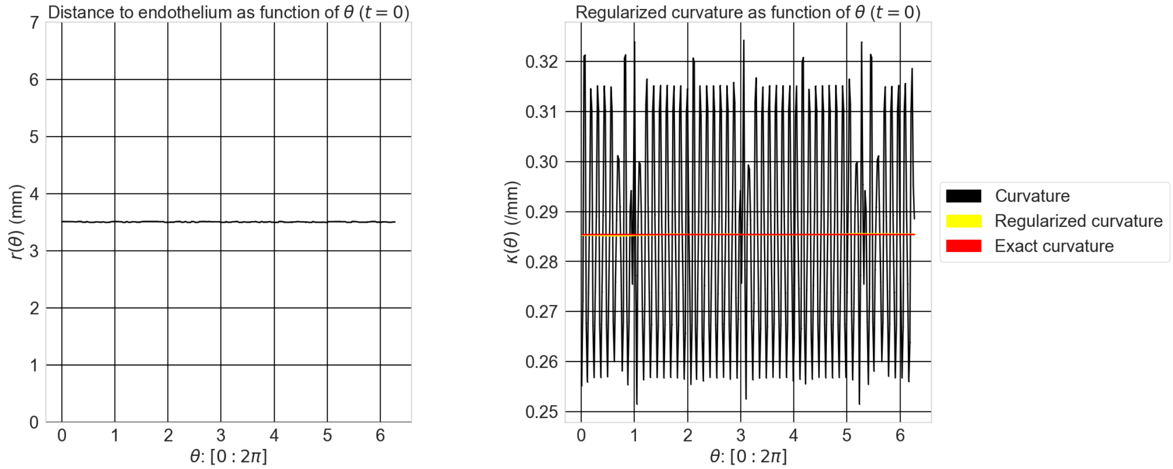

Figure 4.2: Regularized curvature of the endothelium. The exact curvature is calculated as $\dfrac{1}{\sqrt{\text{lumen area}/\pi}}$. The mean square error (MSE) between the regularized curvature and the exact curvature is $\approx 1.14 \times 10^{-8}$.

In Figs. (4.1) and (4.2), we are measuring the distance to the endothelium (the radius) of the lumen from the center $(0, 0)$. We observe from Figs. (4.1) and (4.2) that the magnitude of the noise decreases after we regularize the curvature by fitting a spline through $r(\theta)$ before differentiating it numerically. in Fig. (4.2), we calculate the radius of the lumen at $t = 0$ and $P = 13$ kPa as $\sqrt{\text{lumen area}/\pi}$. We observe that the regularized curvature is approximately the same as the exact curvature.

The error between the regularized and the exact curvature is shown in Fig. 4.3 below

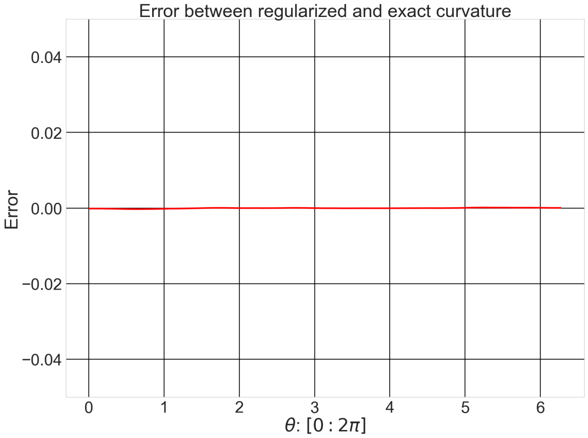

Figure 4.3: Error between the exact and the regularized curvature. The minimum error and the maximum error are -0.00027 and 0.00014, respectively.

4.3 Weak forms

A given PDE involves differentiation with respect to the independent variables. In most real-world problems, this results in PDEs that are hard to solve numerically. A finite element method is a discretization in space and time, which turns the PDE into a set of equations defined on only the nodes of the mesh. We multiply the PDE by a test function. Then integration by parts and introduction of a nodal basis convert the PDE into a set of algebraic equations on the nodes of the mesh. We solve these algebraic equations to get an approximate solution of the PDE over the mesh. In our work, we have three PDEs to solve: one for the Poiseuille flow through the lumen, one for the diffusion–degradation equation for PDGF distribution, and another for the stress distribution for the arterial wall when it is in mechanical equilibrium.

4.3.1 Weak form for the Poiseuille flow

Multiplying the Poisson equation with a test function $v \in C^1(\bar{\omega}_0)$, such that $v = 0$ on boundaries, we get

$$v\Delta w = -\frac{G}{\mu_l}v \tag{4.9}$$

Integrating Eq. (4.9) by parts over the domain ω_0,

$$\int_{\partial\omega_1^{(1)}} v\nabla w \cdot \mathbf{n}\, ds - \int_{\omega_0} \nabla v \cdot \nabla w \, dA = -\frac{G}{\mu_l}\int_{\omega_0} v\, dA \tag{4.10}$$

The boundary term $\int_{\partial\omega_1^{(1)}} v\nabla w\cdot\mathbf{n}\, ds$ vanishes on $\partial\omega_1^{(1)}$ [39]. Then, the above variational form becomes

$$\int_{\omega_0} \nabla v \cdot \nabla w \, dA - \frac{G}{\mu_l}\int_{\omega_0} v\, dA = 0 \tag{4.11}$$

Therefore, we need to find $w(x, y)$ that satisfies Eq. (4.11) for all test functions $v \in C^1(\bar{\omega})$.

4.3.2 The weak form of the diffusion-degradation equation

Consider a test function $v \in C^1(\bar{\omega})$ such that $v = 0$ on $\partial\omega_3^{(2)}$. Multiplying both sides of the diffusion-degradation equation (2.19) with the test function v, we get,

$$vD\Delta C - kCv = 0. \tag{4.12}$$

Integrating both sides over the domain ω,

$$\int_{\omega} v\Delta C\, dA = \int_{\omega} \frac{k}{D} Cv\, dA. \tag{4.13}$$

Integrating by parts, we get,

$$\int_{\partial\omega_1^{(1)}\cup\partial\omega_3^{(2)}} v\, \nabla C \cdot \mathbf{n}\, ds - \int_{\omega} \nabla v \cdot \nabla C\, dA = \int_{\omega} \frac{k}{D} Cv\, dA \tag{4.14}$$

$$\int_{\partial\omega_1^{(1)}} v\, \nabla C \cdot \mathbf{n_1}\, ds_1 + \int_{\partial\omega_3^{(2)}} v\, \nabla C \cdot \mathbf{n_4}\, ds_4 - \int_{\omega} \nabla v \cdot \nabla C\, dA = \int_{\omega} \frac{k}{D} Cv\, dA \tag{4.15}$$

where $\mathbf{n_1}$, ds_1, $\mathbf{n_4}$, ds_4 are unit normals and line elements to $\partial\omega_1^{(1)}$ and $\partial\omega_3^{(2)}$, respectively.

Let $\Gamma = -\frac{J_{\max}}{D}\frac{\tau}{\tau + \tau_0}$. Then from the boundary conditions of the diffusion-degradation equation,

$$\int_{\partial\omega_1^{(1)}} v\, \Gamma ds - \int_{\omega} \nabla v \cdot \nabla C\, dA = \int_{\omega} \frac{k}{D} Cv\, dA. \tag{4.16}$$

Since C = 0 on $\partial\omega_3^{(2)}$, we choose trial functions that vanish on $\partial\omega_3^{(2)}$. Therefore, the integral $\int_{\partial\omega_3^{(2)}} v\,\nabla C\cdot\mathbf{n_4}\,ds_4$ vanishes.
Rearranging the above equation, we get the the weak form as

$$\int_\omega \nabla v\cdot\nabla C\,dA + \int_\omega \frac{k}{D}Cv\,dA = v\int_{\partial\omega_1^{(1)}}\Gamma ds \tag{4.17}$$

Within an FEM framework, we solve for $C(x,y)$ that satisfies Eq. (4.17) for all test functions v. The solution $C(x,y)$ gives the PDGF concentration at each point (x,y) in the vessel layers.

4.3.3 Weak form of the mechanical equilibrium equation

We multiply both sides of the mechanical equilibrium equation by a test function $v\in C^1(\bar\omega)$, where $\omega=\omega_1\cup\omega_2\cup\omega_3$ to get

$$v\nabla\cdot\boldsymbol{\sigma}=0. \tag{4.18}$$

Using vector calculus identity

$$\nabla\cdot(\boldsymbol{\sigma}v)=(\nabla\cdot\boldsymbol{\sigma})v+\boldsymbol{\sigma}:\nabla v, \tag{4.19}$$

the equilibrium equation becomes

$$\nabla\cdot(\boldsymbol{\sigma}v)-\boldsymbol{\sigma}:\nabla v=0. \tag{4.20}$$

Integrating both sides with respect to the domain ω and using the divergence theorem we get,

$$\int_\omega \nabla\cdot(\boldsymbol{\sigma}v)\,dA-\int_\omega \boldsymbol{\sigma}:\nabla v\,dA=0, \tag{4.21}$$

$$\int_\omega \boldsymbol{\sigma}:\nabla v\,dA=\int_{\partial\omega}(\boldsymbol{\sigma}\cdot\mathbf{n})v\,ds. \tag{4.22}$$

Since $\boldsymbol{\sigma}\cdot\mathbf{n}=-p\mathbf{n}$ for $(x,y)\in\partial\omega_1^{(1)}$ and $\boldsymbol{\sigma}\cdot\mathbf{n}=0$ for $(x,y)\in\partial\omega_3^{(2)}$, the above integral equation reduces to

$$\int_\omega \boldsymbol{\sigma}:\nabla v\,dA=-p\int_{\partial\omega_1^{(1)}} v\,\mathbf{n}\,ds. \tag{4.23}$$

Eq. (4.23) above can be rewritten as [11]

$$\Pi'[\mathbf{\Phi}]\mathbf{\Phi}' = \int_{\omega} \boldsymbol{\sigma} : \nabla v \, dA + p \int_{\partial \omega_1^{(1)}} v \, \mathbf{n} \, ds = 0. \tag{4.24}$$

We solve Eq. (4.24) for test functions $\mathbf{\Phi}'$. We should note that the solution $\mathbf{\Phi}$ of Eq. (4.24) that minimizes the total stored energy $\Pi[\mathbf{\Phi}]$ may not be unique. One reason for the existence of multiple minimizers of $\Pi[\mathbf{\Phi}]$ is that it may be polyconvex [11], implying the possible existence of multiple local minima.

Chapter 5

RESULTS AND SIMULATION

In this section, we present the results of the numerical simulations. As mentioned in the previous section, we simulate for three different vessel cross section geometries. We should once again note that the cross section geometries do not correspond to any medical imaging data. We created the geometries using an open source software `Gmsh`, we simulated the fiber fields and the results of Chapter 3 with the help of `Matlab`, and used another open source software `FEniCS` to execute the codes.

5.1 A general overview of the results

We simulate intimal growth subject to hemodynamic shear stresses in cases of three separate cross sections to illustrate the relationship between intimal growth and the features of hemodynamics.

We have considered a constant pressure of 13 kPa, which corresponds to ≈ 100 mmHg (the mean arterial blood pressure in a healthy individual with 120 mmHg systolic and 80 mmHg diastolic pressure) on the endothelium, and have simulated our results for 2 years. We show that the initial geometry of cross sections is one of the important features that dictates the subsequent evolution of the shape of the thickened intima and most importantly, the rate of lumen occlusion. To illustrate the interesting role of geometry, we have considered an annular cross section that is axisymmetric and two other cross sections that are not axisymmetric. The cross sections are shown in Fig. 5.1 below.

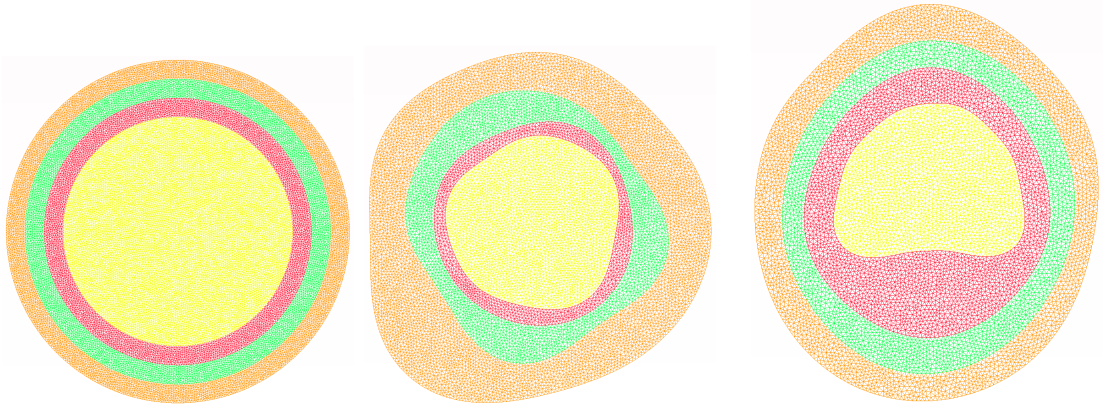
(a) Cross section 1 (b) Cross section 2 (c) Cross section 3

Figure 5.1: (a) Annular cross section with the lumen radius being 3 mm and the thickness of each of the layers being 0.5 mm. (b) General cross section. (c) Atherosclerotic cross section with a half filled lumen. Region colored yellow corresponds to the lumen, red corresponds to intima, green corresponds to media, and orange corresponds to the adventitia.

With intimas that are annular and have uniform thickness, the lumen gets occluded from all directions at the same rate. But with cross sections that are not annular and have a non-uniform intima thickness, the thicker parts of the intima occlude the lumen at a rate faster than the relatively thinner parts of the intima. In addition to the effect of cross section geometry, we show that the distance to the endothelium from the flow center (point in the lumen where the magnitude of the Poiseuille flow is maximum) is a strong predictor of PDGF concentration and shear stress. Another interesting feature that results from non-annular cross sections is the evolution of the shape of the lumen. With time, the shape of the lumen tends to become polygonal and the maximum curvature of the endothelium increases with time. One other important feature is the role of PDGF in controlling the growth of the intima. Since the growth tensor incorporates PDGF, one might be led to believe that higher PDGF concentrations in some parts of the intima causes that corresponding part to grow faster compared to parts where the concentration of PDGF is lower. However, we show that this might not always be true and we demonstrate that for cross section 3.

The properties of the meshes for each of the geometries in Fig. 5.1 are as follows:

Geometries	Layers	Number of elements	Number of nodes	Area (mm^2)
Cross section 1	Intima	6807	3725	10.21
	Media	8007	4374	11.78
	Adventitia	9320	5080	13.35
	Lumen	18565	9432	28.27
	Total	33307	22611	63.61
Cross section 2	Intima	2010	1188	23.82
	Media	4547	2491	57.39
	Adventitia	9854	5205	130.24
	Lumen	5889	3030	70.33
	Total	22300	11914	281.78
Cross section 3	Intima	4008	2168	33.87
	Media	3477	1950	30.58
	Adventitia	4662	2585	39.28
	Lumen	3599	1869	30.15
	Total	15746	8572	133.88

Table 5.1: Properties of the meshes introduced on the three different geometries.

From Fig. 5.1 above, we see that cross section 1 has a uniformly thick intima to begin with whereas cross sections 2 and 3 have intimas of varying thickness in the reference stress free configuration.

5.2 The pressure loop and the growth loop

The dynamics of the arterial cross sections is governed by two factors: the pressure on the endothelium and the growth tensor. In our model, we are applying a constant pressure of 13 kPa on the endothelium as the vessel deforms under growth. Under this constant load, the vessel deforms, and we aim to find an optimal displacement field that results in a final configuration that has minimum energy.

Since the minimization scheme relies on Newton's method, we cannot achieve convergence if our initial guess of the displacement field is not close enough to the actual solution. If we start with a pressure of 13 kPa on the endothelium, the final displacement field will be far off from $\mathbf{u} = (0, 0, 0)^T$, which is our initial guess. So we need to ramp up the pressure slowly using a `for` loop. We call this the *`pressure loop`*. We start with a reference stress free configuration and slowly increase the pressure to 13 kPa without any growth (all growth tensors are identities). We save the final solution of the pressure loop and pass it as an initial guess to the *`growth loop`*.

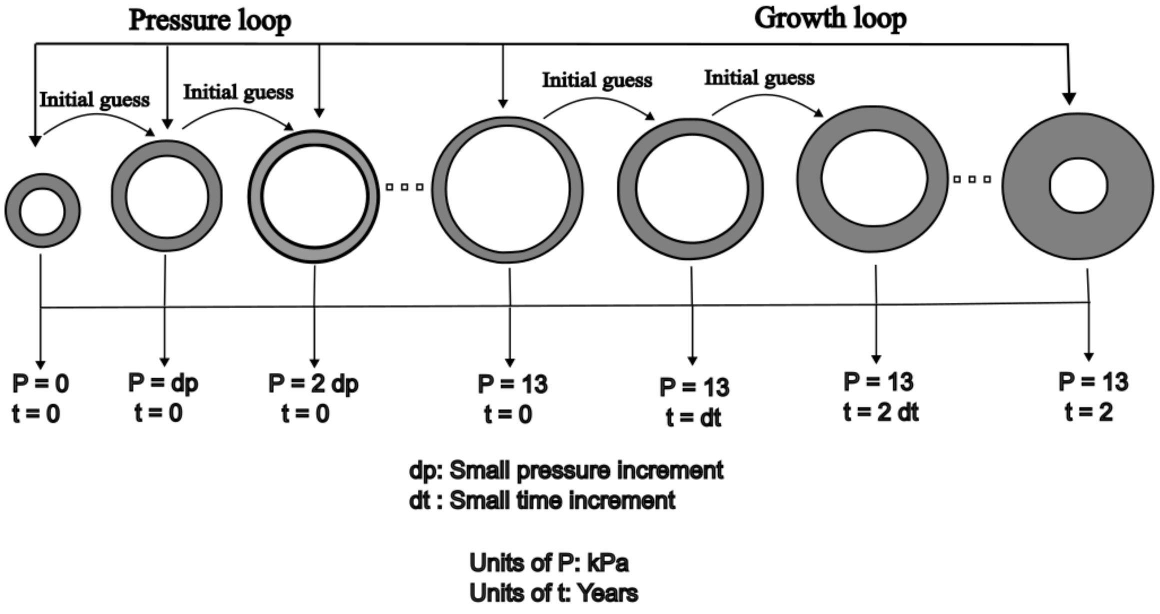

Figure 5.2: Schematic diagram of the algorithm. The pressure loop slowly increases the pressure from 0 to 13 kPa with no growth. The final solution of the pressure loop is passed as an initial guess to the growth loop.

Fig. 5.2 above represents a schematic diagram that illustrates the algorithm. In the figure, we start with the reference stress free configuration ($P = 0$, $t = 0$) and an initial guess $\mathbf{u} = (0, 0, 0)^T$ for the displacement field. For the next iteration, we increase the pressure by an amount dp and pass $\mathbf{u} = (0, 0, 0)^T$ as an initial guess. Thus, we slowly increase the pressure to 13 kPa, and for each iteration of the ***pressure loop***, we consider the solution of the previous iteration as an initial guess. For the pressure loop, there is no time increment, i.e., $t = 0$ for all iterations and the growth tensor for the intima is identity. Once we reach 13 kPa, we then consider the PDGF time-dependent growth tensor for the intima. Following a similar technique as implemented in the pressure loop, we slowly increment t by an amount dt, starting the growth loop from $t = 0$, applying a constant pressure of 13 kPa on the deforming endothelium. From the figure above, we note that in the pressure loop, the arterial wall experiences a dilation (an outward remodeling), while for the growth loop, the arterial wall thickens (due to thickening of the intima) because of the growth tensor. As a result, the arterial wall starts to dilate inward (inward remodeling), gradually occluding the lumen.

In the growth loop, we are applying a pressure of 13 kPa on the endothelium and a time-dependent growth tensor (also incorporating the PDGF) for the intima. So at time $t = 0$ years, the configuration must match the final configuration of the pressure loop. As the endothelium deforms due to pressure, we calculate the Poiseuille flow, the shear stress, and the PDGF concentration across the arterial wall. The PDGF concentration is then plugged into the growth tensor for the intima and looped through time. This growth tensor controls the growth of the intima over time.

We should note here that the choice of the values for dp and dt should be made carefully as they are very sensitive to mesh refinements. For coarse meshes, the values can be high, while for a highly refined meshes, the values must be smaller. We decided on the values for dp and dt based on trial and error. Since the meshes we are considering for our simulations are highly refined, we started with some small values of dp and dt. Upon encountering divergence, we reduce their values until we achieve convergence.

From the schematic diagram above, one might assume that an arterial wall initially experiences an outward remodeling followed by a single continuous phase of inward remodeling. However, we observe that this might not always be the case. We demonstrate in later sections that there can be multiple outward and inward remodeling phases during the growth loop. To the best of our knowledge, we haven't haven't found any literature that provides evidence of multiple remodeling phases during the growth of the arterial wall. While the causes behind this multiple remodeling are unclear, we suspect that the multiple remodeling is an adaptive response to changes in wall shear stress and happens in order to regulate or normalize the shear stress on the endothelium. A detailed investigation of this phenomenon is beyond the scope of this thesis.

5.3 Code validation

An important aspect of our simulation is to check that the code is working correctly. This can be done in several ways. For example, solutions can be checked against analytic solutions when they exist, or against codes that simulate 1D versions of the model. One of the important parameters in our mathematical model is the Poisson ratio ν. For lower values of ν, the arterial wall behaves as a compressible material, while for higher values of $\nu \approx 0.5$, the arterial wall behaves as an incompressible material. Another factor that influences the mechanical response of the arterial wall due to pressure and growth is the presence of collagen fibers. In the presence of collagen fibers, the arterial wall is much stiffer, while it is more compliant in the absence of them.

We validated our 2D `FEniCS` code against `Matlab` codes for two separate cases: one for a 1D compressible model with $P = 1$ kPa, $\nu = 0.4$, a time-dependent growth tensor without any PDGF, and no collagen fibers; and another for a 1D incompressible model with $P = 13$ kPa, a PDGF-dependent growth tensor for the intima, and collagen fibers. Both the `Matlab` codes simulate an annular geometry. Therefore, we only validated our `FEniCS` code with the `Matlab` codes for cross section 1, which is annular and thus axisymmetric.

5.3.1 Validation with the 1D compressible model

The 1D compressible `Matlab` code [11] considers an infinitely long cylinder with the three arterial layers. The geometry is annular. In addition, the strain energy density functions do not have the exponential term and there are no collagen fibers in the model.

We consider a pressure of 1 kPa acting on the endothelium of cross section 1 in Fig. 5.1. We consider $\nu = 0.4$ and $\mu_1 = 27.9$ kPa, $\mu_2 = 1.27$ kPa, and $\mu_3 = 7.56$ kPa.

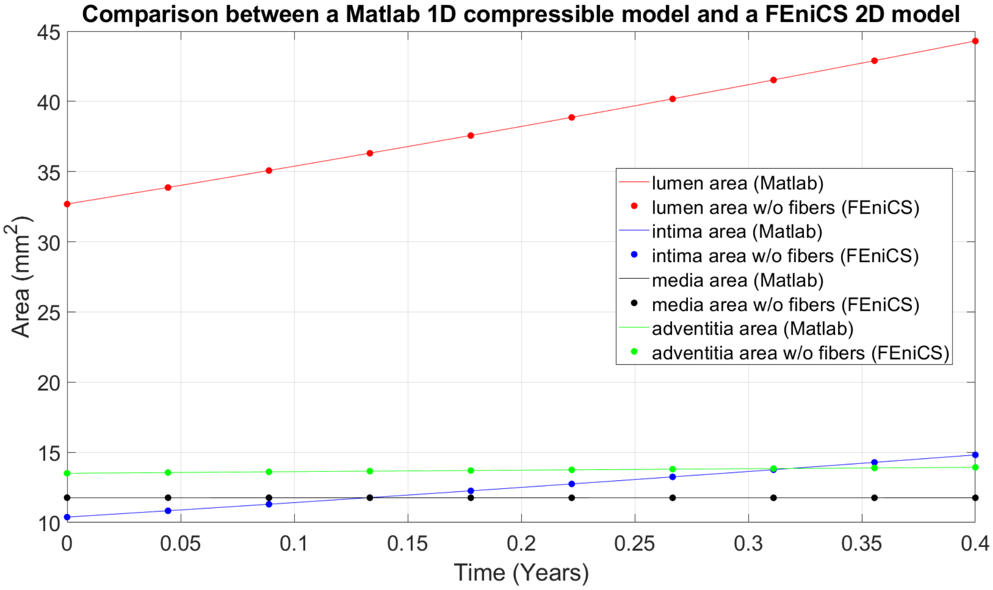

Figure 5.3: The `Matlab` and the `FEniCS` codes produce almost the same results with $\nu = 0.4$, $P = 1$ kPa, $\mu_1 = 27.9$ kPa, $\mu_2 = 1.27$ kPa, and $\mu_3 = 7.56$ kPa. There are no collagen fibers in any of the layers.

One of the reasons for choosing such a small value of the pressure is the absence of collagen fibers. When there are no collagen fibers, the arterial wall is very compliant to outward dilation. So for even a small pressure, we get a large deformation. Since the minimization follows the Newton's method, the difference between the initial guesses and the final solution for the displacement field is very large, resulting in divergence of the code. We considered the growth tensor for the intima to be $\mathbf{G_1} = \text{diag}(1 + t/2, 1 +$

$t/2, 1)$, where the values of t lies in the range $[0, 0.4]$. We observe from the plots below that the codes are in strong agreement with each other.

We should note once again that the above results reflect a compressible material since $\nu = 0.4$. In addition, the graphs above do not incorporate the effects of the collagen fibers or a PDGF-dependent growth tensor. All of the missing factors play a significant role in the full model.

5.3.2 Validation with 1D incompressible model

Although in the previous section, we validated the `FEniCS` code without collagen fibers, we need to validate it in the case with collagen fibers also. The second Matlab code we use for validation is an incompressible model that includes fibers and PDGF and so is closer to the full model. Because it is a fully incompressible model, to compare against it we take $\nu = 0.49$ or 0.499 in `FEniCS`.

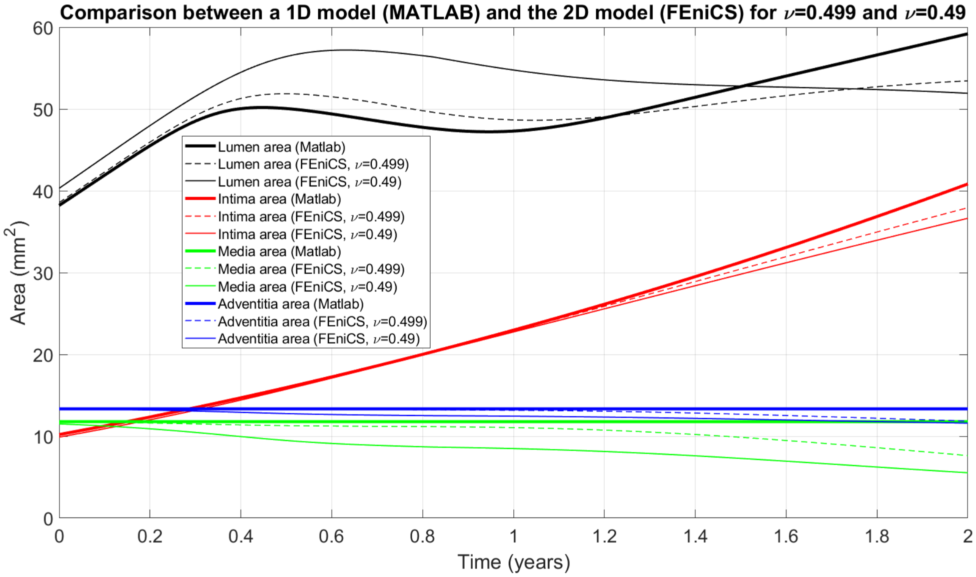

Figure 5.4: Comparison of areas between the `Matlab` 1D incompressible model and the 2D `FEniCS` compressible model.

The `Matlab` 1D incompressible code is different from the `FEniCS` code in some aspects. In the `Matlab` code, the strain energy density function doesn't have the penalty term (see Eq. (2.14)), implying a perfectly incompressible model. In addition, the shear stress and the PDGF concentration are derived from the exact 1D solution of the Poiseuille flow equation and the PDGF diffusion degradation equation, respectively. In `FEniCS`, all solutions are derived from finite element approximations. Since we are comparing our `FEniCS` code against a fully incompressible model, we take ν to be close to 0.5. So, we tested our `FEniCS` code against the `Matlab` code for $\nu = 0.49$ and $\nu = 0.499$. In Fig. 5.4, we show the effect of increasing ν from 0.49 to 0.499.

One of the important most important reasons to increase the Poisson ratio to be closer to 0.5 is to conserve the areas of individual layers as the vessel deforms under pressure and growth. When ν is away from 0.5, there is a significant loss in area, whereas when ν is close to 0.499, the accuracy improves. Although the accuracy improves as we increase ν, the loss of area also increases for sufficiently large time. So no matter how close ν is to 0.5, there will be significant loss in area as we increase time. This is a common phenomenon in finite element methods, and is commonly referred to as *volumetric locking*.

5.3.2.1 Volumetric locking

For incompressible materials, ν plays an important role in conserving area. Theoretically, $\nu \to 0.5$ results in a perfectly incompressible material. But with $\nu \approx 0.5$, locking increases and results in loss of accuracy in solutions, resulting in loss of volume [12]. In this article, Frâncu *et. al.* suggest ways to alleviate the effects of locking using various FEM strategies like for example, using discontinuous Galerkin methods or using higher-order elements. The authors mention that one has to consider fourth-order elements in order to reduce locking. But using such high order elements is computationally intensive and to implement a Galerkin method, one has to reformulate the weak form of the energy functional. The authors propose a mixed formulation method that minimizes the energy functional with respect to displacement $\mathbf{u}$ and a Lagrange multiplier p (discussed below in detail). In our model, in order to implement the mixed formulation, we need to minimize the energy functional with respect to $\mathbf{u}$ and the incompressibility factor ν. This method finds values of ν that are defined pointwise on the entire domain subject to the condition $J_e = 1$, thus enforcing incompressibility. In section 8.5 of [25], Holzapfel describes a two-field variational principle to get rid of the locking phenomenon. The author mentions that locking is a common FEM phenomenon observed when a single-field approach is used and results from over-stiffening of the system when low-order elements are used. The two-field variational principle replaces the coefficient of the penalty term, $\dfrac{\mu\nu}{1-2\nu}$, with a Lagrange multiplier p. So we solve for the displacement field $\mathbf{u}$ and p. In another article [30], Hung *et. al.* discuss the technique of smoothed finite element methods to alleviate locking. In this scheme, each cell is divided into sub-cells and the strain at a particular node is calculated as a weighted average of strains at neighboring nodes. But as the number of sub-cells increases, the error in the displacement field is reduced while the stress field loses accuracy. The authors show that expressing the volumetric part of the strain field using a single sub-cell is enough to alleviate locking.

In this work, we partly alleviated locking by mesh refinement and taking the Poisson ratio to be 0.499. However, in practice, one can take values even closer to 0.5. With sufficient mesh refinement and a value of Poisson ratio very close to 0.5, one can alleviate locking. One of the downside of mesh refinement and taking values of Poisson ratio very close to 0.5 is that it is computationally intensive. So we settled for a moderately refined mesh and a Poisson ratio close to 0.5 to increase time efficiency of the algorithm.

5.4 Solution of Poiseuille flow for three different cross sections

The shape of the lumen changes as the arterial wall undergoes deformation under pressure and growth. The shape of the lumen in turn affects the solution to the Poiseuille flow, thus affecting the shear stress and the flux of PDGF. As the shape of the lumen deforms with growth of the arterial wall, the location of the center of flow changes. The distance to the endothelium from the center of flow plays a major role in determining the shear stress and thus, the PDGF flux. We demonstrate the correlation among the distance of the endothelium from the center of flow, the shear stress, and PDGF concentration in Section 5.6. In this thesis, we have considered the pressure gradient $G = 0.013$ kPa/mm and the dynamic viscosity to be $\mu_l = 4 \times 10^{-6}$ kPa.s with a no-slip boundary condition at the endothelium.

5.4.1 Changes in lumen shape on Poiseuille flow

In this section, we simulate the Poiseuille flow through the lumen of the cross section geometries presented in Fig. 5.1. We demonstrate how the different geometries of the lumen affect the hemodynamics features such as the magnitude of flow, the changes in the center of the flow, and the evolution of the shape of the lumen as time increases.

We start with the annular case (cross section 1). The numerical solutions of the Poiseuille flow for different time points through the lumen of cross section 1 are shown in Fig. 5.5 below.

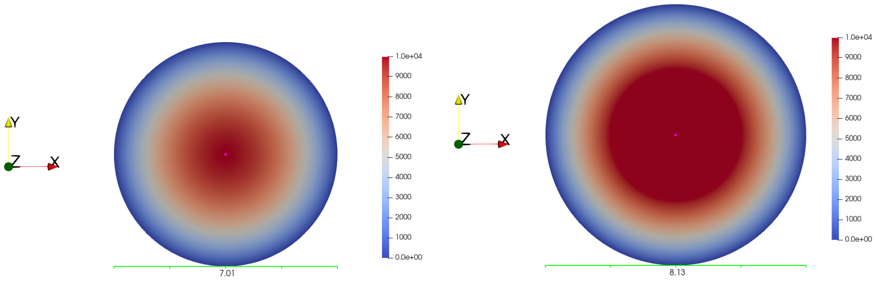

(a) $t = 0$ year.

(b) $t = 0.5$ years.

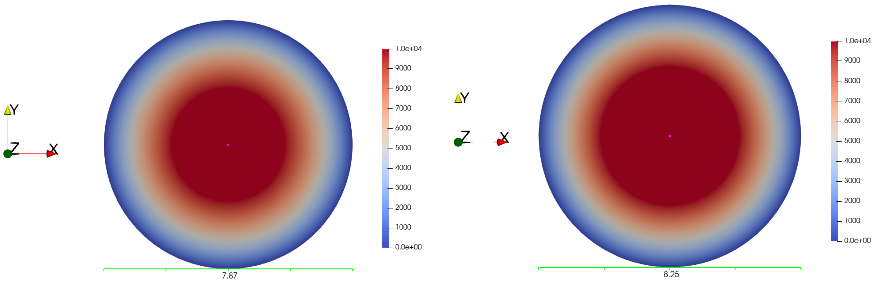

(c) $t = 1$ year.

(d) $t = 2$ years.

Figure 5.5: Numerical solution of Poiseuille flow through the lumen in a vessel pressurized with 13 kPa on the endothelium of geometry 1 for different time points. The green bar denotes the diameter of the lumen with units mm. The color bars represents the magnitude of the Poiseuille flow velocity (mm/sec). The pink dot represents the point (vertex) where the magnitude of velocity is maximum.

There are two important observations that we should note from the above figures. First, the diameter of the lumen follows some interesting dynamics with respect to time as the arterial wall grows. From $t = 0$ years to $t = 0.5$ years, the diameter of the lumen increases from 7.01 mm to 8.12 mm. But we notice a decrease in the diameter, 8.12 mm to 7.87 mm, as we move from $t = 0.5$ years to $t = 1$ year. The diameter again increases from 7.87 mm to 8.25 mm from $t = 1$ year to $t = 2$ years. So as the intima grows and the arterial wall deforms, the lumen first experiences an outward dilation, then an inward remodeling, followed by an outward dilation again. To the best of our knowledge, there does not exist any literature that supports this “multiple remodeling” and the reason for such dynamics is not clear and warrants further investigation. We believe that this dynamics of the lumen is an adaptive response to increase in shear stress. As the lumen begins to contract, the shear stress increases, enhancing the PDGF flux and reducing the contraction.

In Fig. 5.5, we observe that for an annular cross section geometry, the shape of the lumen stays as a circular disk as time evolves. For non-annular geometries, the shape of the lumen evolves to be polygonal with time. Next, we study the non-annular cross section 2 in Fig. 5.1b.

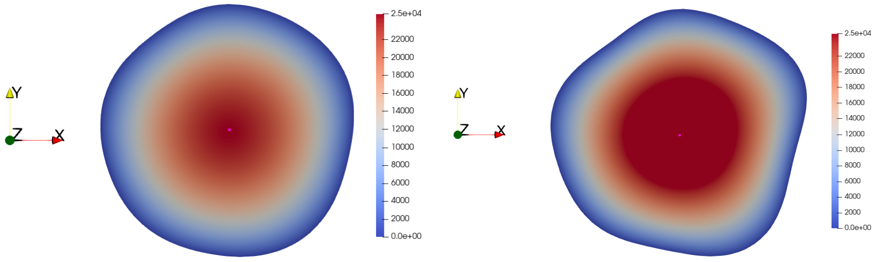

(a) $t = 0$ year. (b) $t = 1$ year.

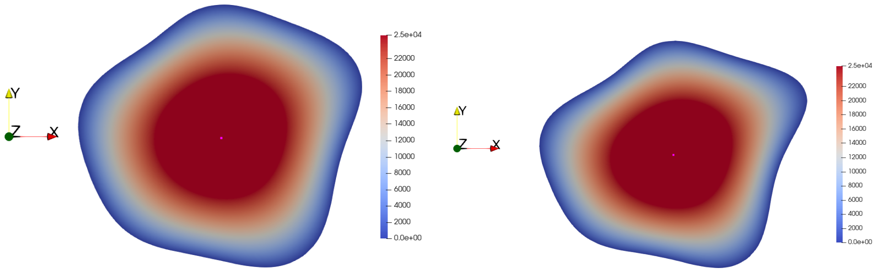

(c) $t = 1.5$ years. (d) $t = 2$ years.

Figure 5.6: Numerical solution of Poiseuille flow through the lumen in a vessel pressurized with 13 kPa on the endothelium of geometry 2 for different time points. The color bars represent the magnitude of the velocity of Poiseuille flow (mm/sec). The pink dot represents the point (vertex) where the magnitude of velocity is maximum.

Next, we explore the features of hemodynamics for the cross section 3. Cross section 3 features a slightly thickened intima in the stress free reference configuration. We observe a drastic change in the shape of the lumen for cross section 3. We also observe that the lumen gets occluded from the direction where the intima is thicker to begin with. In addition, the magnitude of the flow decreases with time.

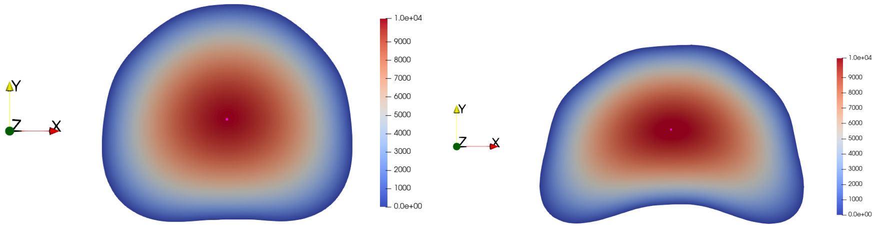

(a) $t = 0$ year.

(b) $t = 1$ year.

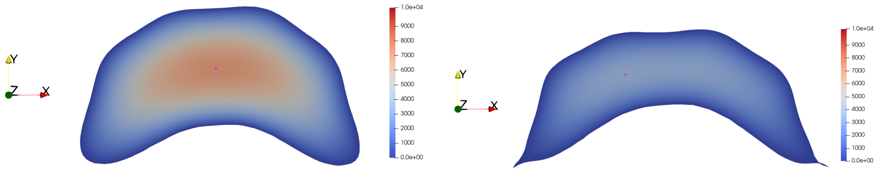

(c) $t = 1.5$ years.

(d) $t = 2$ years.

Figure 5.7: Numerical solution of Poiseuille flow through the lumen in a vessel pressurized with 13 kPa on the endothelium of geometry 3 for different time points. The color bars represents the magnitude of the velocity of Poiseuille flow (mm/sec). The pink dot represents the point (vertex) where the magnitude of velocity is maximum.

We assume the center of flow is always located on a vertex of the lumen mesh. But physically, the position of the center of flow can be inside of an element instead of being on a vertex. Thus an error in the position of the center of flow is introduced. The error is on the order of one edge length of an element. To get an estimate of the error, we need to calculate the average edge length of the elements of the lumen mesh. The average edge length of an element in a mesh of the lumen can be calculated as $\sqrt{\dfrac{\text{Area of lumen}}{\text{Number of elements in the lumen}}}$. If a very coarse mesh is chosen, then a small number of elements is required to mesh the lumen. In that case, the denominator becomes small which then increases the average edge length, leading to a significant error in the position of the center of flow. On the other hand, if a fine mesh with large number of elements is chosen, the average edge length becomes small, leading to a small error. We can calculate the average edge length for the meshes introduced on each of the three cross sections using Table 5.1. For cross sections 1, 2, and 3, the average edge lengths of an element on the lumen are 0.04 mm, 0.11 mm, and 0.09 mm, respectively. So, the average length of the edges of the elements are small. Therefore, we can consider the coordinates of the center of flow to be quite accurate.

Another possible strategy to locate the coordinate for the maximum flow is to fit a local paraboloid and find the coordinate of its vertex. In that case, the accuracy depends on the mesh refinement too. In case the mesh is coarse, the small number of nodes will lead to a paraboloid that is a bad fit, leading to error in locating its vertex. If the mesh is sufficiently refined, the large number of vertices will result in a better fit of the paraboloid, leading to accuracy in its vertex location. So either way, the accuracy of the flow center depends on mesh refinement.

In addition to mesh refinements leading to errors in the position of the center of flow, a translation of the deformed cross sections can also cause a change in the coordinates of the center of flow. If $\mathbf{\Phi}$ minimizes Eq. (2.12), then any constant vector + $\mathbf{\Phi}$ is also a minimizer. To remove this non-uniqueness, we re-centered the cross sections using the center of mass. We calculated the center of mass of the lumen and the arterial wall in the reference stress free configuration. After solving for the displacement fields for the lumen and the arterial wall by minimizing their corresponding energy functionals, we calculated the new center of mass for the lumen and the arterial wall. We then calculated the difference in the center of masses and moved the lumen and the arterial wall back to their center of mass in the reference configuration.

We observe that the center of flow changes rapidly compared to those of the other two cross sections. The magnitude of the flow reduces from $10,250$ mm/sec at $t = 0$ years to 3480 mm/sec at $t = 2$ years. We see corners developing at around $t = 2$ years. These corners lead to an eventual divergence of the code for $t > 2$. It is possible that the corners can be removed by doing a local mesh refinement. We also observe that the lumen tends to be polygonal with time, which is consistent with what we observe for cross section 2, which is due to asymmetry in the geometry.

5.4.2 Evolution of shear stress on the endothelium over time

As the geometry of the lumen changes shape due to growth (of the intima only) and deformation of the three layers, the solution to the Poiseuille flow changes due to the changed shape of the lumen. Since the shear stress on the endothelium depends on the solution to the Poiseuille flow following the relation $\tau = \nu_l[\nabla u + (\nabla u)^T]\mathbf{e}_z \cdot \mathbf{n}$, where $\mathbf{n}$ is the unit normal to the endothelium pointing in the direction of the lumen, the shear stress on the endothelium also evolves as the geometry of the lumen changes shape. In this section, we demonstrate how the distance to the endothelium from the center of flow affects the magnitude of the shear stress for the three different cross section geometries as they evolve over time.

To represent the shear stress on the endothelium, we introduce a polar coordinate system centered at where the magnitude of the Poiseuille flow velocity is maximal (center of flow). In Fig. 5.8, the magnitude of the shear stress along the endothelium is represented by the $\tau(\theta)$. Next, we parameterize the endothelium in terms of angle. One important observation is the difference in the nature of the relation between $r(\theta)$ and $\tau(\theta)$ for cross section 1, which is annular, and for the other two cross sections which are not annular. If we solve the 1D annular model for the Poiseuille flow with the pressure gradient G and radius r, then we get the relation between shear stress and radius as $\tau(\theta) = \frac{Gr}{2}$. This implies that for an annular cross section, the shear stress increases or decreases as the radius increases or decreases, respectively.

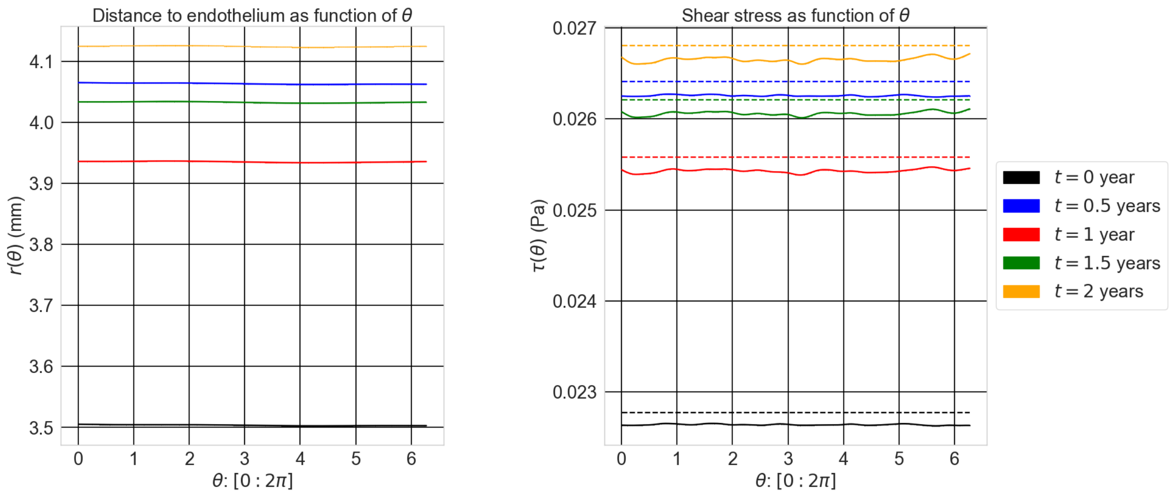

Figure 5.8: Evolution of $r(\theta)$ and $\tau(\theta)$ for cross section 1 with time. $r(\theta)$ and $\tau(\theta)$ are regularized for noise reduction. The dashed lines correspond to the analytical shear stress calculated as $\tau(\theta) = \dfrac{Gr}{2}$, where $G = 0.013$ kPa is the pressure gradient and $r(\theta) = \sqrt{\dfrac{\text{area of lumen}}{\pi}}$ is the numerical radius of the lumen.

In the above figure, we observe that as the $r(\theta)$ increases or decreases with time, the shear stress increases and decreases, respectively. In addition, relation $\tau(\theta) = \frac{Gr}{2}$ agrees with the plot above.

Thus, the magnitude of the shear stress depends highly on the geometry of the lumen, in particular the geometry of the endothelium, as the lumen deforms. For an annular cross section geometry, the relation between $r(\theta)$ and $\tau(\theta)$ are proportional. However, for cross section geometries that are non-annular, the relation between the two becomes inversely related. Here we investigate the relation between $r(\theta)$ and $\tau(\theta)$ for cross sections 2 and 3: see Fig. 5.9.

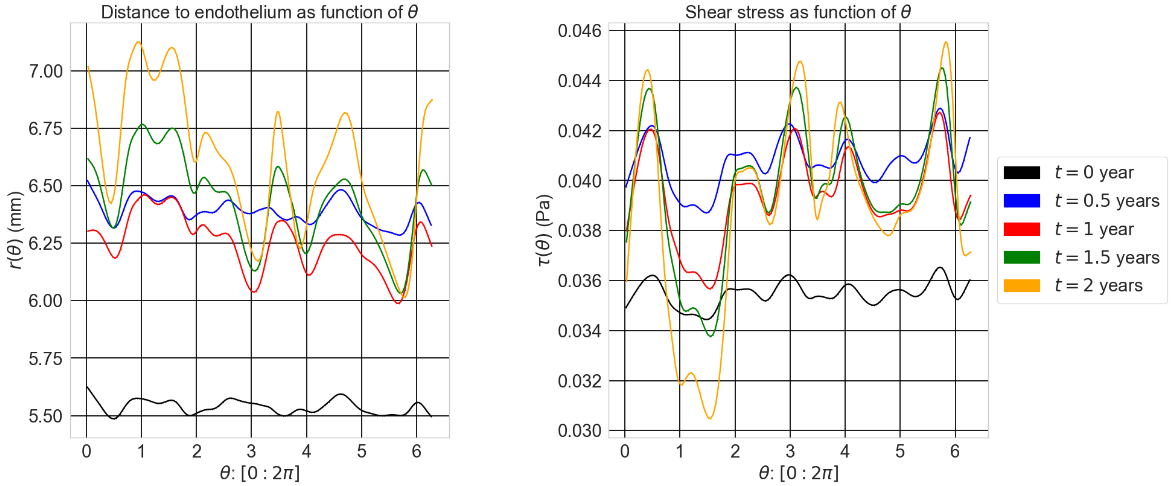

Figure 5.9: Evolution of $r(\theta)$ and $\tau(\theta)$ for cross section 2 with time. $r(\theta)$ and $\tau(\theta)$ are regularized for noise reduction.

In the above figure, we observe that for a given time t, when r is small, τ is large. For example, at time $t = 0$ year, the local minima of $r(\theta)$ correspond to the local maxima of $\tau(\theta)$, implying an inverse relationship between r and τ. This implies that at a particular point of time, if a point on the endothelium is closer to the center of flow, then that point experiences a greater magnitude of shear stress compared to a point that farther away. We observe a similar trend for other time points as well. In the case of an annular cross section, the variables $\tau(\theta)$ and $r(\theta)$ are proportional but for cross sections 2 and 3, there exists an inverse relation between the two variables.

Similarly, in case of cross section 3, we observe a similar relation between $r(\theta)$ and $\tau(\theta)$ as observed in Fig. 5.13 below.

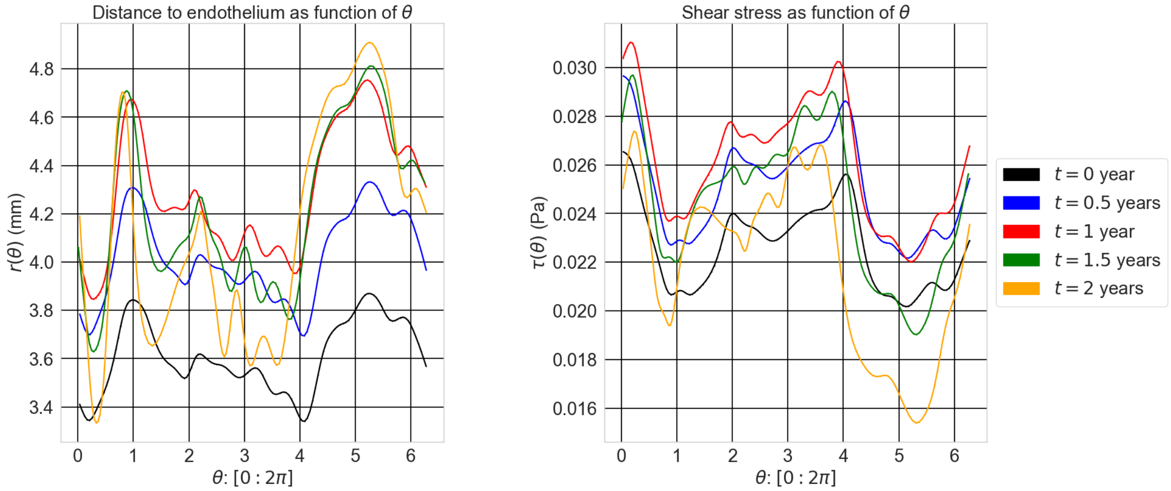

Figure 5.10: Evolution of $r(\theta)$ and $\tau(\theta)$ for cross section 3 with time. $r(\theta)$ and $\tau(\theta)$ are regularized for noise reduction.

5.4.3 Correlations among distance, shear stress, curvature, and PDGF concentration

The endothelial cells release PDGF in a shear-dependent manner. The flux of the PDGF is dependent on the shear stress following the relation $\Gamma = 0.003\dfrac{\tau}{\tau + 0.0003}$. We should note that the flux of PDGF (rather than the amount of PDGF) is dependent on the shear stress. The concentration in the intima is determined by other factors as well, such as the diffusivity of PDGF (D), the degradation of PDGF (k), and also the width of the intima. In this section, we explore how the PDGF concentration along the endothelium is affected by $r(\theta)$, $\tau(\theta)$, and the curvature of the endothelium $\kappa(\theta)$ as the vessel deforms with time. One important feature to look for is how the different cross section geometries (annular and non-annular) affect the relation among the variables. Another area of interest should be the evolution of the PDGF concentration with time and the effect of endothelial curvature on local PDGF concentration.

In this subsection, we discuss the relationships among the variables for the three different cross sections. We start with a discussion for the annular case, cross section geometry 1. As mentioned in Section 5.4.1, as the vessel deforms over time, there is an outward dilation, followed by an inward remodelling, which is again followed by an outward dilation. Since the shear stress at the endothelium is governed by the equation $\tau(\theta) = \dfrac{Gr}{2}$ where τ is shear stress, G is the pressure gradient along the vessel, and r is the radius of the lumen, we expect the flux of the PDGF to be governed by the radius as well. So during the outward dilation, the points on the endothelium are moving away from the center of flow experiencing high shear stress, whereas for an inward remodelling, the points are moving closer to the center of flow experiencing low shear stress. So we expect the flux of PDGF to be high during the initial outward expansion and low during the inward remodelling. In Fig. 5.11 below, PDGF is increasing with time but τ is non-monotonic. So, there is no obvious relation between the PDGF concentration C and τ.

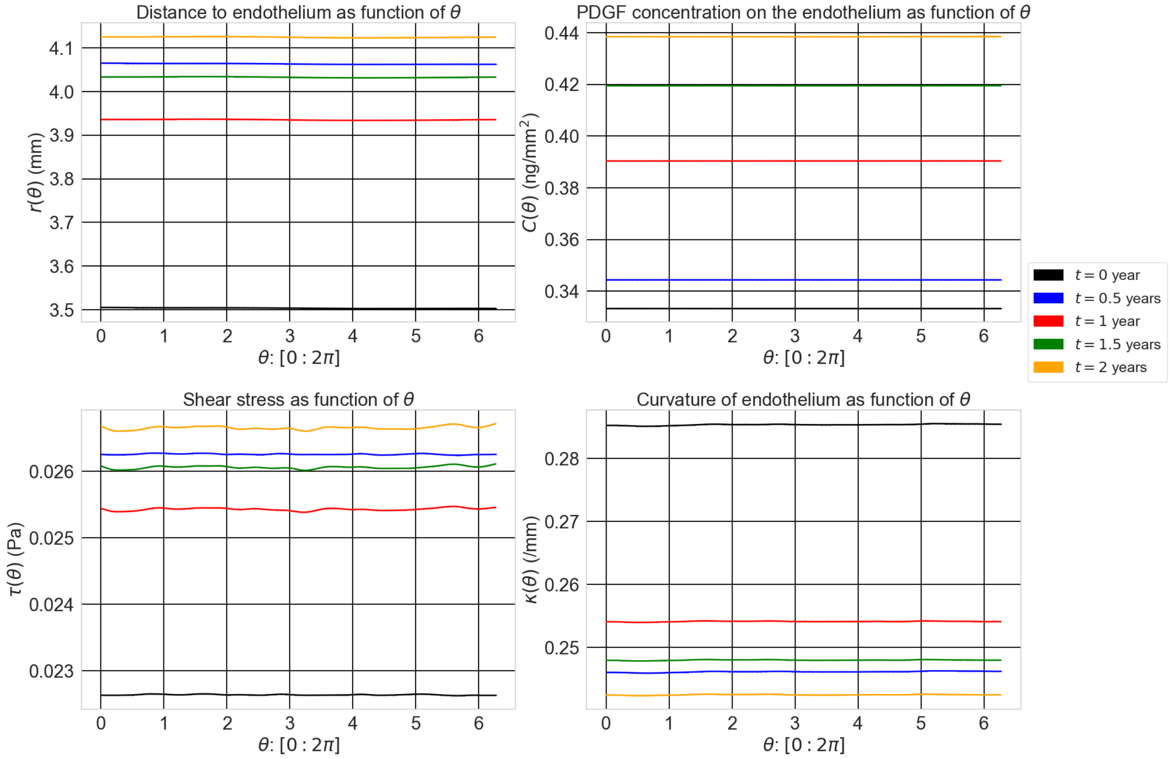

Figure 5.11: Cross section 1: Evolution of the variables of interest over time. All variables are regularized for noise reduction.

The only observation that can be made from the above figure is that the PDGF concentration increases with time. Since for a specific point of time, all the variables, $r(\theta)$, $\tau(\theta)$, $C(\theta)$, and $\kappa(\theta)$, are almost constant, we cannot infer on how the variations in the variables for a specific point of time affect the PDGF concentration $C(\theta)$. The effect becomes more distinct when we consider non-annular geometries.

The effect of angular variation on the PDGF concentration becomes readily observable for non-annular geometries.

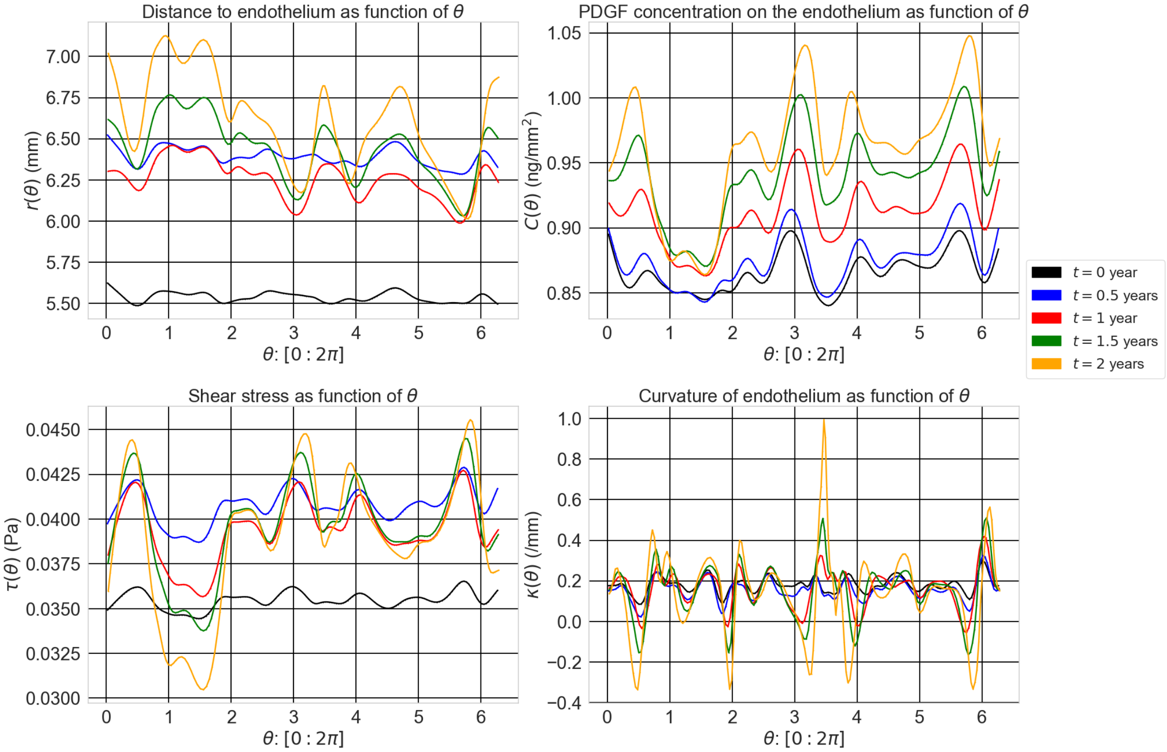

Figure 5.12: Cross section 2: Evolution of the variables of interest over time. All variables are regularized for noise reduction.

The above figure demonstrates the evolution of the variables over time. We find that there are some important correlations between the variables for a given time point. For a given time, we observe that as the distance to the endothelium from the center of flow decreases (increases), the PDGF concentration increases (decreases). Since the distance to the endothelium is measured from the center of flow, this implies that in the course of the deformation of the vessel, if a point on the endothelium comes closer to the center of flow, the PDGF concentration at that point on the endothelium increases and when the point moves further away, the PDGF concentration decreases. Another interesting observation is the relation between shear stress and the curvature of the endothelium at a given time point. There seems to be negative feedback between curvature and shear stress. At a given time point, lower curvature implies greater shear stress, whereas higher curvature implies lower shear stress. This implies that viscous resistance slows down flow in narrowed lumen or in lumen which has sharp areas in the endothelium. Also, as time increases, we observe development of a strong positive correlation between shear stress and the PDGF concentration. In addition, for the non-annular cross sections, local maxima increase in time and local minima decrease in time.

We see a similar trend among the variables for cross section geometry 3 as shown in Fig. 5.13 below.

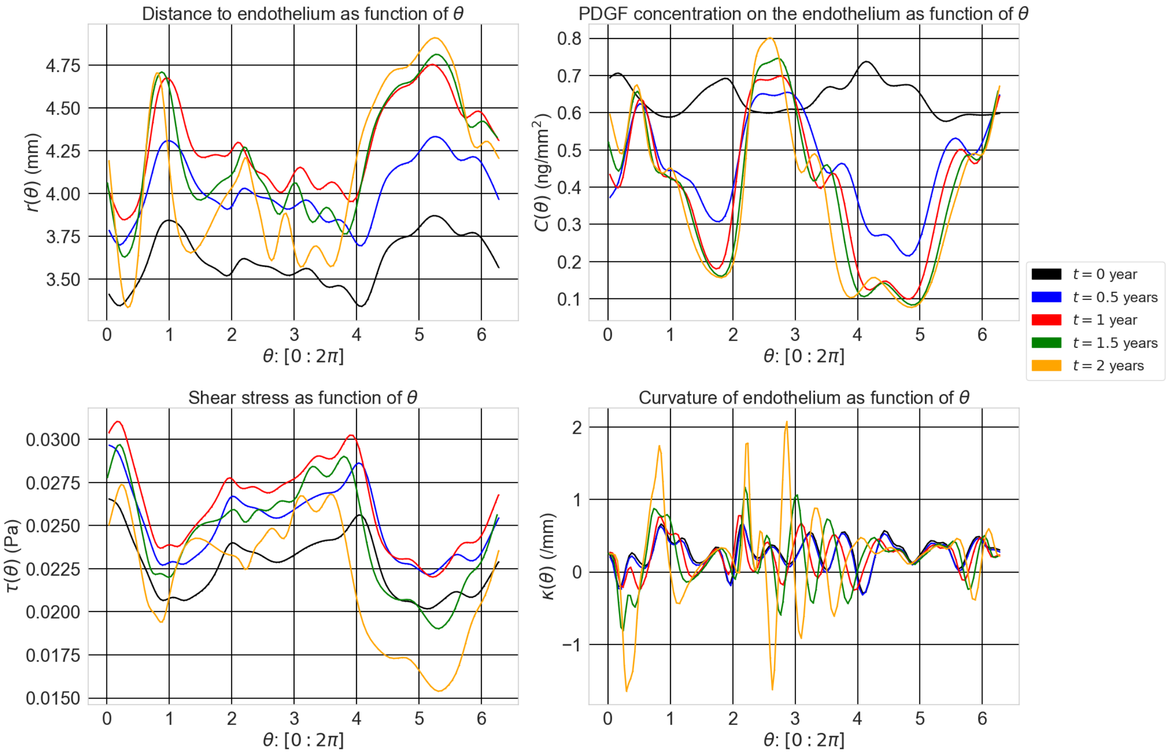

Figure 5.13: Cross section 3: Evolution of the variables of interest over time. All variables are regularized for noise reduction.

Thus, we can see the effect geometry of cross sections have on the shear stress, curvature, and the PDGF concentrations. The correlations among the variables are qualitatively different between the annular and the non-annular cases. From the graphs, the amount of correlation cannot be observed readily. We provide more details on the correlations among the variables in Section 5.6.

5.5 Deformation of arterial wall

In this section, we present the deformation of the arterial wall at times $t = 0$, $t = 1$, $t = 1.5$, and $t = 2$ years for the three cross sections. We demonstrate that thicker intimas grow more quickly than thinner ones. Also, we show that if the cross section is annular in the reference stress free configuration, then it stays annular at later times. For the other cross sections, the endothelium tends to be polygonal with time. In addition, one might think that the intima thickens only if the PDGF concentration is high. We show that this not be always the case. In case of cross section 3, a region can grow faster if the intima is thicker and even if the region has lower PDGF concentration compared to another region of the intima.

For annular cross section 1, since the intima is uniformly thick with respect to angle, the distribution of PDGF at a particular point of time is the same in all directions. As a result, the intima experiences uniform growth angularly. Below is the snapshot of the arterial wall deformation at different time points.

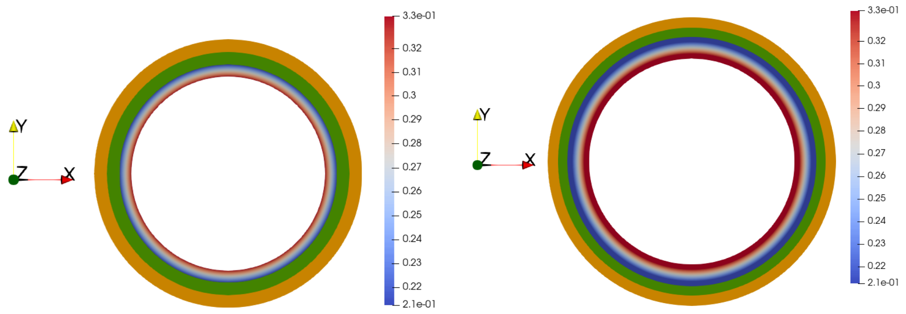

(a) $t = 0$ year.

(b) $t = 1$ year.

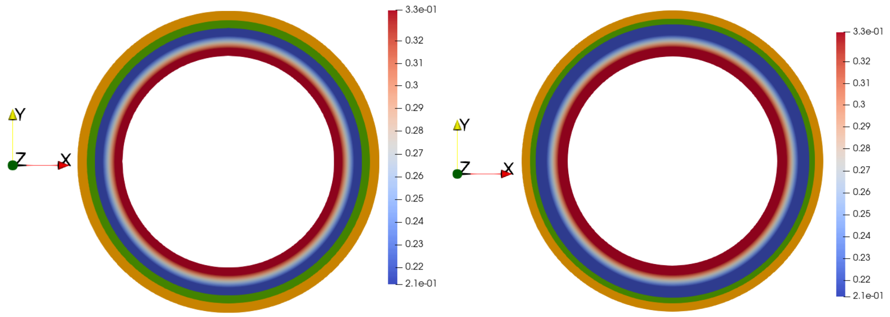

(c) $t = 1.5$ years.

(d) $t = 2$ years.

Figure 5.14: Snapshots of arterial wall remodelling for cross section 1 for four different time points. The color of the intima represents the magnitude of the PDGF concentration. The magnitude are given in the color bar. The units of the PDGF concentration is ng/mm^2.

In the above figure, it is observed that the cross section remains annular for all time points. We speculate that if t is large enough, the symmetry of the cross section will not be conserved. However, the time required to break the symmetry is not the point of this thesis. As mentioned in Section 5.4.1, we observe an interesting remodelling feature as the vessel deforms. For the initial phase, the vessel wall undergoes an outward dilation, in the middle phase, the wall starts to remodel inwards, followed by a last phase of outward remodeling. This "multiple remodeling" feature hasn't been observed before and the reason for this behavior is not clear to us and warrants further investigation. Researchers *have* reported two phase remodeling. In the article [18], Glagov *et. al.* show that there is an initial phase of outward remodeling followed by a later phase of inward remodeling. The authors observe that the inward remodeling begins when the percentage of stenosis exceeds 40%.

We also observe that as the intima grows, the media is getting squeezed more and more, resulting in a loss of area for the media. Also, a circular lumen tends to remain circular (symmetry is preserved for short and intermediate times; see Sections 1.4.1 and 1.4.2 of [20]). In this article, Goriely and Moulton present a sample problem of growth and deformation of an incompressible hyperelastic cylindrical tube. They consider the radial deformation to be uniform along the axis of the tube and focus only on a circular cross section of the tube. The idea is to add a perturbation to a symmetric finite deformation. The important feature of this perturbation is that it does not follow the symmetry of the finite deformation. They show that adding a perturbation leads to instability, resulting in a non-circular cross section.

The mechanics of the arterial wall becomes more interesting when a non-annular cross section is taken into account. In cases of non-annular cross sections, the rate of growth of different regions of the intima are different. The below figure shows the growth of the intima for cross section 2 for different time points.

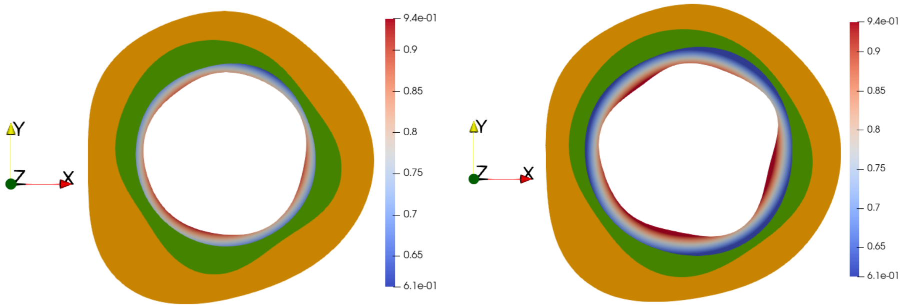

(a) $t = 0$ year.

(b) $t = 1$ year.

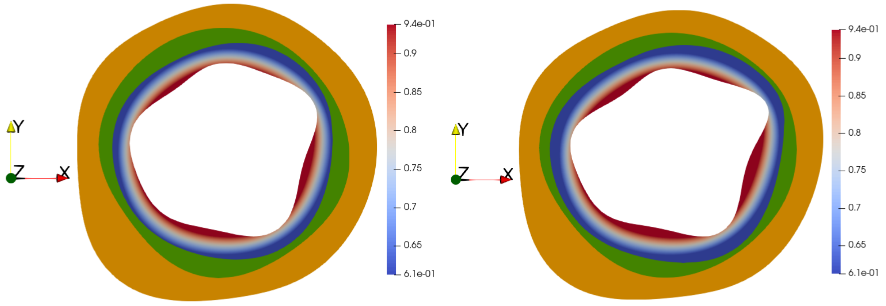

(c) $t = 1.5$ years.

(d) $t = 2$ years.

Figure 5.15: Snapshots of arterial wall remodelling for cross section 2 for four different time points. The color of the intima represents the magnitude of the PDGF concentration. The magnitude are given in the color bar. The units of the PDGF concentration is ng/mm^2.

For cross section 2, we observe that unlike the annular cross section 1, the concentration of PDGF in the intima is not the same in all directions. At $t = 0$ year, there are regions in the intima that have more PDGF concentration compared to other regions. With time, these regions grow more compared to other regions. Thus, different parts of the intima grow at different rates, and the lumen gets occluded at different rates from different directions. At time $t = 0$, we observe that the thicker parts of the intima have more PDGF concentration compared to the thinner regions. At later times, these thicker regions grow more compared to the thinner ones. Therefore, given the PDGF distribution at time $t = 0$ year, one can predict which regions would grow more quickly and the directions along which the intima will occlude the lumen.

From Fig. 5.15, it might seem that regions of cross section 2 that have higher PDGF concentration grow compared to regions that have lower PDGF concentration, the PDGF concentration grows over time, and the thicker parts of the intima have higher PDGF concentration compared to thinner ones. Although these observations are true for cross section 2, they do not hold for cross section 3. For cross section 3, the thicker parts of the intima grows more quickly than the thinner parts and the lumen gets occluded more from the direction where the intima is thicker to start with, i.e., at $t = 0$ year. In cross section 3, the intima is very thick in one direction, the 6 o'clock direction. We can consider cross section 3 to be that of a stage of advanced intimal thickening. Except for regions near the 6 o'clock direction, the intima is more or less uniformly thick. The below figure shows the evolution of the arterial wall of cross section 3 with time.

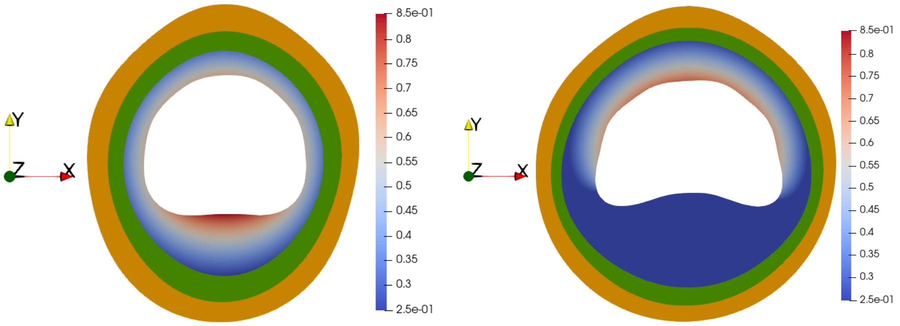

(a) $t = 0$ year.

(b) $t = 1$ year.

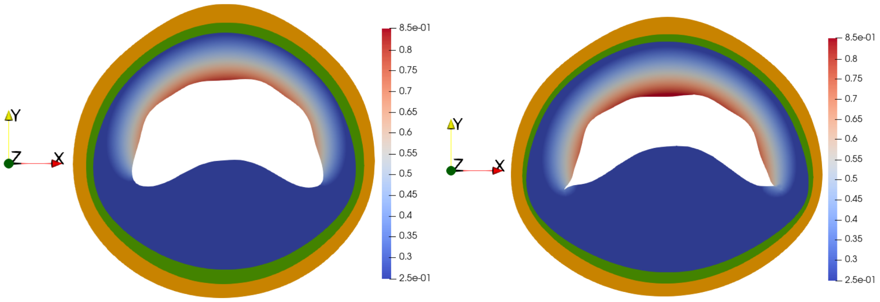

(c) $t = 1.5$ years.

(d) $t = 2$ years.

Figure 5.16: Snapshots of arterial wall remodelling for cross section 3 for four different time points. The color of the intima represents the magnitude of the PDGF concentration. The magnitude are given in the color bar. The units of the PDGF concentration is ng/mm^2.

At time $t = 0$ year, we observe high PDGF concentration in the 6 o'clock direction. From the observations we made in the case of cross section 2, it is natural to make the inference that the PDGF concentration at this region will continue to grow with time. However, such is not the case. The PDGF concentration at the 6 o'clock diminishes with time. But even with a diminishing PDGF concentration, the region grows quicker than the region at 12 o'clock position that develops a greater concentration of PDGF over time but grows more slowly comparatively. Thus, it is true that thicker intimas grow more quickly than the thinner ones, and this observation holds true for both cross sections 2 and 3. One reason to account for the diminishing PDGF concentration is that the center of flow moves away from the 6 o'clock region towards the 12 o'clock region as the lumen deforms over time.

Thus, we can conclude that the thickness of the intima at time $t = 0$ year is a major determinant of which regions grow more faster compared to other regions. Given the thickness of the intima at time at time $t = 0$ year and the parameters for flow and the material parameters, we can predict the time it takes for reaching a certain percentage of stenosis, provided the parameters of blood flow do not change with time as the vessel deforms.

In some experimental setups, often the arterial specimens are depressurized before sectioned and examined. This corresponds to lumen pressure of $P = 0$ kPa. We simulate these depressurized cross sections 2 and 3 and show them in Fig. 5.17 below.

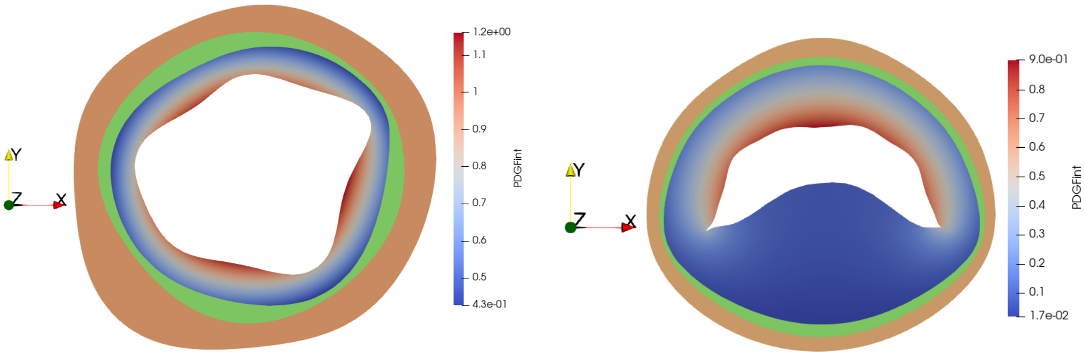

(a) Depressurized cross section 2

(b) Depressurized cross section 3

Figure 5.17: (a) Depressurized cross section 2 at $t = 2$ years with $P = 0$ kPa and constant PDGF concentration in the intima. (b) Depressurized cross section 3 at $t = 2$ years with $P = 0$ kPa and constant PDGF concentration in the intima.

5.6 Metrics of remodelling

The plots in Section 5.4.3 require a further investigation into the amount of correlation among the variables $r(\theta)$, $\tau(\theta)$, $C(\theta)$, and $\kappa(\theta)$. In this section, we present the Pearson correlation coefficients among the different variables. This helps us determine the association between the different variables of interest. We observe an interesting evolution of the correlation coefficients with time for different cross sections.

For cross section 1, there are analytic solutions relating the variables. There is a direct relation between the radius, r, and shear stress, τ, given by $\tau(\theta) = \dfrac{Gr}{2}$ where G is the pressure gradient along the vessel. While τ and r are proportional, the variables r and κ have an inverse relation between them given by $\kappa = \dfrac{1}{r}$. As we observed in Fig. 5.11, there seems to be no obvious relation between $C(\theta)$ and $\tau(\theta)$.

For the non-annular cross sections 2 and 3, we see significant values of the correlation coefficient. Below are the correlation coefficients for cross section 2 at different time points.

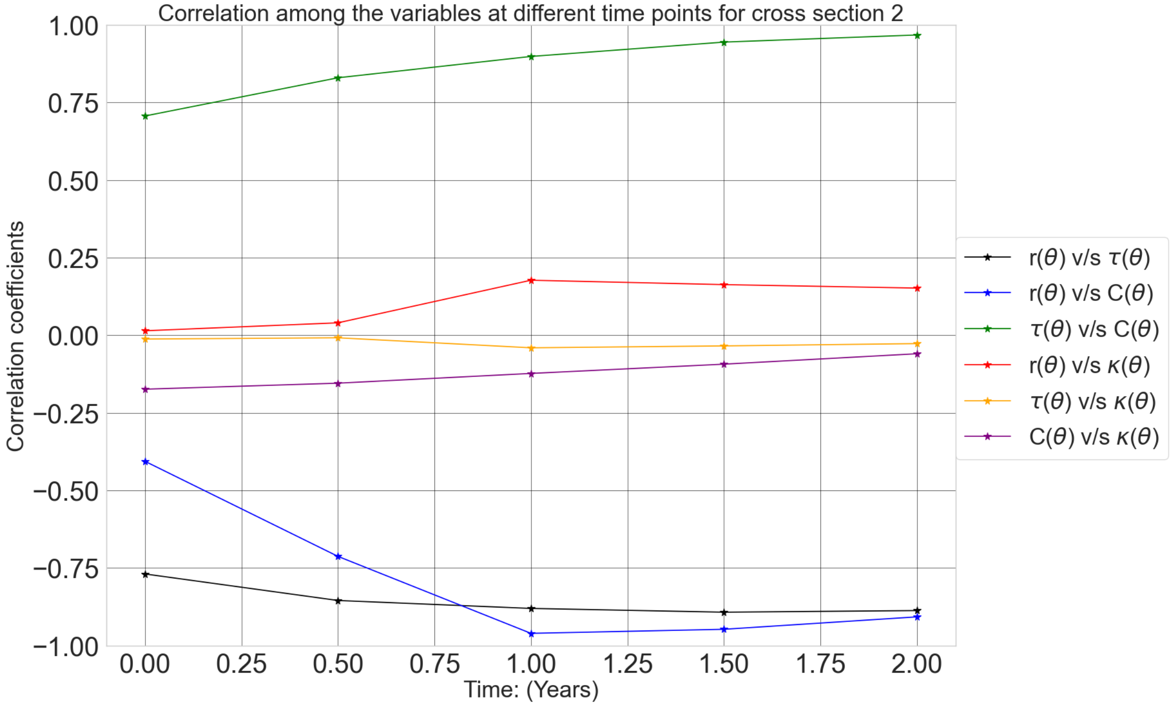

Figure 5.18: Evolution of correlation coefficients among the variables $r(\theta)$, $\tau(\theta)$, $C(\theta)$, and $\kappa(\theta)$ for cross section 2 with time.

We now observe an inverse relation between $r(\theta)$ and $\tau(\theta)$. This implies that as a point on the endothelium moves away from the center of flow, the shear stress at that point decreases for cross section 2 unlike for the case of cross section 1 where the shear stress increases (decreases) as the points on the endothelium moves away (closer) to the center of flow. The below figure represents the scatter plots and the regression lines to demonstrate the strength of the correlation between $r(\theta)$ and $\tau(\theta)$ for cross section 2.

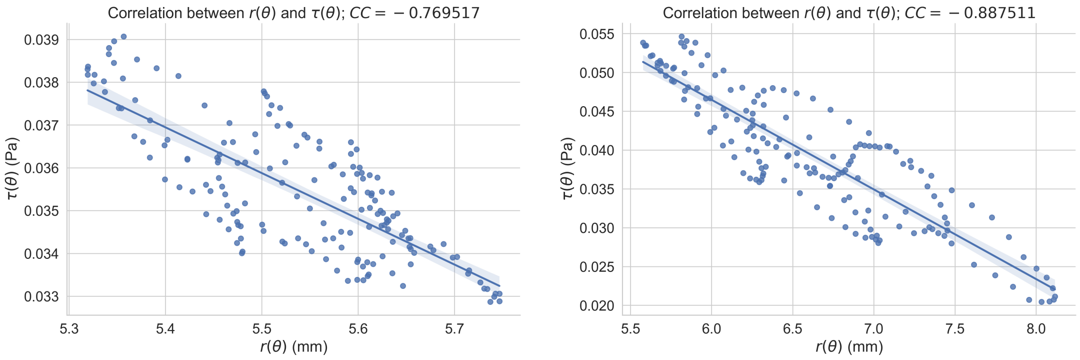

(a) $t = 0$ year.

(b) $t = 2$ years.

Figure 5.19: Regression plots between $r(\theta)$ and $\tau(\theta)$ for cross section 2. CC denotes Pearson's correlation coefficient. The light blue region represents the 95% CI.

Another interesting correlation is that between $r(\theta)$ and the PDGF concentration $C(\theta)$. They are inversely related and the correlation coefficient tends to -1 as $t \to 2$ years. This also implies that as $r(\theta)$ increases, the PDGF concentration $C(\theta)$ decreases. So as a point moves away from the center of flow, it experiences less concentration of PDGF. In the below regression plots, we observe that at time $t = 0$ years, there is a weak negative correlation between $r(\theta)$ and $C(\theta)$. However, as time increases, the two variables become more negatively correlated, suggesting that the PDGF concentration at a point on the endothelium increases (decreases) as the point moves closer to (away from) the center of flow.

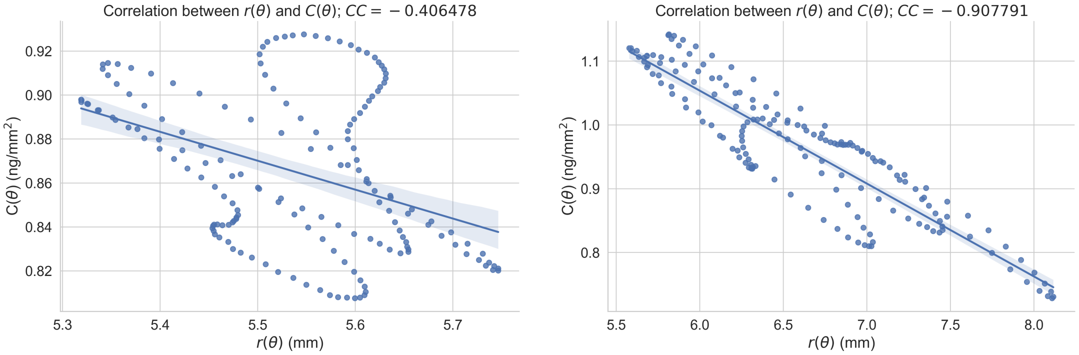

(a) $t = 0$ year.

(b) $t = 2$ years.

Figure 5.20: Regression plots between $r(\theta)$ and $C(\theta)$ for cross section 2. CC denotes Pearson's correlation coefficient. The light blue region represents the 95% CI.

In addition, for cross section 2, we observe a strong positive correlation between $\tau(\theta)$ and the PDGF concentration $C(\theta)$ with the correlation coefficient almost 1. Although the flux of PDGF is related to the shear stress and not the PDGF concentration itself, this correlation suggests that the PDGF concentration increases as the shear stress increases. Since $r(\theta)$ has an inverse relation with $\tau(\theta)$ as observed in Fig. 5.19, and $r(\theta)$ has an inverse relation with $C(\theta)$ as observed in Fig. 5.20, we can explain the strong positive correlation between $\tau(\theta)$ and $C(\theta)$.

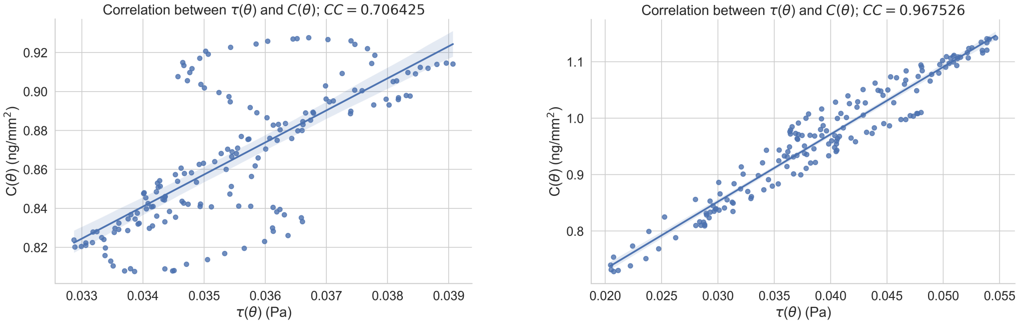

(a) $t = 0$ year.

(b) $t = 2$ years.

Figure 5.21: Regression plots between $\tau(\theta)$ and $C(\theta)$ for cross section 2. CC denotes Pearson's correlation coefficient. The light blue region represents the 95% CI.

There exists a weak positive correlation between $r(\theta)$ and the curvature $\kappa(\theta)$ while the variables $\tau(\theta)$ and $\kappa(\theta)$ exhibit a weak inverse relation between them. The variables $C(\theta)$ and $\kappa(\theta)$ also have an inverse relation between them. At time $t = 0$ years, they have a weak negative correlation, but as time progresses, they tend to become uncorrelated.

Figs. 5.19, 5.20, and 5.21 raise some very interesting questions in case of cross section 2, the investigation of which is beyond the scope of this research: can the concentration of PDGF at a particular point in the intima and the magnitude of shear stress at the endothelium be modeled as a function of the distance of the point from the center of flow? Can the PDGF concentration at the endothelium be modeled as a function of the shear stress?

The strong relations between $r(\theta)$ and $\tau(\theta)$, $r(\theta)$ and $C(\theta)$, and $\tau(\theta)$ and $C(\theta)$ are a consequence of the geometry of cross section 2. We show next that the relations and the correlation coefficients between the variables differ for cross section 3. Thus, an interesting observation is how the correlation coefficients between variables in cross section 2 change as we move on to cross section 3. The correlation coefficients for cross section 3 over time are as follows:

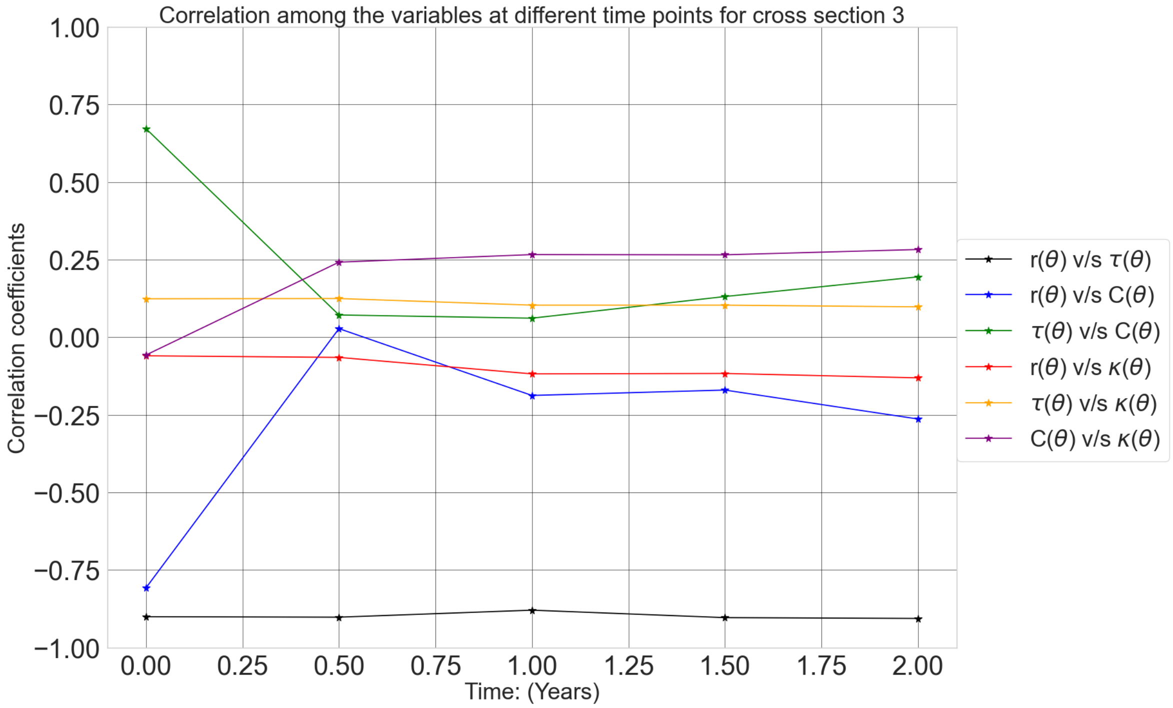

Figure 5.22: Evolution of correlation coefficients among the variables $r(\theta)$, $\tau(\theta)$, $C(\theta)$, and $\kappa(\theta)$ for cross section 3 with time.

There are some important observations we can make from the above figure. We observe that $r(\theta)$ and $\tau(\theta)$ are inversely related for the given time points with the correlation coefficient close to -1. The regression plots for $r(\theta)$ and $\tau(\theta)$ are shown in Fig. 5.23 below.

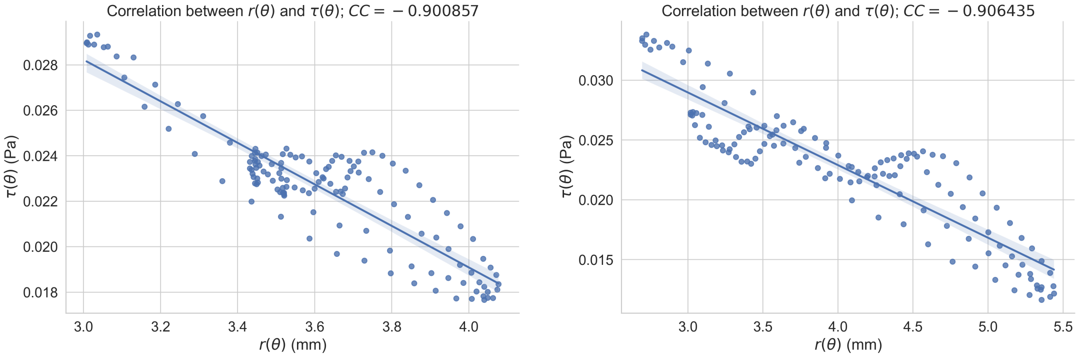
Correlation between $r(\theta)$ and $\tau(\theta)$; $CC = -0.900857$

Correlation between $r(\theta)$ and $\tau(\theta)$; $CC = -0.906435$

(a) $t = 0$ year.

(b) $t = 2$ years.

Figure 5.23: Regression plots between $r(\theta)$ and $\tau(\theta)$ for cross section 3. CC denotes Pearson's correlation coefficient. The light blue region represents the 95% CI.

The correlation coefficient between $r(\theta)$ and $C(\theta)$ first increases and then decreases with time. At time $t = 0$, we observe a strong negative correlation between the variables, but as time increases, the variables exhibit a weak negative correlation.

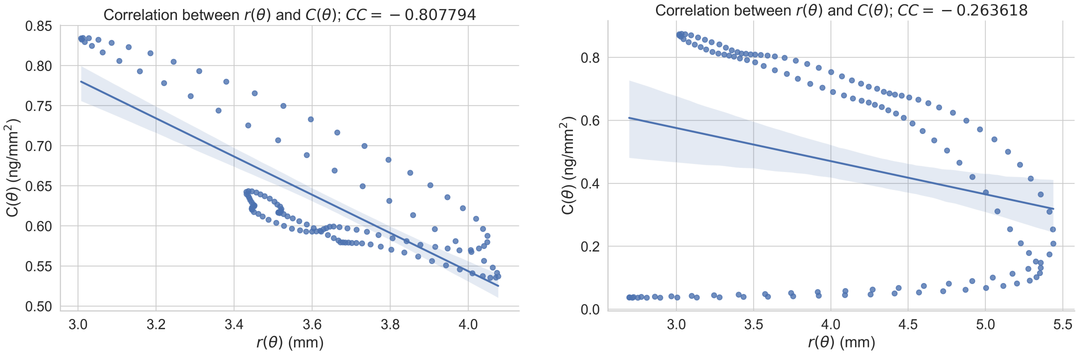
Correlation between $r(\theta)$ and $C(\theta)$; $CC = -0.807794$

Correlation between $r(\theta)$ and $C(\theta)$; $CC = -0.263618$

(a) $t = 0$ year.

(b) $t = 2$ years.

Figure 5.24: Regression plots between $r(\theta)$ and $C(\theta)$ for cross section 3. CC denotes Pearson's correlation coefficient. The light blue region represents the 95% CI.

The variables $\tau(\theta)$ and $C(\theta)$ are directly related. The correlation coefficient decreases and then increases. But the two variables maintain a direct relationship throughout time.

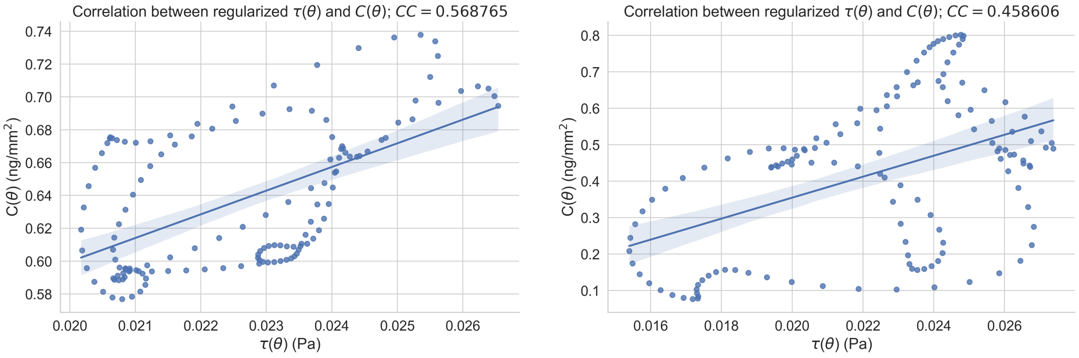

(a) $t = 0$ year.

(b) $t = 2$ years.

Figure 5.25: Regression plots between $\tau(\theta)$ and $C(\theta)$ for cross section 3. CC denotes Pearson's correlation coefficient. The light blue region represents the 95% CI.

The variables $r(\theta)$ and $\kappa(\theta)$ exhibit a weak negative correlation and the correlation coefficient stays roughly the same through time. This implies that the variables are inversely related and the relation does not change with time. The variables $\tau(\theta)$ and $\kappa(\theta)$ exhibit a direct relation throughout time. On the other hand, the two variables, $C(\theta)$ and $\kappa(\theta)$, are inversely related at $t = 0$ years but develops a direct relation at $t = 0.5$ years.

An important takeaway is that the sign of the correlation coefficients are preserved for later times for cross sections 2 and 3. Also, for cross sections 2 and 3, there is a negative correlation between $r(\theta)$ and $\tau(\theta)$. As the distance of a point on the endothelium moves away from the center of flow, it experiences less shear stress, resulting in reduced flux of PDGF. On the other hand, if a point moves closer to the center of flow, it experiences high shear stress, resulting in greater flux of PDGF from the endothelium to the intima. Another important observation is how the correlation coefficient between $\tau(\theta)$ and $C(\theta)$ varies when the geometry is changed. For cross section 2, $r(\theta)$ and $C(\theta)$ have a strong negative correlation compared to cross section 3. For cross section 3, the two variables seem to become uncorrelated as time increases. These observations raise two interesting questions: first, what effect does a cross section geometry have on the strength of the correlation among the variables? Second, how does the strength of correlation change as time increases? For the simulations presented in this thesis, we have considered $t = 2$ years to be the final time. If we stretch time beyond 2 years, other interesting correlations may emerge among the variables.

CONCLUSIONS

In this thesis, we constructed a model for intimal thickening in which growth depends on shear stress from a Poiseuille flow. The model illustrates how hemodynamics can influence arterial morphology. The shear stress profile along the endothelium has a strong negative correlation with the distance to the endothelium from the center of flow. Also, the shape of the lumen tends to be polygonal with time. This thesis also incorporates a new technique of using numerical conformal maps to compute the fiber field in a general arterial cross section. With this technique, we get a smooth distribution of fiber fields that can be used directly in the strain energy functional.

We modeled the PDGF flux across the endothelium as a function of shear stress. The flux is a Hill function of the shear stress induced by the blood flow. This implies that as shear stress increases the flux of PDGF saturates. The endothelial cells have a maximum capacity to produce PDGF. As a result, as the shear stress increases, the flux of PDGF saturates to a maximum value. To account for PDGF transport, we solve a diffusion-degradation equation subject to the fact that the flux of PDGF from the endothelium is upregulated by the shear stress induced by the Poiseuille flow through the lumen. In addition to the PDGF concentration, the growth of the intima and the deformation of the vessel wall is also governed by the mechanical properties of each of the layers (intima, media, and adventitia). We take into account the different mechanical properties of each of the layers in constructing the strain energy density functions for each of the layers.

A PDGF-induced growth of the intima and deformation of a vessel cross section changes the total potential energy of the system, which is represented by an energy functional that involves strain energy density functions for each of the layers. We define the strain energy density functions for each of the layers using hyperelasticity and morphoelasticity implemented through a finite element method. In order to find the optimal deformation, one needs to find an optimal displacement field. We find the displacement field by minimizing the energy functional.

The shape of the lumen deforms according to the deformation of the arterial wall. During the initial expansion of the arterial wall, the lumen dilates whereas in the remodeling phase, the lumen shrinks. Since the blood flows through the lumen and the lumen shape changes with time, the solution to the Poiseuille flow equation also changes with time. To numerically simulate the blood flow through the changing lumen using finite element methods, we need a mesh on the lumen. So, we have two meshes which are used differently: a mesh for the arterial wall and a mesh for the lumen. They share the endothelium as a common boundary. We introduce a strain energy density function for the lumen, assuming the lumen to be filled with highly compressible material. We then minimize the energy functional, subject to a Dirichlet boundary condition that the displacement field is continuous across the endothelium. The resulting displacement field gives rise to a lumen mesh that remains regular over time.

The collagen fibers associated with each of the layers play an important role in dictating the stiffness and deformation of each of the layers. While there are techniques like interpolation and probability distributions that are used to model the distribution of fibers, we implemented a new technique of modeling the fiber fields using numerical conformal maps. Using this technique, we map each of the layers to an annulus, which has outer radius 1 and inner radius ρ (conformal modulus). For each point in the physical cross section, we apply a forward conformal map to find a corresponding point on the annulus. We then find the unit normal vector at the mapped point. Using an inverse conformal map, we map the unit normal vector back to a vector at the point on the physical cross section. Using this technique for each of the layers, we created a smoothly varying fiber fields in each of the layers. The fibers have different inclination angles for each of the layers. At the IEL (interface between the intima and media), we assigned the inclination angle of the fibers to that of the intima while at the media–adventitia interface, we defined the angle of inclination to be that of the adventitia. The reasons for choosing a conformal map is that it preserves angles and that the fiber field in an annulus is easy to determine since the fibers are circumferential; they are the unit normal vectors at each of the points on the annulus. Since conformal maps preserve angles, the fibers at the boundaries of the layers stay tangential and do not cross from one layer to the next.

We also calculate the correlations among the different variables ($r(\theta)$, $\tau(\theta)$, $C(\theta)$, and $\kappa(\theta)$ with all variables measured from the center of flow) for cross sections 2 and 3. For cross sections 2 and 3, we observe positive correlations between $\tau(\theta)$ and $C(\theta)$, $r(\theta)$ and $\kappa(\theta)$. On the other hand, we observe an inverse relationship between $C(\theta)$ and $\kappa(\theta)$, $r(\theta)$ and $C(\theta)$, $\tau(\theta)$ and $\kappa(\theta)$, $r(\theta)$ and $\tau(\theta)$. These observations suggest that for cross sections 2 and 3, as the shear stress increases (decreases), the PDGF concentration along the endothelium increases (decreases). Also, as the distance to the endothelium from the center of flow increases (decreases), the curvature of the endothelium increases (decreases). On the other hand, as the curvature of the endothelium increases (decreases), the PDGF concentration along the endothelium decreases (increases); as the distance to the endothelium from the center of flow increases (decreases), the PDGF concentration along the endothelium decreases (increases); as the shear stress on the endothelium increases (decreases), the curvature of the endothelium decreases (increases); and as the distance to the endothelium from the center of flow increases (decreases), the shear stress decreases (increases). Since all the variables are measured from the center of flow or are parameterized with respect to the coordinates of the center of flow, the above observations strongly suggest that the center of flow and its distance to the endothelium is a crucial factor in determining the magnitude of the variables for cross sections 2 and 3. In order to find the center of flow, one needs to find the solution of the Poiseuille flow numerically, thus introducing error in the center of flow. Thus, it is necessary to regularize the variables by fitting splines to them.

Finally, we implement spline interpolation to reduce noise in data (regularization). The framework of the mathematical formulations and the simulations involves a finite element method. As a result, there are numerical errors introduced in the calculations. These errors affect the accuracy in the calculation of the variables $r(\theta)$, $\tau(\theta)$, $C(\theta)$. To reduce the noise, we fit a spline to each of the variables. To calculate $\kappa(\theta)$, we differentiate the spline fit through $r(\theta)$. This reduces the noise in both $r(\theta)$ and $\kappa(\theta)$. Since finding $\kappa(\theta)$ involves numerical differentiation of $r(\theta)$, if there is noise in $r(\theta)$, then it gets amplified when differentiated, introducing noise in $\kappa(\theta)$.

However, there are 5 limitations of this study. First, the blood flow is highly idealized. In reality, the blood flow through the lumen is pulsatile. In our work, we have assumed that as the vessel deforms with time, the pressure gradient across the vessel remains constant, the viscosity of blood remains constant with time, and the blood pressure is constant with time. These simplifying conditions allow a focused investigation of how intimal thickening is promoted by shear stress. The second limitation of our study is that the collagen fibers in the three layers have a spatially smooth distribution. In reality, the orientation is random and can be modeled using probability distributions. As a result of this limitation, the results from our study will deviate from studies that incorporate probabilistic models for the fiber orientations. Third, we haven't considered the production of PDGF by the smooth muscle cells (SMCs) in the intima or media and we are also neglecting the flux of SMCs from the media to the intima through the internal elastic lamina towards regions of higher PDGF concentration. Fourth, we assumed there is no growth in the media. However, the media does experience growth and becomes thicker with time. Finally, in reality, a healthy intima starts out as a very thin layer. To simulate an initially thin intima, we have to resolve it with many small elements. This increases the time complexity of the algorithm. The intima in all the cross sections of our simulation start off much thicker than a typical healthy intima.

In spite of the above limitations of our model, it provides a clear insight into the dynamics of intimal growth due to hemodynamical shear stresses and highlights the intricate relation between the cross section geometry and intimal growth. Growth and hemodynamics have been studied separately in a lot of detail but there are none (to our knowledge) that combines the two. It introduces a new approach to compute fiber fields in a 2D vessel cross section using numerical conformal maps. In addition, it introduces a new method of meshing the lumen to compute and simulate a Poiseuille blood flow through an evolving lumen geometry.

An evolving lumen can be mapped to an annular disk with the help of numerical conformal maps. This raises the possibility of solving the Poiseuille flow in a disk and then with the help of the inverse conformal map, calculating the Poiseuille flow on the evolving lumen geometry. However, the construction of the conformal map can be unstable in some cases because of the *crowding phenomenon*.

This thesis raises several interesting aspects that warrant further investigations. We can enrich our model further by considering a more realistic blood flow. Inclusion of more interesting transport processes and signalling factors in the arterial wall will help us create a more realistic model. Incorporating the dynamics of lipid trafficking into our model can also provide some interesting insights on plaque progression. Also coupling hemodynamics with plaque progression can provide some answer to some interesting questions: What is the role of geometry in determining the rate of atherosclerosis? How does hemodynamics affect the progression of plaques? What is the effect of hemodynamics on atherosclerosis at vessel arches and bifurcations? What are the correlations among the variables $r(\theta)$, $\tau(\theta)$, $C(\theta)$, and $\kappa(\theta)$ for different cross section geometries? Do the results from this thesis apply to cross section geometries (apart from bifurcations and arches) taken from medical imaging data?

This thesis can be considered as a stepping stone to further investigations into the relation between the local geometry of the endothelium and intimal growth; and the interplay between cross section geometry, hemodynamics, and atherosclerosis.

GitHub Link: https://github.com/avishmj/intimal-thickening

BIBLIOGRAPHY

[1] A.C. Akyildiz, C-K. Chai, C.W.J. Oomens, A.v.d. Lugt, F.P.T. Baaijens, G.J. Strijkers, and F.J.H. Gijsen. 3D fiber orientation in atherosclerotic carotid plaques. *Journal of Structural Biology*, 200:28–35, 2017.

[2] A. Aminbaksh and G.B.J. Mancini. Carotid intima-media thickness measurements: What defines an abnormality? a systemic review. *Clinical and Investigative Medicine*, 22:149–157, 1999.

[3] F. Cacho, P.J. Elbischger, J.F. Rodríguez, M. Doblaré, and G.A. Holzapfel. A constitutive model for fibrous tissues considering collagen fiber crimp. *International Journal of Non-Linear Mechanics*, 42:391–402, 2007.

[4] E. Cecchi, C. Giglioli, S. Valente, C. Lazzeri, G.F. Gensini, R. Abbate, and L. Mannini. Role of hemodynamic shear stress in cardiovascular disease. *Atherosclerosis*, 214(2):249–256, 2011.

[5] J.J. Chiu and S. Chien. Effects of disturbed flow on vascular endothelium: Pathophysiological basis and clinical perspectives. *Physiological Reviews*, 91(1):327–387, 2011.

[6] M. Cobble and B. Bale. Carotid intima-media thickness: Knowledge and application to everyday practice. *Postgraduate Medicine*, 122(1):10–18, 2010.

[7] J. Davignon and P. Ganz. Role of endothelial dysfunction in atherosclerosis. *Circulation*, 109(23_suppl_1):III–27–III–32, 2004.

[8] J.M. Dolan, J. Kolega, and H. Meng. High wall shear stress and spatial gradients in vascular pathology: A review. *Ann Biomed Eng*, 41:1411–1427, 2013.

[9] E. Falk. Pathogenesis of atherosclerosis. *Journal of the American College of Cardiology*, 47(8_Supplement):C7–C12, 2006.

[10] V. Fernández-Alvarez, M.L. Sánchez, F.L. Alvarez, C.S. Nieto, A.A. Mäkitie, K.D. Olsen, and A. Ferlito. Evaluation of intima-media thickness and arterial stiffness as early ultrasound biomarkers of carotid artery atherosclerosis. *Cardiology and therapy*, 11(2):231–247, 2022.

[11] P.W. Fok and K. Gou. Finite element simulation of intimal thickening in 2D multi-layered arterial cross sections by morphoelasticity. *Computer Methods in Applied Mechanics and Engineering*, 363, 2020.

[12] M. Frâncu, A. Asgeirsson, K. Erleben, and M.J.L. Rønnow. Locking-proof tetrahedra. *ACM Transactions on Graphics (TOG)*, 40(2):1–17, 2021.

[13] M.H. Friedman, O.J. Deters, C.B. Bargeron, G.M. Hutchins, and F.F. Mark. Shear-dependent thickening of the human arterial intima. *Atherosclerosis*, 60:161–171, 1986.

[14] E. Gabryś, M. Rybaczuk, and A. Kedzia. Fractal models of circulatory system. symmetrical and asymmetrical approach comparison. *Chaos, Solitons Fractals*, 24(3):707–715, 2005.

[15] T.C. Gasser, R.W. Ogden, and G. A. Holzapfel. Hyperelastic modelling of arterial layers with distributed collagen fibre orientations. *J. R. Soc. Interface*, 3:15–35, 2006.

[16] T.C. Gasser, R.W. Ogden, and G.A. Holzapfel. Hyperelastic modelling of arterial layers with distributed collagen fibre orientations. *Journal of The Royal Society Interface*, 3(6):15–35, 2005.

[17] F.J.H. Gijsen, E. Allanic, F.N. van de Vosse, and J.D. Janssen. The influence of the non-Newtonian properties of blood on the flow in large arteries: unsteady flow in a 90° curved tube. *Journal of Biomechanics*, 32(7):705–713, 1999.

[18] S. Glagov, E. Weisenberg, C.K. Zarins, R. Stankunavicius, and G.J. Kolettis. Compensatory enlargement of human atherosclerotic coronary arteries. *New England Journal of Medicine*, 316(22):1371–1375, 1987.

[19] C.K. Glass and J.L. Witztum. Atherosclerosis: the road ahead. *Cell*, 104(4):503–516, 2001.

[20] A. Goriely and D. Moulton. *The Physics and Mechanics of Biological Systems.* Oxford University Press, 2011.

[21] G.K. Hansson and A. Hermansson. The immune system in atherosclerosis. *Nature immunology*, 12(3):204–212, 2011.

[22] J.M. Haugh. Deterministic model of dermal wound invasion incorporating receptor-mediated signal transduction and spatial gradient sensing. *Biophysical Journal*, 90(7):2297–2308, 2006.

[23] M. Heron and R.N. Anderson. Changes in the leading cause of death: Recent patterns in heart disease and cancer mortality. *NCHS data brief*, 254, 2016.

[24] G.A. Holzapfel. *Nonlinear solid mechanics : a continuum approach for engineering.* Wiley, 2001.

[25] G.A. Holzapfel. *Nonlinear solid mechanics: a continuum approach for engineering science.* Kluwer Academic Publishers Dordrecht, 2002.

[26] G.A. Holzapfel, R.W. Ogden, and S. Sherifova. On fibre dispersion modelling of soft biological tissues: a review. *Proc. R. Soc. A*, 475, 2019.

[27] G.A. Holzapfel, G. Somme, C.T. Gasser, and P. Regitnig. Determination of layer-specific mechanical properties of human coronary arteries with nonatherosclerotic intimal thickening and related constitutive modeling. *American Journal of Physiology-Heart and Circulatory Physiology*, 289(5):H2048–H2058, 2005.

[28] G.A. Holzapfel, G. Sommer, C.T. Gasser, and P. Regitnig. Determination of layer-specific mechanical properties of human coronary arteries with nonatherosclerotic intimal thickening and related constitutive modeling. *Am J Physiol Heart Circ Physiol*, 289:H2048–H2058, 2005.

[29] H.J. Hsieh, N.Q. Li, and J.A. Frangos. Shear stress increases endothelial platelet-derived growth factor mRNA levels. *American Journal of Physiology-Heart and Circulatory Physiology*, 260(2):H642–H646, 1991.

[30] N.X. Hung, S.P.A. Bordas, and N.D. Hung. Addressing volumetric locking and instabilities by selective integration in smoothed finite elements. *Communications in Numerical Methods in Engineering*, 25(1):19–34.

[31] M. Jahangiri, M. Saghafian, , and M.R. Sadeghi. Numerical simulation of hemodynamic parameters of turbulent and pulsatile blood flow in flexible artery with single and double stenoses. *Journal of Mechanical Science and Technology*, 29:3549–3560, 2015.

[32] B.M. Johnston, P.R. Johnston, S. Corney, and D. Kilpatrick. Non-Newtonian blood flow in human right coronary arteries: steady state simulations. *Journal of Biomechanics*, 37(5):709–720, 2004.

[33] J.E. Moore Jr, C. Xu, S. Glagov, C.K. Zarins, and D.N. Ku. Fluid wall shear stress measurements in a model of the human abdominal aorta: oscillatory behavior and relationship to atherosclerosis. *Atherosclerosis*, 110:225–240, 1994.

[34] S. Katsuda, Y. Okada, T. Minamoto, Y. Oda, Y. Matsui, and I. Nakanishi. Collagens in human atherosclerosis: Immunohistochemical analysis using collagen type-specific antibodies. *Arteriosclerosis and Thrombosis: A Journal of Vascular Biology*, 12, 1992.

[35] A. Knowles and R.J. Renka. Methods for numerical differentiation of noisy data. *Electronic Journal of Differential Equations*, pages 235–246, 2014.

[36] M. Kroon. A continuum mechanics framework and a constitutive model for remodelling of collagen gels and collagenous tissues. *Journal of the Mechanics and Physics of Solids*, 58:918–933, 2010.

[37] A. Krüger-Genge, A. Blocki, R.P. Franke, and F. Jung. Vascular endothelial cell biology: An update. *International Journal of Molecular Sciences*, 20(18):4411, 2019.

[38] D.N. Ku. Blood flow in arteries. *Annu. Rev. Fluid Mech.*, 29:399–434, 1997.

[39] H.P. Langtangen and A. Logg. *Solving PDEs in Python: The FEniCS Tutorial I.* 2016.

[40] P. Libby. The changing landscape of atherosclerosis. *Nature*, 592(7855):524–533, 2021.

[41] P. Libby, P.M. Ridker, and A. Maseri. Inflammation and atherosclerosis. *Circulation*, 105(9):1135–1143, 2002.

[42] S.Q. Liu and Y.C. Fung. Relationship between hypertension, hypertrophy, and opening angle of zero-stress state of arteries following aortic constriction. *Journal of Biomechanical Engineering*, pages 325–335, 1989.

[43] M. Markl, F. Wegent, T. Zech, S. Bauer, C. Strecker, M. Schumacher, C. Weiller, J. Hennig, and A. Harloff. In vivo wall shear stress distribution in the carotid artery. *Circulation: Cardiovascular Imaging*, 3(6):647–655, 2010.

[44] N.M. Mirzaei and P.W. Fok. Simple model of atherosclerosis in cylindrical arteries: impact of anisotropic growth on Glagov remodeling. *Mathematical Medicine and Biology: A Journal of the IMA*, 38:59–82, 2020.

[45] N.M. Mirzaei, W.S. Weintraub, and P.W. Fok. An integrated approach to simulating the vulnerable atherosclerotic plaque. *American Journal of Physiology-Heart and Circulatory Physiology*, 319(4):H835–H846, 2020.

[46] D. Mojsejenko, J.R. McGarvey, S.M. Dorsey, J.H. Gorman III, J.A. Burdick, J.J. Pilla, R.C. Gorman, and J.F. Wenk. Estimating passive mechanical properties in a myocardial infarction using MRI and finite element simulations. *Biomech Model Mechanobiol*, 14:633–647, 2015.

[47] A. Mukherjee and P.W. Fok. A new approach to calculating fiber fields in 2D vessel cross sections using conformal maps. *Mathematical Biosciences and Engineering*, 20:3610–3623, 2023.

[48] Y. Nakashima, Y.X. Chen, N. Kinukawa, and K. Sueishi. Distributions of diffuse intimal thickening in human arteries: preferential expression in atherosclerosis-prone arteries from an early age. *Virchows Arch*, 441:279–288, 2002.

[49] Y. Nakashima, H. Fujii, S. Sumiyoshi, T.N. Wight, and K. Sueishi. Early human atherosclerosis. *Arteriosclerosis, Thrombosis, and Vascular Biology*, 27:1159–1165, 2007.

[50] Y. Nakashima, T.N. Wight, and K. Sueishi. Early atherosclerosis in humans: role of diffuse intimal thickening and extracellular matrix proteoglycans. *Cardiovascular Research*, 79(1):14–23, 2008.

[51] Y. Nakatsukasa, O. Séte, and L.N. Trefethen. The AAA algorithm for rational approximation. *SIAM J. Sci. Comput.*, 40(3):A1494–A1522, 2018.

[52] J.A. Niestrawska, A. Pukaluk, A.R. Babu, and G.A. Holzapfel. Differences in collagen fiber diameter and waviness between healthy and aneurysmal abdominal aortas. *Microscopy and Microanalysis*, pages 1–15, 2022.

[53] S. Numata, K. Itatani, K. Kanda, K. Doi, S. Yamazaki, K. Morimoto, K. Manabe, K. Ikemoto, and H. Yaku. Blood flow analysis of the aortic arch using computational fluid dynamics. *European Journal of Cardio-Thoracic Surgery*, 49(6):1578–1585, 2016.

[54] M.S. Olufsen. Structured tree outflow condition for blood flow in larger systemic arteries. *American Journal of Physiology-Heart and Circulatory Physiology*, 276(1):H257–H268, 1999.

[55] M.S. Olufsen and A. Nadim. - *On deriving lumped models for blood flow and pressure in the systemic arteries.* Elsevier Science Ltd, Oxford, 2003.

[56] M.S. Olufsen, C.S. Peskin, W.Y. Kim, E.M. Pedersen, A. Nadim, and J. Larsen. Numerical simulation and experimental validation of blood flow in arteries with structured-tree outflow conditions. *Annals of Biomedical Engineering*, 28:1281–1299, 2000.

[57] F. Otsuka, M. Joner, F. Prati, R. Virmani, and J. Narula. Clinical classification of plaque morphology in coronary disease. *Nature Reviews Cardiology*, 11(7):379–389, 2014.

[58] T.J. Pence and K. Gou. On compressible versions of the incompressible neo-Hookean material. *Mathematics and Mechanics of Solids*, 20(2):157–182, 2015.

[59] G. Plank, J.D. Bayer, R.C. Blake, and N.A. Trayanova. A novel rule-based algorithm for assigning myocardial fiber orientation to computational heart models. *Annals of Biomedical Engineering*, 40:2243–2254, 2012.

[60] A.R. Pries, T.W. Secomb, and P. Gaehtgens. Biophysical aspects of blood flow in the microvasculature. *Cardiovascular research*, 32(4):654–667, 1996.

[61] A. Procopio, S.D. Rosa, C. Covello, A. Merola, J. Sabatino, A.D. Luca, C. Indolf, F.Amato, and C. Cosentino. Mathematical model of the release of the cTnT and CK-MB cardiac biomarkers in patients with acute myocardial infarction. 18th European Control Conference (ECC), 2019.

[62] A. Quarteroni. What mathematics can do for the simulation of blood circulation. *MOX Report*, 2006.

[63] M.T. Quinn, S. Parthasarathy, and D. Steinberg. Lysophosphatidylcholine: a chemotactic factor for human monocytes and its potential role in atherogenesis. *Proceedings of the National Academy of Sciences*, 85(8):2805–2809, 1988.

[64] M. Rafieian-Kopaei, M. Setorki, M. Doudi, A. Baradaran, and H. Nasri. Atherosclerosis: process, indicators, risk factors and new hopes. *International journal of preventive medicine*, 5(8):927, 2014.

[65] M.A. Reidy, J. Fingerle, and V. Lindner. Factors controlling the development of arterial lesions after injury. *Circulation*, 86(6 Suppl):III43–6, 1992.

[66] R. Ross. Cell biology of atherosclerosis. *Annual review of physiology*, 57(1):791–804, 1995.

[67] K. Sakakura, M. Nakano, F. Otsuka, E. Ladich, F.D. Kolodgie, and R. Virmani. Pathophysiology of atherosclerosis plaque progression. *Heart, Lung and Circulation*, 22:399–411, 2013.

[68] S.G. Sassani, S. Tsangaris, and D.P. Sokolis. Layer- and region-specific material characterization of ascending thoracic aortic aneurysms by microstructure-based models. *Journal of Biomechanics*, 48:3757–3765, 2015.

[69] A.J. Schriefl, A. J. Reinisch, S. Sankaran, D.M. Pierce, and G.A. Holzapfel. Quantitative assessment of collagen fibre orientations from two-dimensional images of soft biological tissues. *J. R. Soc. Interface*, 9:3081–3093, 2012.

[70] S.M. Schwartz, D. deBlois, and E.R.M. O'Brien. The intima: soil for atherosclerosis and restenosis. *Circulation research*, 77(3):445–465, 1995.

[71] R. Shankar, C.A. de la Motte, E.J. Poptic, and P.E. DiCorleto. Thrombin receptor-activating peptides differentially stimulate platelet-derived growth factor production, monocytic cell adhesion, and E-selectin expression in human umbilical vein endothelial cells. *The Journal of Biological Chemistry*, 269(19):13936–13941, 1994.

[72] C. Simonetto, M. Heier, A. Peters, J.A. Kaiser, and S. Rospleszcz. From atherosclerosis to myocardial infarction: A process-oriented model investigating the role of risk factors. *American Journal of Epidemiology*, 00:1–10, 2022.

[73] C. Simonetto, S. Rospleszcz, M. Heier, C. Meisinger, A. Peters, and J. C. Kaiser. Simulating the dynamics of atherosclerosis to the incidence of myocardial infarction, applied to the KORA population. *Statistics in Medicine*, 40:3299–3312, 2021.

[74] P.A. Stonebridge, S.A. Suttie, R. Ross, and J. Dick. Spiral laminar flow: a survey of a three-dimensional arterial flow pattern in a group of volunteers. *European Journal of Vascular and Endovascular Surgery*, 52(5):674–680, 2016.

[75] E.K. Theofilogiannakos, G.K. Theofilogiannakos, A. Anogeianaki, P.G. Danias, H. Zairi, T. Zaraboukas, V. Stergiou-Michailidou, K. Kallaras, and G. Kallaras. A fiber orientation model of the human heart using classical histological methods,

magnetic resonance imaging and interpolation techniques. *Computers in Cardiology*, 35:307–310, 2008.

[76] F.B. Tian, L. Zhu, P.W. Fok, and X.Y. Lu. Simulation of a pulsatile non-Newtonian flow past a stenosed 2D artery with atherosclerosis. *Computers in Biology and Medicine*, 43(9):1098–1113, 2013.

[77] L. N. Trefethen. Numerical conformal mapping with rational functions. *Computational Methods and Function Theory*, 20:369–387, 2020.

[78] O.F. Voropaeva, C.A. Tsgoev, and Y.L. Shokin. Numerical simulation of the inflammatory phase of myocardial infarction. *Journal of Applied Mechanics and Technical Physics*, 62:441–450, 2021.

[79] J. Wong and E. Kuhl. Generating fiber orientation maps in human heart models using poisson interpolation. *Comput Methods Biomech Biomed Engin*, 17:1217–1226, 2014.

[80] C.K. Zarins, M.A. Zatina, D.P. Giddens, D.N. Ku, and S. Glagov. Shear stress regulation of artery lumen diameter in experimental atherogenesis. *Journal of Vascular Surgery*, 5:413–420, 1987.

[81] M. Zaromytidou, G. Siasos, A.U. Coskun, M. Lucier, A.P. Antoniadis, M.I. Papafaklis, K.C. Koskinas, I. Andreou, C.L. Feldman, and P.H. Stone. Intravascular hemodynamics and coronary artery disease: New insights and clinical implications. *Hellenic Journal of Cardiology*, 57(6):389–400, 2016.

Appendix A

PERMISSIONS

Chapter 3 of this thesis is taken from the publication [47] by Avishek Mukherjee and Pak-Wing Fok, with Avishek Mukherjee being the first author. The article is an open access article published by AIMS Press in the journal Mathematical Biosciences and Engineering. The link to rights for the journal is `https://www.aimspress.com/index/news/solo-detail/about` where it is mentioned "All articles published by AIMS Press are Open Access under the Creative Commons Attribution License (`http://creativecommons.org/licenses/by/4.0`). Under this license, authors retain ownership of the copyright for their content, and anyone can copy, distribute, or reuse these articles as long as the author and original source are properly cited".